Electrochemical Energy Reviews (2020) 3:730–765
https://doi.org/10.1007/s41918-020-00078-z

REVIEW ARTICLE

Surface Segregation in Solid Oxide Cell Oxygen Electrodes: Phenomena, Mitigation Strategies and Electrochemical Properties

Kongfa Chen[1] · **San Ping Jiang**[2]

Received: 26 March 2020 / Revised: 21 May 2020 / Accepted: 14 July 2020 / Published online: 10 August 2020
© The Author(s) 2020

Abstract
Solid oxide cells (SOCs) are highly efficient and environmentally benign devices that can be used to store renewable electrical energy in the form of fuels such as hydrogen in the solid oxide electrolysis cell mode and regenerate electrical power using stored fuels in the solid oxide fuel cell mode. Despite this, insufficient long-term durability over 5–10 years in terms of lifespan remains a critical issue in the development of reliable SOC technologies in which the surface segregation of cations, particularly strontium (Sr) on oxygen electrodes, plays a critical role in the surface chemistry of oxygen electrodes and is integral to the overall performance and durability of SOCs. Due to this, this review will provide a critical overview of the surface segregation phenomenon, including influential factors, driving forces, reactivity with volatile impurities such as chromium, boron, sulphur and carbon dioxide, interactions at electrode/electrolyte interfaces and influences on the electrochemical performance and stability of SOCs with an emphasis on Sr segregation in widely investigated (La,Sr)MnO_3 and (La,Sr)(Co,Fe)$O_{3-\delta}$. In addition, this review will present strategies for the mitigation of Sr surface segregation.

Keywords Solid oxide cells · Strontium surface segregation · Driving force · Electrochemical polarization · Oxygen nonstoichiometry modulation · Mitigation

1 Introduction

Solid oxide cells (SOCs) are electrochemical devices capable of both energy storage and regeneration in an intermediate temperature range of 600–800 °C with remarkably high efficiencies and low greenhouse emissions. Of different operating modes of SOCs, solid oxide fuel cells (SOFCs) can directly convert the chemical energy of fuels such as hydrogen, natural gas, ammonia, fossil fuel and biomass fuel into electrical power with high-quality heat being produced as a by-product of the overall power generation process [1–5]. Here, the overall efficiency of SOFCs in terms of combined heat and power (CHP) can reach 65%–85%, which is the highest among the fuel cell family. Alternatively, solid oxide electrolysis cells (SOECs) operate reversibly from SOFCs and are able to store surplus renewable electrical power from solar and wind in the form of useful fuels such as hydrogen, syngas and methane [6–10]. And because the electrical energy demand of electrolysis at high temperatures can partially be compensated by low-cost thermal energy, the electricity to fuel conversion efficiency of SOECs can exceed 100%.

Overall, SOCs consist of a dense electrolyte, a porous hydrogen electrode and a porous oxygen electrode in which the electrolyte is an ionic or protonic conductor that can transport oxygen ions or protons and prevent the intermixing of reactants at both sides of the electrodes. Common electrolyte materials include 8 mol% yttria-stabilized zirconia (YSZ) [11, 12], Gd- or Sm-doped ceria (GDC or SDC) [11, 12], $La_{0.9}Sr_{0.1}Ga_{0.8}Mg_{0.2}O_3$ (LSGM) [13], $BaCe_{0.7}Zr_{0.1}Y_{0.1}Yb_{0.1}O_{3-\delta}$ (BCZYYb) [14, 15], etc. And among these materials, YSZ is a state-of-the-art electrolyte material that can balance the electrical, thermal and mechanical properties of SOCs. As for hydrogen electrodes, these are generally exposed to reducing environments during operation and can provide active sites for the electrochemical oxidation of fuels or the reduction of steam and/or carbon dioxide. Examples of state-of-the-art

✉ San Ping Jiang
S.Jiang@curtin.edu.au

[1] College of Materials Science and Engineering, Fuzhou University, Fuzhou 350108, Fujian, China

[2] WA School of Mines: Minerals, Energy and Chemical Engineering and Fuels and Energy Technology Institute, Curtin University, Perth, WA 6102, Australia

hydrogen electrodes include nickel and ionically conducting YSZ phase-based Ni–YSZ cermet electrodes [16–18]. In addition, oxide materials such as $La_{0.75}Sr_{0.25}Cr_{0.5}Mn_{0.5}O_3$ (LSCrM) [19, 20], Sr_2XMoO_5 (X = Mg, Fe) [21–23], $La_{0.3}Sr_{0.7}TiO_3$ (LST) [24, 25] and $PrBaMn_2O_{5+\delta}$ (PBM) [26] have also been actively explored as potential hydrogen electrode materials. In terms of oxygen electrodes, these operate in air and allow for the electrochemical reduction of gaseous oxygen in the SOFC mode and the oxidation of oxygen ions in the SOEC mode. Currently, a variety of oxygen electrode materials have been investigated, including perovskite oxides such as $La_{1-x}Sr_xMnO_3$ (LSM) [27–31], $La_{0.6}Sr_{0.4}Co_{0.2}Fe_{0.8}O_{3-\delta}$ (LSCF) [32, 33], $La_{0.6}Sr_{0.4}CoO_{3-\delta}$ (LSC) [34], $Ba_{0.5}Sr_{0.5}Co_{0.8}Fe_{0.2}O_{3-\delta}$ (BSCF) [35] and $SrTi_{1-x}Fe_xO_{3-\delta}$ (STF) [36, 37], double-perovskite oxides such as $PrBa_{0.8}Ca_{0.2}Co_2O_{5+\delta}$ (PBCC) [38, 39] and $Ba_{1-x}Gd_{0.8}La_{0.2+x}Co_2O_{6-\delta}$ [40] as well as Ruddlesden–Popper (RP) layered oxides such as $(La,Sr)_2CoO_4$ (LSC214) [41, 42] and $La_2NiO_{4+\delta}$ (LNO) [43, 44]. Figure 1 shows the operational principles of SOCs in both SOFC and SOEC operation modes.

One critical issue in the development of reliable SOC technologies involves poor long-term durability over 5–10 years as required for commercialization. Although SOC performance degradation can be caused by structural, thermal, chemical and mechanical sources from various cell components, one major contributor to performance degradation comes from the oxygen electrode. Here, oxygen electrode degradation can be divided into several categories, including microstructural coarsening, thermal mismatching, cation surface segregation, interfacial reactions as well as deposition and poisoning by volatile impurities such as CrO_3, SO_2, BO_2, CO_2 and H_2O in SOC stacks [45–49]. Among these, surface segregation plays a key role in the chemical instability of oxide surfaces and the performance degradation of SOC electrodes and is a phenomenon generally associated with the redistribution and accumulation of specific cations at oxide surfaces due to a loss of symmetry at the surface relative to the bulk. A typical example involves A-site cation segregation, particularly Sr, which is frequently observed in Sr-containing perovskite-based electrodes such as LSM and LSCF annealed under oxidizing atmospheres and/or at SOC operating conditions and can occupy active surface sites and degrade electrochemical activities for oxygen reactions [33, 50–54]. Surface-segregated SrO is also highly mobile and can migrate across GDC barrier layers to form $SrZrO_3$ insulating layers on YSZ electrolytes [55, 56]. In addition, segregated SrO can interact with volatile impurities to form inert and nonreactive reaction products such as $SrCrO_4$, $SrSO_4$ and $SrCO_3$, causing the drastic poisoning of the electrocatalytic activities of oxygen electrodes [48, 49, 57, 58]. Based on all of this, the fundamental understanding of cation surface segregation is vital in the development of reliable and durable SOC technologies.

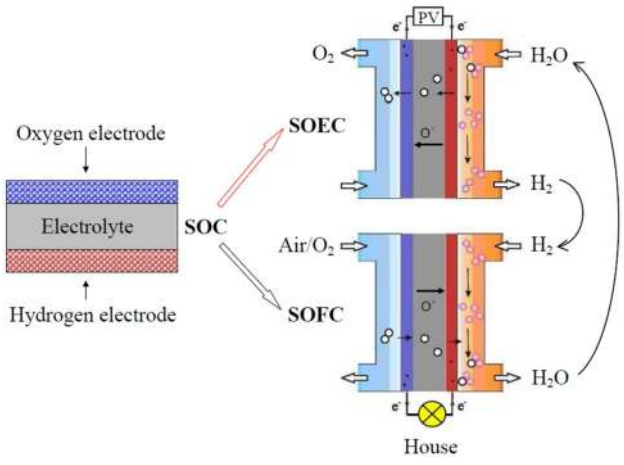

Fig. 1 Operational principles of SOCs in the SOEC mode to store renewable energy in fuels such as H_2 and SOFC mode to generate electricity using stored H_2

Because numerous comprehensive reviews on cation segregation and its origin in perovskite oxide-based electrodes have been published [50–52, 59, 60], this review will focus on the segregation phenomenon, including influential factors, driving forces, reactivity with volatile impurities, mobility and interaction at the electrode/electrolyte interface and the influence of electrochemical polarization on Sr-doped perovskite oxide electrode materials. In particular, the latest developments in the understanding of the intrinsic relationship between surface segregation, interfaces and the activity of common and widely investigated electronic conducting LSM and mixed ionic and electronic conducting (MIEC) LSCF electrodes will be reviewed in detail. The latest developments in the mitigation of SrO surface segregation will also be discussed.

2 Phenomenon of Surface Segregation

2.1 Lanthanum Strontium Manganite (LSM)

SrO surface segregation has been extensively reported on LSM-based electrodes [53, 61–65]. For example, Dulli et al. [61] annealed $La_{0.65}Sr_{0.35}MnO_3$ film at 900 °C in oxygen for 10 h and probed appreciable SrO segregation on the film surface using surface sensitive angle resolved X-ray photoelectron spectroscopy (XPS). In another study, de Jong et al. [62] deposited an LSM film at 750–800 °C in low vacuum followed by annealing at 450 °C in high vacuum and used XPS and ultraviolet photoelectron spectroscopy (UPS) analyses to reveal the presence of SrO and $SrCO_3$ a few angstroms in thickness on the film surface. Jiang et al. [53] used inductive coupled plasma optical

emission spectroscopy (ICP-OES) analysis to show that the concentrations of Sr and Mn in the solution collected after the acid treatment of freshly prepared LSM electrodes after annealing at 1150 °C in air were one order of magnitude higher than that of La. Furthermore, Huber et al. [66] reported that a high Sr content was an indication of Sr enrichment or segregation on LSM surfaces based on observations of Sr segregation on LSM thin-film electrodes using in situ XPS and quasi-static secondary ion mass spectroscopy (ToF-SIMS).

In addition to Sr segregation, the surface segregation of B-site Mn cations in LSM and subsequent migration to YSZ electrolyte surfaces have also been observed under low oxygen partial pressures and cathodic polarization conditions [67–71]. For example, de Jong et al. [71] annealed an LSM film in varied oxygen partial pressures and reported based on X-ray adsorption spectroscopy (XAS) that annealing in ultra-high vacuum conditions can result in strong increases in the peak assigned to Mn^{2+} and that this peak intensity decreased in oxygen-rich environments due to the increased valence state of Mn cations. Davis et al. [72] deposited an LSM film onto lattice matched $LaAlO_3$ and $NdGaO_3$ substrates and reported that total reflection X-ray fluorescence (TXRF) measurements showed the surface segregation of Mn cations during annealing at 800 °C in air accompanied by the increase in the Mn valence state to +4 at the surface as revealed using X-ray absorption near edge spectroscopy (XANES). In further examples, Backhaus-Ricoult et al. [67] observed the rapid migration of Mn^{2+} from an LSM film to a YSZ electrolyte surface using in situ photoelectron microscopy under polarization conditions and Jiang et al. [49] confirmed the segregation and subsequent diffusion of Mn cations at LSM surfaces through the systematic study of Cr deposition on LSM electrode systems (this will be discussed in following sections).

2.2 Lanthanum Strontium Cobalt (LSC)-Based Electrodes

Sr segregation is also well known in LSC-based electrodes [33, 73–76]. For example, Niania et al. [76] in situ investigated the microstructural and elemental evolution of LSCF pellets using high-temperature environmental scanning electron microscopy (HT-ESEM) and reported that the extent of SrO surface segregation increased with increasing annealing temperatures in the range of 750–1000 °C (Fig. 2). Here, the evolution of surface-segregated SrO can be divided into three distinct stages: (1) the rapid growth of segregated particles on grain boundaries, defect points and at the centre of grains; (2) the agglomeration of segregated particles; and (3) the continuous coarsening of segregated particles during annealing.

Detailed elemental information concerning LSC-based electrode surfaces can further be obtained using high surface sensitive techniques such as low-energy ion scattering (LEIS). For example, Druce et al. [77, 78] used LEIS to probe the surface chemistry of LSCF pellets after annealing at 400, 600 and 800 °C in air for 8 h as well as at 1000 °C in oxygen for 12 h and found that the onset temperature of SrO surface segregation occurred at as low as 400 °C and that the extent of segregation increased with increasing temperatures (Fig. 3a). Alternatively, these researchers also found that transition metals in B-sites disappeared on the surface at

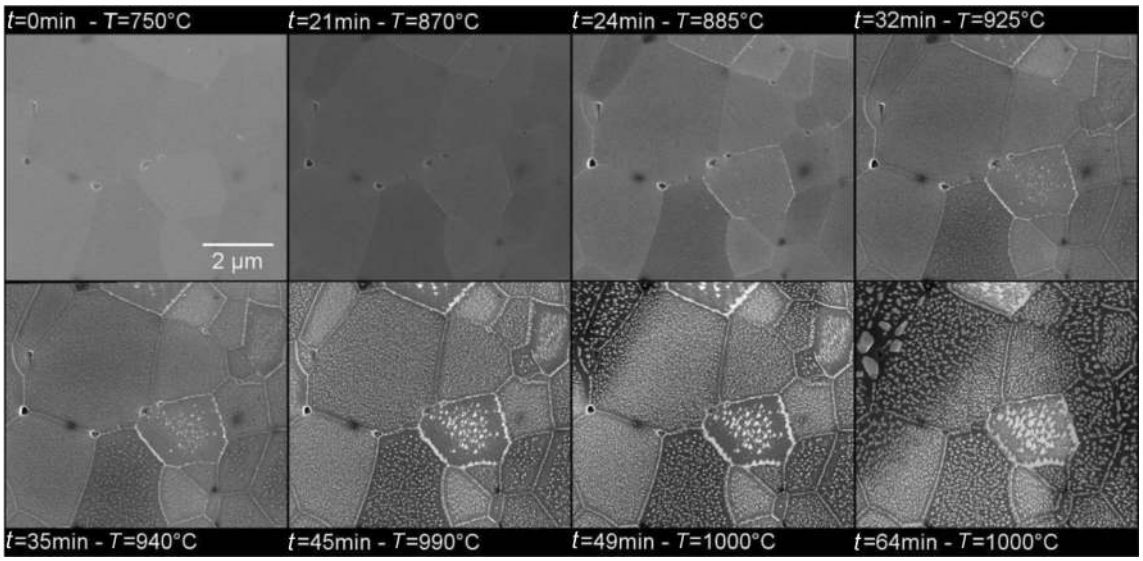

Fig. 2 HT-ESEM micrographs of SrO segregation on a polished LSCF surface in situ observed at high temperatures under 300 Pa of water vapour. Reproduced with permission from Ref. [76]. Copyright 2016, WILEY-VCH Verlag GmbH & Co. KGaA, Weinheim

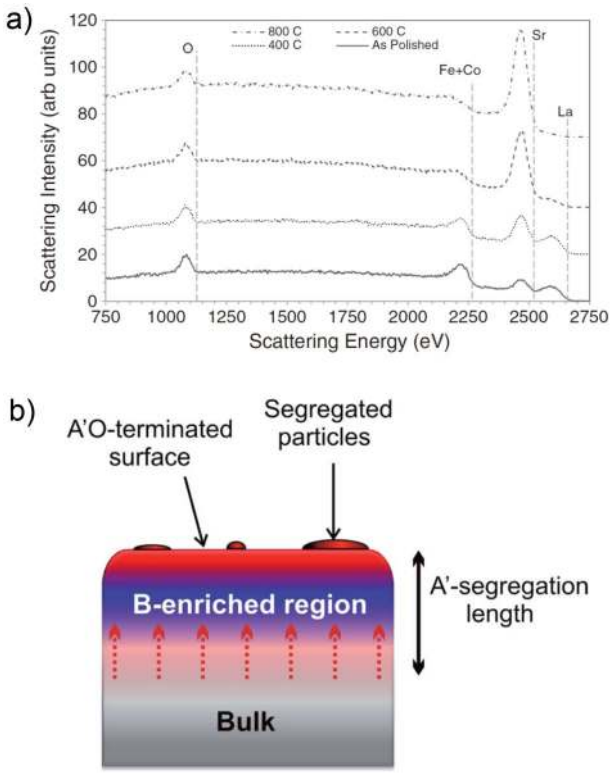

Fig. 3 **a** LEIS spectra of LSCF pellets annealed at various temperatures, **b** schematic of the compositional variations in the near-surface region of LSCF after annealing at 1000 °C. Reproduced with permission from Ref. [77, 78]. Copyright 2014, Elsevier; Copyright 2014, Royal Society of Chemistry

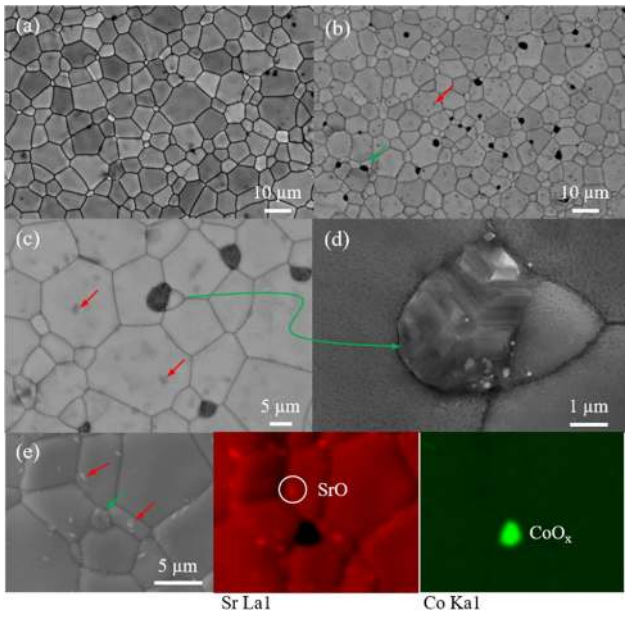

Fig. 4 SEM micrographs of **a** freshly prepared LSCF and **b** LSCF after heat treatment at 800 °C in air for 96 h; **c**, **d** enlarged images of the segregated micron-sized particles and **e** EDS element mapping of Sr and Co. Arrows indicate segregated and isolated submicron-sized particles and large particles, modified based on Ref. [86]. Reproduced with permission from Ref. [86]. Copyright 2014, Royal Society of Chemistry

temperatures above 600 °C (Fig. 3b). Similar to segregated Sr species on LSM surfaces [53], segregated SrO can also be removed from LSC and LSCF electrode surfaces and films using acid etching [79–82]. For example, Kubicek et al. [79] etched the LSC film in 0.12 mol L^{-1} HCl solution for 5 s and reported a significantly reduced Sr surface content. Despite this, Sr tends to re-segregate on etched surfaces quickly at elevated temperatures [81, 82].

SrO surface segregation can occur on porous LSCF electrodes after long-term operation. For example, Simner et al. [55] observed the significant performance degradation of an anode-supported YSZ film|GDC barrier layer LSCF cell after operation at 750 °C for 500 h and XPS analysis revealed that Sr segregated on both the outer and inner surfaces of the LSCF electrode and that the thickness of the Sr-segregated layer was 35–75 nm. In addition, these researchers reported the formation of a $SrZrO_3$ reaction layer at the YSZ/GDC interface. In the case of the annealing of LSCF electrodes in the GDC electrolyte at 800 °C in air for 800 h, Wang et al. [83] found evidence of SrO surface segregation by detecting Sr species in the etched LSCF.

SrO surface segregation is usually accompanied by variations in electrode lattice parameters. For example, Hardy et al. [84] measured the X-ray diffraction (XRD) patterns of a cell with an anode-supported YSZ film|GDC barrier layer|LSCF electrode operating under constant current conditions at 750 °C and found that the diffraction patterns of LSCF continually changed during operation under load for more than 60 h in air in which the cubic lattice parameter of their LSCF was 3.92502 Å in the initial stage of operation and increased to 3.92650 Å after 60 h. This lattice expansion was also observed by Chang et al. [85] on an LSCF thin-film electrode under cathodic polarization using synchrotron X-ray techniques.

B-site Co cation surface segregation can also occur on LSC and LSCF electrodes. For example, Zhao et al. [86, 87] annealed LSCF pellets at 800 °C in air for 96 h and observed the segregation of both Sr and Co on the LSCF surface to form separated SrO and CoO_x oxide particles (Fig. 4). As shown in Fig. 4, the surface of the freshly prepared LSCF sample before testing was dense, smooth and clean without pinholes, whereas the surface morphology of the LSCF sample after annealing changed significantly. Here, the formation of submicron-sized particles (less than 1 μm) and dark coloured particles (as large as ~ 5 μm) on the surface of the LSCF sample was detected and EDS element mapping identified the fine particles as SrO and the large particles as CoO_x. In addition, Ni et al. [75] observed the generation of a $CoFeO_{3.5}$ phase after annealing an LSCF electrode at

900 °C in air for 5 h. Co segregation has also been observed on LSC and LSCF electrodes after electrochemical polarization. As examples, Mutoro et al. [88] observed the segregation of Co on the LSC film after anodic polarization and Chang et al. [89] reported that Co segregated uniformly on LSCF film surfaces based on in situ synchrotron-based TXRF analysis and that this segregation responded sensitively and reversibly to electrochemical polarization. Baumann et al. [90] further observed the surface segregation of both Sr and Co on LSCF films as induced by cathodic polarization. And in the case of the reversible operation of a $La_{0.57}Sr_{0.38}Co_{0.18}Fe_{0.72}Nb_{0.1}O_{3-\delta}$ (LSCFN) electrode directly assembled on the YSZ electrolyte, He et al. [91] found that Co-rich particles were generated in the vicinity of the LSCFN/YSZ interface at 750 °C under 0.5 A cm^{-2} for 240 h and that the number of particles increased in proportion to the degree of Sr accumulation at the interface, indicating the close correlation between Sr and Co segregation.

2.3 Other oxygen Electrode Materials

In addition to LSM and LSC-based electrodes, cation surface segregation also occurs on various perovskite oxides, layered perovskite oxides and RP oxides. For example, Norman and Leach [92] carried out the in situ and quasi in situ high-temperature XPS analysis of BSCF pellets in vacuum and found that although Co (and Fe) ions were predominant on the surface at intermediate temperatures (300 and 500 °C), Ba and Sr segregated to the surface at a higher temperature of 800 °C. Jung and Tuller [36] also detected an appreciable degree of Sr-excess at the surface of as-deposited STF films using XPS. In addition, Chen et al. [41] analysed the surface chemistry of (001) and (100) faceted RP oxide $(La_{1-x}Sr_x)_2CoO_4$(LSC214, $x = 0.25$ and 0.50) films using LEIS and XPS and reported that in the as-prepared films, the top surface was Sr-rich, whereas the subsurface was Co-rich. These researchers also reported that after annealing at elevated temperatures, the extent of SrO segregation increased and that the segregated SrO clustered into Sr-rich secondary phase particles. Burriel et al. [93] also characterized the surface of a $La_{1.67}Sr_{0.33}NiO_{4+\delta}$ (LSN) film using surface sensitive techniques including the crystal truncation rod, LEIS and angle-resolved XPS (ARXPS) and reported that both La and Sr can segregate onto the outer surface of LSN, whereas Ni was located in the subsurface region. Furthermore, researchers reported dominant La surface segregation in Sr-free LNO [78] and $LaCoO_{3-\delta}$ [94]. Moreover, Kilner's group [78, 95, 96] investigated the surface chemistry of double-perovskite $GdBaCo_2O_{5+\delta}$ (GBC) and $PrBaCo_2O_{5+\delta}$ (PBC) pellets annealed at 400–800 °C using LEIS and reported that Ba cations can rapidly segregate to the surface and that segregation started from 400 °C. Wei et al. [97] also observed that the extent of Ba surface segregation on PBC was affected by electrochemical polarization in which the level of Ba segregation increased through anodic polarization and decreased through cathodic polarization.

3 Influential Factors of Cation Surface Segregation

The extent of cation surface segregation, particularly Sr, is affected by various factors, including stoichiometric composition, strain, temperature, oxygen partial pressure, the nature of oxide samples, the type of cations in B-sites and electrochemical polarization condition.

3.1 Stoichiometric Composition

Sr surface segregation greatly depends on stoichiometric composition, in particular the amount of Sr dopant [41, 98, 99]. For example, Decorse et al. [98] prepared $La_{1-x}Sr_xMnO_3$ pellets with various Sr dopant concentrations ($x = 0$, 0.2, 0.5 and 1) and reported that the level of SrO surface segregation at high temperatures depended on Sr concentration. Chen et al. [41] prepared LSC214 RP oxide films with Sr dopants of 25% and 50% and reported that the as-deposited film with a higher Sr dopant level led to a higher coverage of Sr on the surface and a thicker Co-rich layer in the subsurface. In addition, Yu et al. [99] deposited LSCF films onto a $NdGaO_3$ (NGO) substrate with a varying Sr content ($x = 0.2$, 0.3 and 0.4) and found that the lowering of the Sr content from 40% to 30% decreased SrO surface segregation, but that further lowering of the Sr content to 20% increased SrO segregation. Here, these researchers attributed the increase in surface segregation at 20% Sr to the high tensile strain among the samples in which a model correlating SrO segregation with strain showed that at a fixed strain, SrO surface segregation increased linearly with an increased Sr content. Furthermore, Wang et al. [100] deposited LSCF electrodes with 40% and 20% Sr on dense GDC barrier layer/YSZ pellets and sintered the samples at 1100 °C and 1200 °C for 168 h. Here, these researchers observed the formation of $SrZrO_3$ at the GDC/YSZ and LSCF/GDC interfaces and reported that the amount of $SrZrO_3$ increased with increasing Sr concentration in the LSCF.

The extent of SrO surface segregation also depends on the type of B-site cations in which thermodynamic calculations indicate that SrO activity in $(La,Sr)MO_3$ (M = Fe, Co, Mn) is in the order of Co > Fe > Mn [101]. In STF films, Chen et al. [102] reported that SrO segregation increased with increasing the Fe content and first principle calculations conducted by Ding et al. [103] suggested that the substitution of Fe with Co in LSCF can increase SrO segregation. Kwon et al. [104] also compared the effects of B-site cations on SrO surface segregation in Sr-doped $LaBO_3$ (001) ($B = Cr_{0.50}Mn_{0.50}$,

Mn, Fe, $Co_{0.25}Fe_{0.75}$, Co and Ni) using DFT calculations and suggested that the minimization of elastic energy was the main driving force of SrO segregation in which these researchers predicted that larger B-site cations can lead to greater compressive strain on dopant cations and thereby increased SrO surface segregation.

3.2 Strain

In terms of the effects of strain on Sr surface segregation, Lussier et al. [105] deposited a $La_{1/2}Sr_{1/2}MnO_3$ film with a lattice constant of 0.3866 nm and a $La_{2/3}Ca_{1/3}MnO_3$(LCM) film with a lattice constant of 0.3867 nm onto (100) faceted $SrRuO_3$ (SRO), $SrTiO_3$ (STO), $NdGaO_3$ (NGO) and $LaAlO_3$ (LAO) substrates with lattice constants of 0.3940 nm, 0.3905 nm, 0.3864 nm and 0.3793 nm, respectively, in which these substrates can provide a broad range of in-plane biaxial stress ranging from tensile (+ 1.91% for SRO and + 1.01% for STO) to relaxed (for NGO) and to compressive stress (− 1.89% for LAO). The results showed that compressive or tensile interfacial strain can modify the relative concentrations of La and Sr in the interfacial region to achieve better lattice matching. Estrade et al. [106, 107] also deposited a 20-nm-thick LCM film onto STO (001) and (110) substrates to generate relaxed and tensile strained surfaces, respectively, and their electron energy loss spectroscopy (EELS) results showed that tensile strain can lead to La depletion at the free film surface and La enrichment at the LCM/STO interface, whereas relaxed films were chemically homogeneous. In addition, Jalili et al. [108] grew a 10-nm-thick LSM film onto (001) STO and (001) LAO substrates using PLD to generate in-plane tensile strain and in-plane compression strain, respectively, and observed a higher tendency for SrO segregation and higher concentrations of surface oxygen vacancies on the tensile strained LSM surface due to the larger spacing available for Sr cation accommodation and the reduced elastic energy on the surface as compared with the bulk. This positive effect of tensile strain on increasing oxygen diffusivity has also been reported on Au dispersed $Pr_{1.9}Ni_{0.71}Cu_{0.41}Ga_{0.05}O_{4+\delta}$ [109] and $La_{0.8}Ce_{0.1}Ni_{0.4}Ti_{0.6}O_3$ with embedded metal nanoparticles [110], demonstrating that high concentrations of surface oxygen vacancies can play a key role in accelerating SrO segregation.

The accelerating effects of tensile strain on SrO surface segregation have also been observed on LSC and LSCF samples. For example, Cai et al. [111] deposited an LSC film onto STO and LAO substrates to generate tensile and compressive strain and found that although both tensile and compressive strain can induce Sr-rich surfaces, SrO segregation was slightly more pronounced in the case of tensile strain. In the case of LSCF films, Yu et al. [99] deposited LSCF films onto NGO, STO and $GdScO_3$ (GSO) substrates and found that SrO surface segregation increased with tensile strain and decreased with compressive strain. To gain a better understanding of the effects of strain on surface segregation, Liu et al. [112] further conducted experimental and DFT studies and found that tensile strain tended to create greater oxygen deficiencies on LSC surfaces than compressive strain due to the smaller oxygen vacancy formation energy associated with tensile strain.

3.3 Temperature

Sr surface segregation is also sensitive to temperature [113–115]. For example, Katsiev et al. [114] in situ probed the surface chemistry of polycrystalline LSM films as a function of temperature using Auger electron spectroscopy (AES) and observed Sr segregation on LSM surfaces at temperatures above of 400 °C and that the extent of segregation increased with increasing temperature. The onset temperature of surface segregation is further dependent on the dopant type. For example, Lee et al. [116] annealed 20 mol% Ba-, Sr- and Ca-doped $LaMnO_3$ films and probed the corresponding surfaces using atomic force microscopy (AFM) and ARXPS. Here, these researchers reported that surface-segregated Ba and Sr dopant particles appeared at 430 and 630 °C, respectively, and grew larger upon annealing at higher temperatures but that no structural changes were found on the film surfaces with Ca dopant up to 830 °C (Fig. 5).

In another study, Oh et al. [113] annealed LSCF pellets in temperatures ranging from 600 to 900 °C in air for 50–100 h and found that the amount of surface-segregated SrO increased with increasing temperature. Mutoro et al. [88] in situ investigated the surface composition of LSC films at varying temperatures of 25–650 °C at a low oxygen partial pressure of 1×10^{-6} mbar and observed that Sr-containing secondary components on film surfaces increased with increasing temperature. Chen et al. [41] further reported that the surface roughness of an LSC214 film and its coverage by SrO particles increased with increasing annealing temperature at 400 and 500 °C.

The stability of segregated SrO appears to be also related to treatment temperature. For example, Caillol et al. [65] reported that an as-prepared LSM electrode sintered at 1200 °C was characterized by a SrO-segregated surface but that the SrO segregation disappeared after annealing at 800 °C for 1 week with no microstructural change. Chang et al. [117] also showed that Sr-rich nanoparticles can slowly be reincorporated into LSM films if annealed at 700 °C.

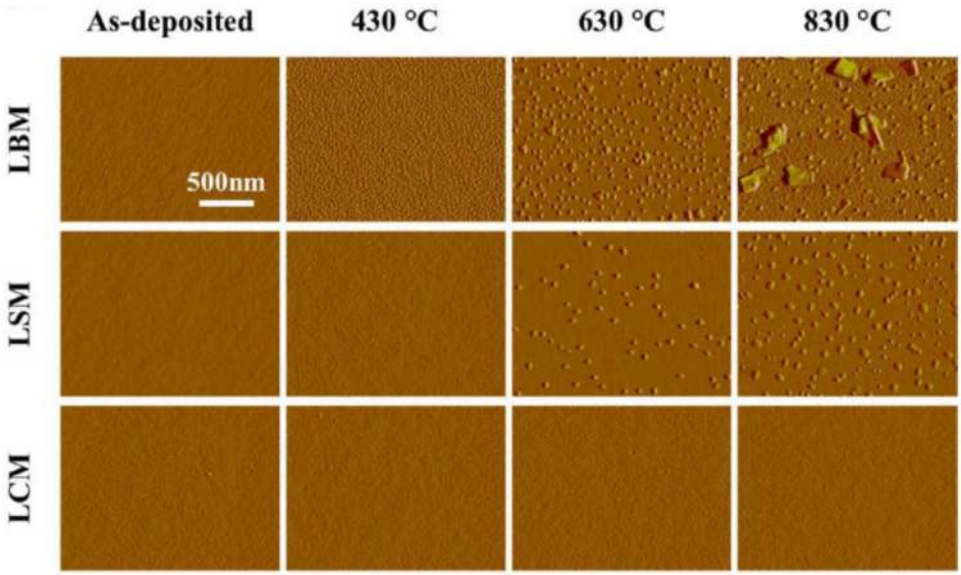

Fig. 5 AFM amplitude images of Ba-, Sr- and Ca-doped $LaMnO_3$ film surfaces as a function of annealing temperature. Reproduced with permission from Ref. [116]. Copyright 2013, American Chemical Society

3.4 Oxygen Partial Pressure

The amount of SrO surface segregation on LSM is further dependent on oxygen partial pressure (P_{O_2}). For example, Fister et al. [118] probed the surface composition of LSM films using in situ synchrotron-based TXRF and observed that the concentration of surface Sr decreased with increasing P_{O_2}. Caillol et al. [65] observed a similar trend by exposing LSM powder to different P_{O_2} at 900 °C in which the Sr/La ratio on the LSM surface probed by XPS was 0.38 in 1% O_2 and decreased to 0.24 in 20% O_2. Alternatively, Rohnke et al. [119] reported that the annealing of LSCrM in a P_{O_2} of 10^{-9} mbar at 550 °C led to the gradual deletion of surface Sr and that as P_{O_2} increased to 10^{-6} mbar, more Sr diffused from the LSCrM film to the YSZ surface. Lee et al. [116] also observed increased Sr segregation on LSM films at higher oxygen partial pressures. Similar increases in Sr segregation in O_2 rich atmospheres were reported by Oh et al. [113] on LSCF pellets annealed in pure N_2, 0.1% O_2 and 21% O_2 at 800 and 890 °C for 50 h.

3.5 Microstructure or Morphology of Perovskite Oxides

The microstructure or morphology of perovskite oxides such as single-crystal films, polycrystalline pellets, powders and porous electrodes plays a vital role in determining SrO surface segregation [17, 74, 115]. For example, Plonczak et al. [120]. reported that the columnar grain boundaries of LSCF can increase surface areas by approximately 25 times as compared with dense flat films. Alternatively, la O' et al. [121] reported that LSC films can exhibit enhanced surface oxygen exchange kinetics and O_2 reduction reaction (ORR) activities as compared with bulk samples. Decorse et al. [98] further compared the surface composition of fine LSM powders and pellets and concluded that grain boundaries had a vital effect on surface composition.

As-deposited LSC and LSCF thin films that are epitaxially grown using pulsed laser deposition (PLD) initially show Sr-rich and Co-poor termination surface layers [41, 80, 81, 122, 123] in which the extent of surface segregation on these films is dependent on deposition temperature. For example, Cai et al. [80] used PLD to grow 200-nm-thick LSC films on YSZ (100) electrolytes at 450 and 650 °C and created poor and well crystalline films. The LSC film grown at 650 °C underwent surface structural change from a Sr-rich state to a $SrO/Sr(OH)_2$-rich phase-separated state, whereas the LSC film grown at 450 °C showed no surface segregation or phase separation. A recent study on LSCF thin-film electrodes prepared using PLD on GDC-buffered YSZ single-crystal substrates indicated significant differences between as-grown LSCF thin films in terms of the apparent surface exchange coefficient and surface segregation, indicating the dependence of oxygen exchange properties and surface segregation on the surface chemistry and nanostructure of film electrodes [124].

Crumlin et al. [125] also compared the temperature-dependent surface chemistry and behaviour of LSC pellets and LSC (001) films and reported that during annealing at elevated temperatures, the coverage of surface secondary phases on LSC films became smaller and Sr surface segregation increased with increasing temperature, whereas LSC pellets underwent no detectable change, suggesting that careful consideration is required in the comparison of findings published by different groups.

3.6 Electrochemical Polarization

3.6.1 LSM

Early studies on LSM electrodes show that the electrocatalytic performance of LSM for ORR is highly sensitive to electrochemical polarization in which the electrocatalytic performance of freshly prepared LSM electrodes can be significantly enhanced by cathodic polarization but reduced by anodic polarization [53, 126–128]. Here, oxygen vacancies are generated at the LSM electrode/YSZ electrolyte interface under cathodic polarization and the subsequent positive charge of the oxygen vacancies can be compensated by the reduction of B-site Mn ions. This can be represented as follows in Kröger–Vink notation [129, 130]:

$$O^{x}_{O,LSM} + 2Mn^{x}_{Mn} + V^{\cdot\cdot}_{O,YSZ} + 2e \rightarrow V^{\cdot\cdot}_{O,LSM} + 2Mn'_{Mn} + O^{x}_{O,YSZ} \quad (1)$$

$$O^{x}_{O,LSM} + 2Mn^{\cdot}_{Mn} + V^{\cdot\cdot}_{O,YSZ} + 2e \rightarrow V^{\cdot\cdot}_{O,LSM} + 2Mn^{x}_{Mn} + O^{x}_{O,YSZ} \quad (2)$$

in which $V^{\cdot\cdot}_{O,LSM}$ and $V^{\cdot\cdot}_{O,YSZ}$ are oxygen vacancies at LSM and YSZ and $Mn^{\cdot}_{Mn}$, Mn^{x}_{Mn} and Mn'_{Mn} are Mn^{4+}, Mn^{3+} and Mn^{2+} ions, respectively. The effective ionic radii for Mn ions in octahedral coordination (CN = 6) are: $Mn^{2+} = 0.67$ (LS) and 0.83 (HS); $Mn^{3+} = 0.58$ (LS) and 0.645 (HS); $Mn^{4+} = 0.53$ Å (LS) in which LS and HS refer to low and high spin [131]. Thus, the charge compensation through the reduction of B-site cations (and/or) will cause the increase in average cation size, e.g. the increase is 15.5% and 28.7% for Mn^{3+} to Mn^{2+} in LS and HS, respectively, and 9.4% for Mn^{4+} to Mn^{3+} in LS. Cation size increase leads to lattice expansion and would in turn increase the internal stress, which would drive the substituted Sr cations and/or B-site Mn cations to the surface, similar to the elastic interaction due to the size mismatch between the Sr dopant and the La host. Experimentally, B-site Mn cation segregation to the LSM surface under cathodic polarization has been observed by Backhaus-Ricoult et al. [67] using photoelectron microscopy techniques. The segregation and subsequent migration of Mn species to the TPB region of the LSM/YSZ interface have been well documented by deposition and poisoning of Cr studies and formation of $(Cr,Mn)_3O_4$ spinels [49, 132, 133]. On the other hand, A-site Sr segregation to the LSM surface under cathodic polarization is inconsistent with the significant reduction of segregated SrO on LSM surface as shown by in situ studies on the surface chemistry of LSM using XPS and time-of-flight secondary ion mass spectrometry (ToF-SIMS) [66] and with significant enhancement of the electrochemical activity of LSM under cathodic polarization [53, 126–128]. This indicates that the charge compensation mechanism for the oxygen vacancy formation under cathodic polarization conditions through valence change of B-site Mn ions cannot explain the removal and disappearance of segregated Sr under cathodic polarization conditions.

Another viable charge compensation mechanism is through incorporating SrO into La lattice sites, forming negatively charged defect, Sr'_{La}. This is possible as the positively charged oxygen vacancies induced by cathodic polarization are essentially on the surface of LSM in the TPB regions. In this case, the incorporation of segregated SrO is driven by the electrostatic interaction and we will discuss this in more details later. Under anodic polarization, LSM experiences oxidation conditions with oxygen excess nonstoichiometry, similar to that at high oxygen partial pressure [134]. The negatively charged oxygen excess could push the already exited negatively charged defect, Sr'_{La}, to the surface through the electrostatic repulsive force. The segregated SrO species occupy the active sites and deteriorate the electrochemical activity of LSM for ORR, consistent with the deactivation effect of LSM under anodic polarization conditions [128].

The phenomena of Sr incorporation and segregation in LSM under cathodic and anodic polarization have been validated by numerous in situ characterization techniques. For example, Chang et al. [117] used grazing incidence XRD (GIXRD) to in situ probe the cation concentration of LSM films during annealing and under applied cathodic potential at 800 °C and observed that after annealing, SrO segregation was found to occur uniformly over the LSM surface, whereas after applying a cathodic potential, Sr amounts were reduced on ~ 70% of the LSM surface. Huber et al. [66, 135] also in situ studied the surface chemistry of LSM and LSCrM films under polarization using XPS and ToF-SIMS and observed that cathodic polarization led to the depletion (or incorporation) of Sr on surfaces, whereas anodic polarization led to Sr surface segregation (Fig. 6). The Sr incorporation on the LSCrM is relatively a faster process under cathodic polarization as compared to the Sr segregation under anodic polarization conditions. A similar phenomenon was also reported on LSCrM films by Rohnke et al. [119]. Sr surface segregation driven by anodic polarization under SOEC mode was also confirmed through observations of $SrCrO_4$ formation under Cr poisoning conditions [136] in contrast to the formation of a $(Cr,Mn)_3O_4$ spinel phase by cathodic polarization under the SOFC mode on LSM electrodes [132]. The effects of polarization current on the performance and surface chemistry of LSM electrodes reported in the literature are listed in Table 1.

3.6.2 LSC-Based Electrodes

Electrochemical polarization also has a remarkable impact on cation segregation on the surface of LSC-based electrodes. Different from that observed on LSM electrodes, however, cathodic polarization generally increases cations,

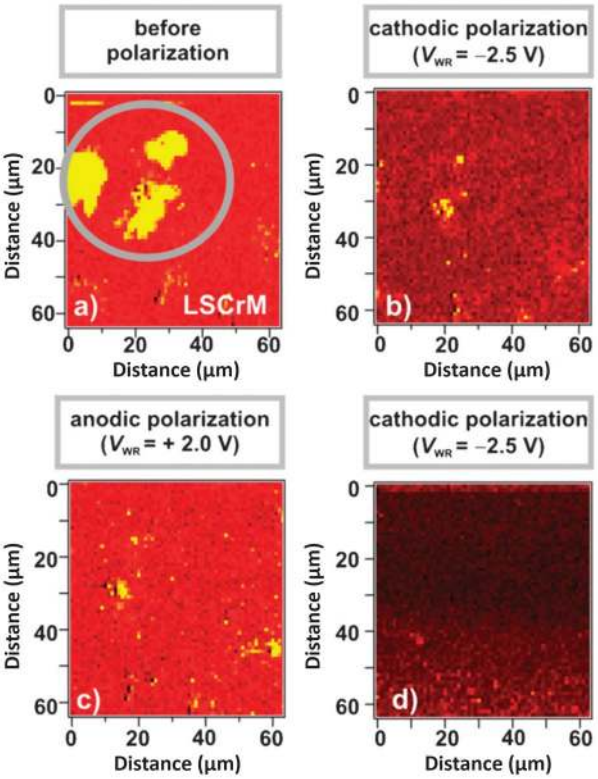

Fig. 6 Scanning X-ray photoelectron microscopy (SPEM) images of the Sr 3d component monitored on LSCrM surfaces at different applied voltages. Bright colours denote high Sr concentration, and dark colours denote low Sr concentration. Reproduced with permission from Ref. [135]. Copyright 2012, Royal Society of Chemistry

particularly Sr segregation. For example, Vovk et al. [137] studied the surface chemistry of LSC film surfaces under polarization using in situ XPS and found that under cathodic polarization, the Sr/(La + Co) ratio at the LSC surface increased irreversibly by 5%, whereas the La/Co ratio remained constant. Baumann et al. [90] also observed that cathodic polarization led to increases in surface Sr and Co on LSCF films but that surface compositions remained unchanged by anodic polarization. Mutoro et al. [88] further probed the surface composition of LSC films using synchrotron XPS and observed SrO surface segregation by applying cathodic polarization as well as Sr incorporation and Co segregation by applying anodic polarization. A similar reversible change in surface Sr content was reported on LSC/LSC214 bi-layer films as well [88]. Alternatively, Choi et al. [138] tested LSCF films on GDC at 600 °C for 540 h and observed decreased R_P after cathodic polarization and increased R_P after anodic polarization.

The redistribution of cations induced by polarization may have a correlation with the change in cell volume or surface oxygen vacancy concentration. For example, Kivi et al. [139] in situ investigated the lattice parameters of porous LSC and LSCF electrodes under different atmospheres and polarization conditions using high-temperature XRD and reported that under open-circuit conditions, cell volumes increased slightly with decreasing oxygen partial pressures, but that the effects of oxygen partial pressure on cell volume became more significant if a cathodic potential was applied, in which cell volumes increased with increasing cathodic potential and the degree of volume expansion was more significant at lower oxygen partial pressures. These researchers also

Table 1 Effects of polarization current on the performance and surface chemistry of LSM and LSCrM electrodes

Cathode materials	Operating conditions	Performance variation	Extent of Sr surface segregation	Probing method	Reference
LSM film	T: 800 °C; t: 72 h; E: −280 mV	–	Decreased by cathodic	GIXRD	[117]
LSM film	PO_2: 10^{-6} mbar; T: 500 and 600 °C; E: −2.5 to 2 V	Activation by cathodic; deactivation by anodic	Cathodic < anodic	In situ XPS/SPEM and ToF-SIMS	[66]
LSCrM film	PO_2: 10^{-6} mbar; T: 500 and 600 °C; E: −2.5 to 2 V	Activation by cathodic	Cathodic < anodic	In situ XPS/SPEM; quasi in situ ToF-SIMS	[135]
LSCrM film	PO_2: 1×10^{-9} and 1×10^{-6} mbar; T: 550 °C; E: −3.5 to 2.8 V	–	Either cathodic or anodic potential, enrichment or depletion of different cations	Quasi in situ ToF-SIMS	[119]
LSM film	–	Activation by cathodic	–	–	[127]
LSM film (a quenched LSM surface enriched with La)	–	–	La segregation: cathodic < anodic	Quasi in situ AES and XPS	[174]
LSM electrode	PO_2: in air; T: 800 °C; In CrO_3	Accelerated degradation by anodic	Increased by anodic	Ex situ SEM-EDS	[136]

showed that the effects of cathodic potential on the change in lattice parameters were reversible by switching the potential between 0 and −0.9 V [140]. Here, the increase in cell volume by applying a cathodic potential is possibly due to the increase in oxygen vacancies or the decrease in the effective oxidation state of Co ions.

Table 2 lists the effects of polarization current on the performance and surface chemistry of selected LSC and LSCF electrodes reported in the literature.

3.6.3 Reversible Polarization

Surface segregation, particularly Sr species in YSZ electrolyte-based SOCs, is a complex issue due to the high activity of segregated Sr species with YSZ electrolyte and its significant dependence on the direction of polarization current. In the case of LSCF electrodes, although a GDC barrier layer is generally applied on YSZ electrolytes to function as a barrier layer, segregated Sr cations can readily diffuse through the pores or grain boundaries of the GDC layer to form a resistive $SrZrO_3$ phase at the GDC/YSZ interface region, in which the amount of formed $SrZrO_3$ is a good indication of the extent of Sr surface segregation. For example, Matsui et al. [141] reported that after an LSCF electrode was polarized in the cathodic mode at 0.3 A cm^{-2} and 1000 °C for 400 h, the volume of $SrZrO_3$ at the YSZ/GDC interface increased by 6 times as compared with that before polarization. Khan et al. [142] also prepared half cells with LSCF–GDC electrodes sintered on $(Sc_2O_3)_{0.10}(CeO_2)_{0.01}(ZrO_2)_{0.89}$ (ScCeSZ) electrolytes at 1150 °C without a GDC barrier layer and reported that electrode activities decreased as polarization current densities increased in the range of 0–1.5 A cm^{-2} at 900 °C for 1000 h and that the Sr content at the LSCF–GDC /ScCeSZ interface increased with increasing current density. In the case of flat tubular single cells with co-sintered YSZ film/GDC barrier layers, Khan et al. [143] reported that performance degradation greatly increased with increasing current densities at 800 °C for 1000 h.

Recently developed direct assembly techniques provide an effective approach to study the intrinsic relationship between Sr segregation, interfacial formation and reaction of LSC-based electrodes on YSZ electrolytes [144, 145]. With the directly assembled electrodes, it has been found that cathodic polarization can not only in situ induce the

Table 2 Effects of polarization current on the performance and surface chemistry of LSC and LSCF electrodes

Cathode materials	Operating conditions	Performance degradation	Extent of Sr surface segregation	Probing method	References
YSZ|LSC film	PO_2: ultra-high vacuum; *T*: 350–370 °C; *I*: several μA	–	Increased by cathodic	In situ XPS	[137]
YSZ|LSC film; YSZ|LSC/$(La,Sr)_2CoO_4$ bi-layer film	PO_2: 1×10^{-6} mbar; *T*: 650 °C; *E*: 0.5–1.5 V	Cathodic versus anodic	Cathodic > anodic; Segregated Sr by cathodic reduced by anodic	In situ synchrotron XPS	[88]
YSZ|LSCF film	*T*: 600–750 °C; *E*: −2 to 2.5 V	Cathodic versus anodic	Cathodic > anodic	Ex situ XPS	[90]
GDC|LSCF film	*T*: 600 °C; *j*: 2 mA cm^{-2}; *t*: 540 h	Anodic > cathodic	Cathodic > anodic co segregation	Ex situ TEM, EDS mapping	[138]
YSZ film|GDC|LSCF–GDC	*T*: 850 °C; *j*: 0.5 A cm^{-2}; *t*: 1000–2400 h	Anodic > cathodic	Anodic > cathodic	Ex situ 2D/3D synchrotron XRD and XRF, FIB-SEM, STEM-EDS	[154]
LSCF–SDC |SDC|YSZ|SDC|LSCF–SDC	*T*: 900 °C; *j*: 0.5 A cm^{-2}; *t*: 5500 h	Cathodic > anodic	Cathodic > anodic	Ex situ SEM-EDS	[152]
LSCF|GDC|LSCF	*T*: 800 °C; *E*: 100–600 mV; *t*: 48 h	Cathodic > anodic	Cathodic > anodic	Ex situ XAS	[153]
YSZ film|LSCF, without sintering	*T*: 750 °C; *j*: 0.5 A cm^{-2}; *t*: 100 h	Cathodic > anodic	Cathodic > anodic	Ex situ ToF-SIMS, FIB-SEM, STEM-EDS	[146, 155, 156]
YSZ film|LSCFN electrodes, without sintering	*T*: 750 °C; *j*: 0.5 A cm^{-2}; *t*: 100 h	Cathodic > anodic; degradation by cathodic is recovered by anodic	Cathodic > anodic	Ex situ FIB-SEM, STEM-EDS	[91]
YSZ pellet|LSCF, sintered at 900 °C for 2 h	*T*: 800 °C; *j*: 1 A cm^{-2}; *t*: 158 h	Enhanced stability by anodic	Decreased surface Sr by anodic	Ex situ XPS	[157, 158]

formation of electrode (LSM and LSCF)/electrolyte (YSZ and GDC) interfaces, but also lead to Sr segregation and diffusion, forming a Sr-rich layer and eventually a $SrZrO_3$ secondary phase at the YSZ surface in the case of LSC-based electrode/YSZ electrolyte interfaces [146–148]. In addition, further polarization can accelerate Sr segregation and $SrZrO_3$ reaction layer formation, which will lead to the disintegration of LSCF structures at the electrode/electrolyte interface (Fig. 7) [146]. These findings indicate that cathodic polarization can accelerate SrO surface segregation and kinetically promote the chemical reaction between LSCF and YSZ at 750 °C under polarization conditions. Alternatively, The et al. [149] studied LSCF electrodes in the anodic mode at 1 A cm^{-2} and 780 °C for 9000 h and detected the growth of a $SrZrO_3$ layer at the YSZ/GDC interface and the partial de-mixing of LSCF [149–151]. Choi et al. [138] further observed the significant degradation of an LSCF–GDC electrode after anodic polarization at a high current density of 2 A cm^{-2} under 700 °C for 1300 h, in which the electrode/electrolyte interface partly delaminated and Co and Sr accumulated at the electrode/electrolyte interface near the delaminated region.

To clarify the effects of polarization current direction on the activity of LSC-based electrodes, Shimura et al. [152] studied symmetric LSCF–SDC composite electrodes on YSZ electrolytes with dense SDC barrier layers under polarization at 900 °C and 0.5 A cm^{-2} for 5500 h. Here, these researchers reported that the overpotentials under anodic and cathodic modes remained constant over the operational duration in which the cell ohmic resistance increased from 0.5 to 0.8 Ω cm^2 after cathodic polarization, whereas the increase after anodic polarization was very small. Elemental analysis further showed significant Sr accumulation at the YSZ/SDC interlayer interface after cathodic polarization, which was consistent with cell ohmic resistance increases under cathodic polarization. Finsterbusch et al. [153] also prepared symmetric LSCF electrodes on GDC electrolytes and applied a constant DC voltage at 800 °C for 48 h in which gaseous Cr was fed as a tracer to catch segregated Sr cations at the surface through the formation of $SrCrO_4$. Here, these researchers reported that Sr surface segregation can be inhibited by anodic polarization but that the inhibition effect became less evident as anodic overpotentials increased. Sr surface segregation increased at lower cathodic overpotentials, but decreased at higher cathodic overpotentials. Different results were reported on typical Ni–YSZ/YSZ/LSCF–GDC cells with high degradation rates in the electrolysis mode than in fuel cell mode [154].

Our group also investigated the effects of polarization current direction on Sr segregation in LSCF oxygen electrodes directly assembled on Ni–YSZ hydrogen electrode-supported YSZ electrolytes [146, 155, 156]. The LSCF/YSZ interfaces were in situ formed in the early stage of polarization at 750 °C as evidenced by decreased cell ohmic resistance and formation of contact marks on the YSZ electrolyte. And with two identical cells operating at 0.5 A cm^{-2} and 750 °C for 100 h, it was found that the operating stability of the cell under cathodic polarization deteriorated drastically, whereas significant performance enhancements were observed for the cell under anodic polarization (Fig. 8) [156]. And although a Sr-rich layer formed on both YSZ surfaces, the Sr-rich layer was ~ 30 nm after cathodic polarization and was much thicker than the 10-nm layer observed after anodic polarization. Similarly, Pan et al. [157, 158] directly sintered LSCF electrodes onto a barrier layer-free YSZ electrolyte at 900 °C and observed enhanced electrode operating stability under anodic polarization at 1 A cm^{-2} and 800 °C for 158 h as compared with the performance decay under open-circuit conditions.

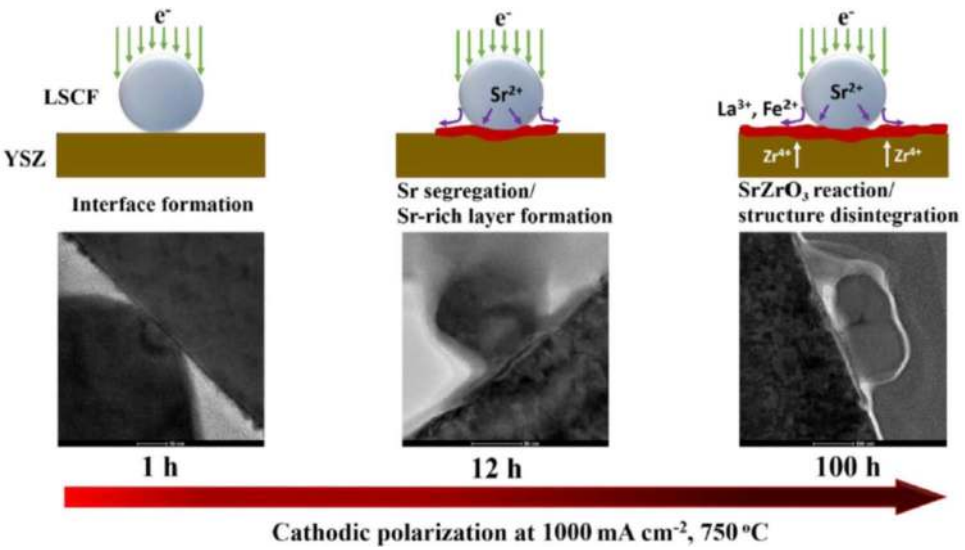

Fig. 7 Scheme of the effect of polarization time at 1 A cm^{-2} and 750 °C on electrode/electrolyte interface formation, Sr segregation and diffusion and Sr-rich and (Fe,La,Y)-containing $SrZrO_3$ reaction layer formation at the LSCF/YSZ interface region. Reproduced with permission from Ref. [146]. Copyright 2018. The Electrochemical Society, Inc.

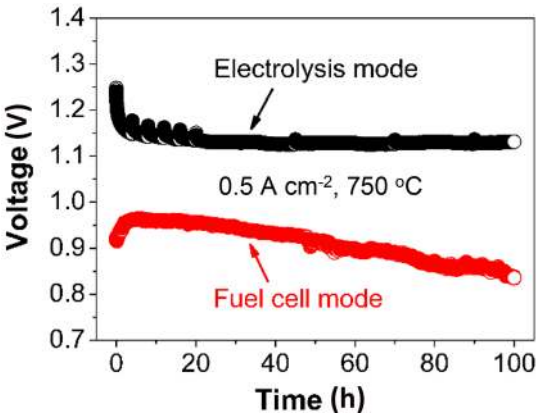

Fig. 8 Stability plots of single cells with LSCF oxygen electrodes assembled on YSZ electrolyte films under fuel cell and electrolysis modes. Reproduced with permission from Ref. [156]. Copyright 2018, Elsevier

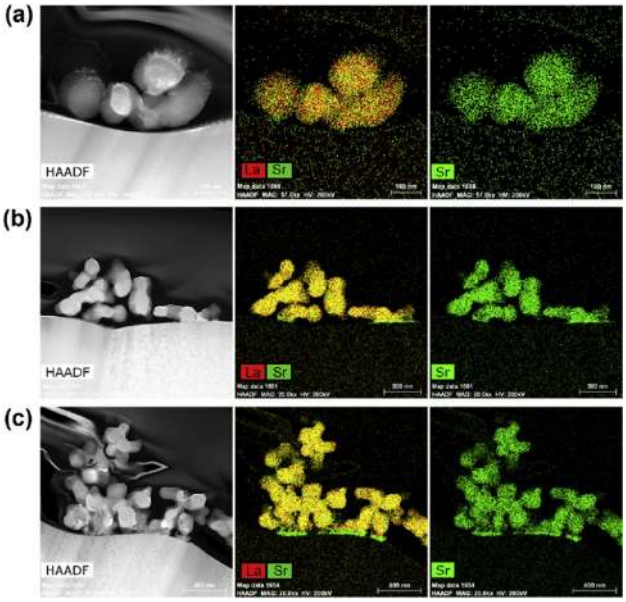

Fig. 9 HAADF images and elemental maps of LSCFN electrodes after cyclic polarization at 0.5 A cm^{-2} and 750 °C with varied time periods and durations: **a** 12-h cathodic polarization/12-h anodic polarization for 48 h, **b** 12-h cathodic polarization/12-h anodic polarization for 240 h and **c** 4-h cathodic polarization/4-h anodic polarization for 224 h. Reproduced with permission from Ref. [91]. Copyright 2018, Elsevier

He et al. [91] further investigated the effects of cyclic cathodic and anodic polarization on Sr segregation using a 10% Nb-doped LSCF (LSCFN) electrode assembled on a YSZ electrolyte and reported that although electrode performances severely degraded through cathodic polarization at 0.5 A cm^{-2} and 750 °C, it can largely be recovered by subsequently switching to the anodic polarization mode. This suggests that Sr surface segregation and accumulation at electrode/electrolyte interfaces as induced by cathodic polarization can be significantly mitigated through subsequent operation in the anodic polarization mode. However, the degree of performance reversibility and Sr segregation was dependent on the time duration of cycles. LSCFN electrode performances were largely reversible in the case of 12-h cathodic polarization/12-h anodic polarization cycles, whereas performance degradation occurred in the case of cyclic polarization with a shorter time period of 4-h cathodic polarization/4-h anodic polarization. Here, FIB-SEM and elemental mapping results indicated that for cyclic polarization using 4-h cathodic polarization/4-h anodic polarization cycles, significant Sr segregation and deposition at the electrode/electrolyte interface occurred after 224 h, whereas for cyclic polarization using 12-h cathodic polarization/12-h anodic polarization cycles, Sr accumulation at the interface was negligible (Fig. 9) [91].

In another study, Barnett et al. [82, 159] investigated the effects of current switching on surface segregation and performance stability in symmetrical LSCF electrodes on GDC electrolytes. Here, these researchers performed current switching at 700 °C for 1000 h under varied current densities (0.7, 1.0 and 1.5 A cm^{-2}) and observed that performance degradation was proportional to the level of current density [159]. To estimate the level of SrO surface segregation, these researchers also stirred the tested LSCF electrodes in ultrapure water for 10 min to seize the water-soluble Sr cations and used ICP-OES to analyse the solution. The results indicate that after current switching, the amount of surface-segregated Sr was higher than that of the as-prepared electrode and the electrode annealed under identical conditions without polarization. It has also been found that the effects of current density were dependent on operating temperature [82] in which at lower temperatures (650–700 °C), the performance degradation of LSCF electrodes increased with increasing current densities, whereas at a higher temperature of 750 °C, operating stability improved with increasing current densities.

Overall, the discrepancies in the effects of influential factors on Sr segregation as reported by different groups may be related to the fact that because Sr segregation is critically influenced by a variety of factors, the differences in sample preparation processes, surface chemistry, surface strains, surface morphology, atmospheres, impurities and polarizations can have a critical effect on observed Sr surface segregation. Therefore, it is important to conduct surface segregation studies under carefully controlled conditions.

4 Driving Forces of Surface Segregation

4.1 Open-Circuit and Annealing Conditions

Although numerous theories exist regarding the mechanism or the driving force of Sr surface segregation in perovskite oxides under open-circuit and/or annealing conditions, the most accepted ones involve electrostatic and elastic interactions [52, 103, 116, 160]. In this review, only the main points are briefly summarized.

Because Sr^{2+} dopant possesses a 5.9% larger ionic radius than the host cation La^{3+}, Sr^{2+} cations experience compressive strain in LSM lattices that can be relaxed through surface migration. As a result, elastic interactions have been proposed as a driving force for SrO surface segregation in LSM [31, 53, 126, 128] and have proved useful in the explanation of many segregation related phenomena. For example, Jalili et al. [108] reported a higher tendency of Sr segregation on tensile strained LSM surfaces due to the larger spacing available for the accommodation of Sr cations with reduced elastic energy on the surface than in the bulk. Lee et al. [116] also reported that the extent of dopant segregation was proportionally dependent on the size of dopants. Observed increases in Sr surface segregation at higher oxygen partial pressures can also be explained by elastic interaction, in which higher oxygen pressures can incorporate oxygen into lattices and contract lattices, whereas lower oxygen pressures can expand lattices upon oxygen loss. Because of this, the shrinkage of LSM lattices under high oxygen partial pressures can lead to increased dopant strain energy and accelerated Sr surface segregation. This was further confirmed by calculations using first-principles thermodynamics [161].

Surface oxygen vacancy concentrations tend to increase with decreasing oxygen partial pressures [162, 163]. Because of this, Fister [118] proposed that electrostatic interactions are the driving force for SrO segregation in LSM and are related to the interactions between positively charged oxygen vacancies and net negative charges due to the substitution of Sr^{2+} for La^{3+} in LSM lattices. Large concentrations of positively charged surface oxygen vacancies (+2) can drive substituted Sr cations from the bulk to the surface through electrostatic interaction to maintain local electroneutrality. Electrostatic interactions between surface oxygen vacancies and Sr cations can also be used to explain the Sr surface segregation phenomenon of LSC and LSCF [125, 164, 165]. For example, Kuyyalil et al. [164] applied the electrostatic interaction mechanism to explain the formation of SrO layers on LSCF (100) film surfaces at a very low annealing temperature of 150 °C in which prior to annealing, surface oxygen vacancies were created by sputtering the LSCF film with low-energy Ar^{+} ions.

Lee et al. [116] further identified both elastic and electrostatic interactions as driving forces for surface segregation, using (La,D)MnO_3 (D = Ca, Sr and Ba) as a model system (Fig. 10). The tendency to segregate to the surface increases with increased dopant sizes (the radii of Ca^{2+}, Sr^{2+}, Ba^{2+} and La^{3+} with CN = 12 are 1.34, 1.44, 1.61 and 1.36 Å, respectively [131]). Here, a smaller size mismatch between the host and dopant cations can suppress dopant segregation due to reduced elastic interactions. D^{2+} substitution of A-site La^{3+} in perovskites produces negatively charged D'_{La} defects, which can be compensated by the formation of positively charged oxygen vacancies, $V_O^{\cdot\cdot}$ on the surface. The electrostatic interaction between D'_{La} and $V_O^{\cdot\cdot}$ can then drive the substitutional D^{2+} cations towards the surface. In another study, Ding et al. [103] took into account both strain relaxation and surface charge minimization as driving forces for Sr surface segregation on LSCF, in which DFT calculations indicated that the net effect of surface oxygen vacancies enhanced Sr surface segregation because the increase in surface charge overrode the induction of compressive strain. Sr surface segregation also depends on the type of B-site cations. For example, the substitution of Fe with Co can induce tensile strain and increase surface charge, thus increasing Sr surface segregation. Because of this, the application of compressive strain and the reduction in surface charge are effective strategies to suppress Sr surface segregation. This also indicates that electrostatic interactions play a dominant role in Sr segregation in LSCF [125, 164, 165].

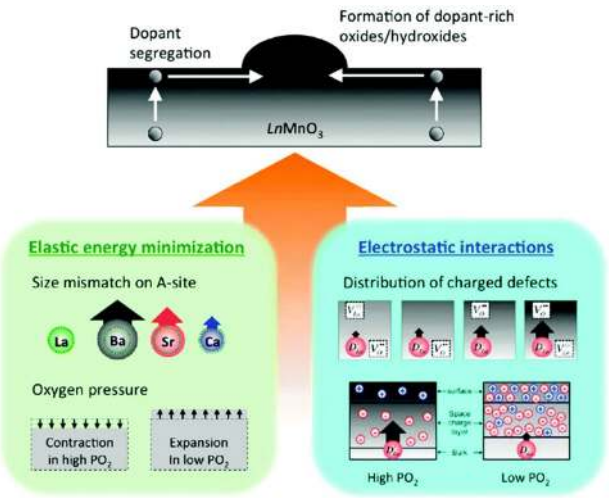

Fig. 10 Driving forces for A-site segregation in a perovskite $LaMnO_3$ system as a case study. Reproduced with permission from Ref. [116]. Copyright 2013, American Chemical Society

4.2 Polarization Conditions

Sr surface segregation behaves differently under cathodic and anodic polarization conditions. In the case of LSM electrodes, cathodic polarization inhibits Sr segregation, whereas anodic polarization promotes Sr segregation in which incorporation and segregation of Sr species on LSM surfaces are supported by the activation/deactivation of LSM electrodes for ORR under the influence of cathodic/anodic polarization [53, 126, 127]. Here, the significant redistribution of segregated Sr species on LSM and LSCrM electrode surfaces can be studied by using in situ probing techniques [66, 135, 166].

The effects of polarization on Sr segregation/incorporation induced by cathodic/anodic polarization are complicated, as indicated by the activation and deactivation process of oxygen reduction reaction on LSM [126, 128]. LSM-based materials are predominantly electronic conductors with negligible oxygen ion conductivities [167]. In fact, in the case of Sr-doped $LaMnO_3$, Sr substitution of A-site La leads to the formation of electron holes, and at SOFC operating temperatures, the electron holes are localized onto specific Mn ions, forming Mn^{4+} ions, $Mn_{Mn}^{\cdot}$ or electron holes, $h^{\cdot}$ [168]. This is consistent with the p-type electronic conductivity of LSM-based materials [169]. The neutrality condition can be simply described as:

$$SrO \overset{LaMnO_3}{\longrightarrow} Sr'_{La} + Mn^{\cdot}_{Mn} + O^{x}_{O} \tag{3}$$

Under cathodic polarization conditions, the generation of positively charged oxygen vacancies, $V^{\cdot\cdot}_{O,LSM,surface}$, is a dominant process in LSM electrodes for ORR. The subscript surface indicates that the positively charged oxygen vacancies generated under cathodic polarization are primarily on the LSM surface in the vicinities of the three-phase boundary (TPB). Cathodic polarization substantially reduced the formation energy of oxygen vacancies, and thus, the formed oxygen vacancies significantly enhance the ORR [130, 170]. Considering the high concentration of positively charged oxygen vacancies on the LSM surface, the electroneutrality can also be established by incorporating the segregated SrO into the La lattice, forming negatively charged Sr'_{La}. Such incorporation of SrO through the electrostatic attractive interaction can be expressed as:

$$2SrO_{surface} \overset{\text{Cathodic polarization},LaMnO_3}{\longrightarrow} 2Sr'_{La,surface} + V^{\cdot\cdot}_{O,LSM,surface} + 2O^{x}_{O} \tag{4}$$

In this case, oxygen vacancies are formed under the influence of cathodic polarization and not due to the Sr substitution. As discussed above, the charge compensation through the oxidation of B-site Mn ions (Eqs. 1 and 2) would mainly drive the B-site Mn cations to the surface via the elastic interaction, while incorporation of segregated SrO into La lattice sites would be the alternative charge compensation mechanism for the oxygen vacancy formed under cathodic polarization conditions. The incorporation of segregated SrO species can be a fast process due to the strong electrostatic attractive force between the positively charged $V^{\cdot\cdot}_{O,LSM,surface}$ and negatively charged Sr'_{La}. Fast incorporation reaction of segregated Sr into LSM lattices is consistent with the observed activation effect and reduced Sr species at LSM electrode surfaces [53, 66, 117, 135].

Under anodic polarization conditions, oxygen excess occurs, similar to the oxygen excess of LSM materials at high oxygen partial pressures [130, 169]. The presence of oxygen excess in the form of negatively charged O''_{excess} ions (note: the oxygen excess could exist as negatively charged cation vacancies such as V'''_{La} due to the compact nature of LSM perovskite structure. Nevertheless, electronically O''_{excess} and V'''_{La} would function similarly due to the fact that both are negatively charged point defects) would push the negatively charged Sr'_{La} out of the lattice to the surface by the repulsive electrostatic interaction. The Sr segregation due to the excess oxygen in LSM under anodic polarization can be expressed as follows:

$$Sr'_{La} \overset{\text{Anodic polarization},O''_{excess}\text{ or }V'''_{La}}{\longrightarrow} SrO_{surface} \tag{5}$$

This anodic polarization-induced electrostatic interaction can subsequently drive Sr segregation to the LSM surface. Therefore, the driving force for Sr segregation at LSM electrode surfaces under polarization is most likely the result of oxygen nonstoichiometry modulated electrostatic interaction on the LSM surface induced by cathodic/anodic polarization. The observed Sr incorporation rather than Sr segregation under cathodic polarization implies that elastic interactions due to the size mismatch between the substitute Sr and host La cations are compensated by the electrostatic interactions of the generated oxygen vacancies and are not key factors dominating Sr surface segregation/incorporation in LSM under polarization conditions. The Sr segregation/incorporation processes on LSM under polarization conditions are schematically shown in Fig. 11.

The effects of polarization on Sr segregation in LSC-based electrodes are the opposite of those observed in LSM electrodes. Cathodic polarization promotes Sr segregation, whereas anodic polarization inhibits Sr segregation [91, 146, 147]. These polarization effects can be explained based on the nature of LSC-based electrodes such as LSCF. LSCF electrode materials are well-known MIECs with high oxygen ion conductivity [171, 172], which results in significant differences in electrode behaviours between LSCF and LSM. Cathodic polarization will cause the excess in oxygen vacancies on the electrode surface of LSCF. As a result, the increased accumulation of positively charged oxygen vacancies at the electrode surface would enhance electrostatic

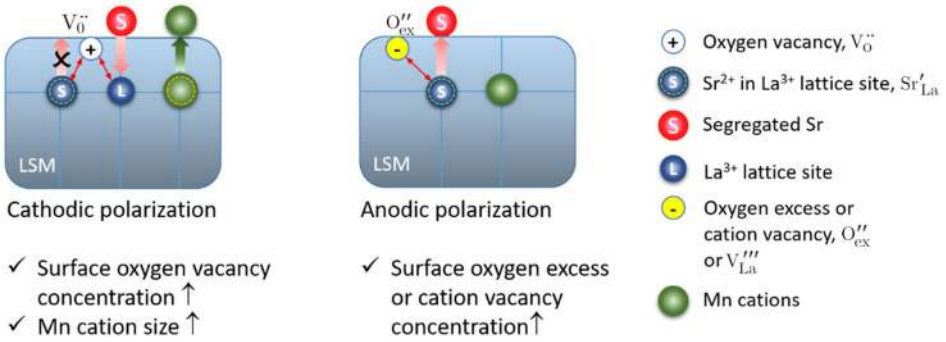

Fig. 11 Segregation and incorporation of Sr and Mn cations on LSM electrodes under polarization conditions. Locations and sizes of ions are not to scale

interactions. This combined with intrinsic elastic interactions subsequently drives Sr segregation. The observed Sr segregation rather than Sr incorporation under cathodic polarization is an indication of much stronger elastic interaction in the case of LSCF as compared to that in LSM. Under anodic polarization, oxygen vacancy concentrations at the electrode surface are significantly reduced and the substituted Sr at the La site would be held by the attractive force between negatively charged Sr'_{La} and positively charged $V_O^{\cdot\cdot}$ in the bulk, which will overcome the elastic interaction and result in decreased driving force for Sr segregation, thus inhibiting Sr segregation. This in turn suggests the diminished role of elastic interactions on Sr segregation in LSC-based electrodes under polarization conditions. As a result, the driving force for Sr segregation in LSC-based electrodes under polarization is primarily related to the significant change in electrode surface properties, particularly positively charged oxygen vacancy concentration at surfaces under cathodic and anodic polarization conditions. This is schematically shown in Fig. 12.

5 Relationship Between Surface Segregation and Electrochemical Activity

5.1 Surface Segregation and Activation

Sr segregation in LSM is closely related to the activation phenomenon of LSM-based electrodes for O_2 reduction reactions in SOFCs under the influence of cathodic polarization [53, 68, 173]. This activation effect can be classified as a performance enhancement under the influence of polarization in which Jiang et al. [53] demonstrated the first direct evidence of the intrinsic relationship between the activation phenomenon and surface segregation through the polarization behaviour of a weakly acid-etched freshly prepared LSM electrode in 2001. In this experiment, an as-prepared $La_{0.72}Sr_{0.18}MnO_3$ electrode was washed with 1 M HCl acid solution prior to cathodic polarization, and the ICP-AES analysis of the solution collected after HCl etching of the LSM electrode coating showed an atomic ratio of La/Sr/Mn based on La concentration as 0.74/8.4/15.8, which was significantly different from the measured ratio of 0.74/0.15/1 for the LSM coating. Here, the results suggested that the high content of Sr on the LSM surface was an indication of Sr segregation and enrichment on the LSM surface. The electrochemical activity of freshly prepared LSM electrodes for O_2 reduction can be enhanced significantly through cathodic polarization (i.e. activation), and such activation phenomenon is much less pronounced after the acid treatment of the electrode (Fig. 13) [53]. The electrode polarization resistance for the reaction on the acid-treated LSM in 1 M HCl solution was 0.84 Ω cm^2, which was much smaller than 6.2 Ω cm^2 for the reaction on LSM without acid treatment. In addition, the reduction in polarization resistance under cathodic polarization treatment was also much smaller.

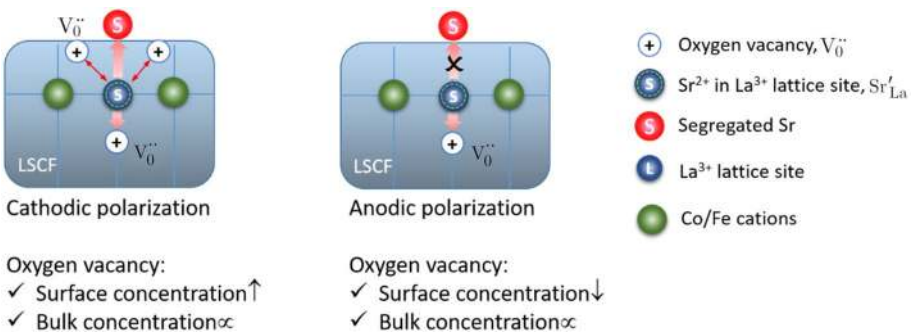

Fig. 12 Segregation and inhibition of Sr species on LSCF under polarization conditions. Locations and sizes of ions are not to scale

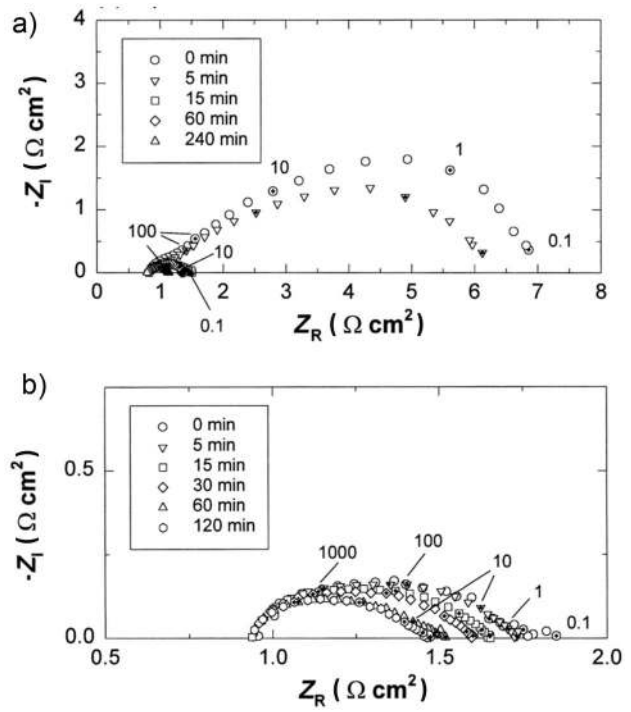

Fig. 13 Impedance plots of a $La_{0.72}Sr_{0.18}MnO_3$ electrode **a** before and **b** after acid treatment with 1 M HCl solution for ORR as a function of cathodic polarization at 200 mA cm^{-2} and 900 °C in air. Impedance was measured under an open circuit and frequency numbers are shown in Hz. Reproduced with permission from Ref. [53]. Copyright 2001, Elsevier Inc.

La O' et al. [174] also observed significantly enriched La on annealed and quenched LSM and reported that cathodic polarization considerably decreased electrode impedance as associated with the reduction of surface La and increase in surface Sr and Mn species on LSM adjacent to the three-phase boundary. Because segregated dopant cations such as SrO and BaO are electrically insulated as revealed by scanning tunnelling microscopy and spectroscopy (STM/STS) [114, 116], their occupation on electrode surfaces can have detrimental effects on electrocatalytic activity. For example, Wang et al. [83] reported that the surface segregation of SrO on annealed LSCF electrodes led to decreased surface exchange rates (k) by ~ 50% and oxygen diffusion coefficients (D^*) by 50%. Yokokawa et al. [175] recently also reported that Sr deficiencies in the LSCF bulk can lead to decreased k and D^* due to positively charge oxygen vacancy can also be compensated by incorporating the surface-segregated SrO into the La lattice, forming negatively charged Sr'_{La} and decrease in oxygen vacancy concentrations. Chen et al. [102] further proposed deterioration mechanisms of SrO segregation on the ORR kinetics of STF electrodes involving: (1) the inhibition of electron transfer from the bulk of STF to the oxygen species adsorbed on the surface and (2) the decrease in surface oxygen vacancy concentrations for the incorporation of oxygen into STF lattices. Lu et al. [82] suggested that the removal of surface-segregated SrO through etching in diluted acid or water can significantly enhance the electrocatalytic activity of LSCF electrodes for ORR.

The initial state of LSM lattices can be examined to explain the activation phenomenon. The segregated SrO species on LSM surface occupies the active sites and significantly inhibits the dissociation and diffusion of oxygen, leading to the very high electrode polarization resistance. Here, the removal of SrO species can be achieved through chemical processes such as weak acid etching as well as with the application of cathodic polarization/current passage through the incorporation of segregated SrO species into LSM perovskite lattices due to the charge compensation between the positively charged oxygen vacancies formed and the incorporated negatively charged Sr'_{La} defects (Fig. 11). The incorporation of SrO under cathodic polarization conditions is kinetically favourable and a fast process due to the strong oxygen vacancy modulated electrostatic interactions.

To clearly elucidate the effects of segregated cations on the electrocatalytic activity of LSC films, Rupp et al. [176] developed a combined PLD and electrochemical measurement approach to monitor electrochemical performance changes during surface decoration in a PLD chamber. Here, these researchers intentionally deposited a 4% Sr monolayer onto an LSC surface using PLD to achieve severe performance deactivation and found that this result was in good agreement with the aforementioned performance degradation as induced by in situ SrO surface segregation at elevated temperatures. The deposition of Co using PLD caused performance activation in LSC films. The dominant role of B-site cations as active sites for ORR has also been reported in the case of LSM [114, 177].

Researchers have also reported the promotional effects of SrO decoration on electrode activity [34, 178, 179]. For example, Mutoro et al. [178] deposited 50%–80% of an LSC film surface with SrO nanoparticles using PLD and found that the surface exchange coefficient was remarkably enhanced by an order of magnitude. Here, these researchers attributed the enhancement of the Sr-decorated surface to the generation of a catalytically active LSC214 RP phase at the interface between SrO particles and the LSC film [42]. The positive effects of SrO and BaO nanoparticle infiltration into porous electrodes have also been reported [179–183]. For example, Hong et al. [179] infiltrated 1.25–8.75 wt% SrO into $La_{0.8}Sr_{0.2}FeO_3$ (LSF) scaffolds with annealing at 800 °C to prepare a $(La,Sr)_2FeO_4$ (LSF214) RP phase and reported significantly enhanced ORR activities. Chen et al. [184] further infiltrated barium nitrate into a PBCC electrode and observed that the PPD of the single cell at 750 °C increased from 0.85 to 1.15 W cm^{-2} following the surface modification and detailed analyses demonstrated

that the in situ formation of a highly active nanostructured barium cobaltite was critical to ORR activity and durability. Recently, Li et al. [34] also investigated SrO decoration on LSC film surfaces through infiltration and obtained polarization resistances ~ 30 times lower than that of pristine LSC films in which after annealing at 600 °C, the infiltrated SrO phase evolved into isolated islands and possessed a Sr-rich perovskite structure. Here, these researchers combined their experimental observations with DFT calculations and hypothesized that the surface infiltrated Sr^{2+} cations had a high tendency to seize surface defective sites and inhibit intrinsic Sr flux, thereby suppressing SrO segregation. Despite this, excessive SrO infiltration can still lead to surface passivation. Therefore, the promotional effects of SrO surface decoration [34, 178, 179] may be related to interactions at the interface between SrO and perovskite oxides, forming a highly active Sr-containing perovskite phase. Nevertheless, the use of infiltration to study the effects of decorated SrO needs to be cautioned because infiltration can not only introduce nanoparticles but also clean the surface of infiltrated electrodes, meaning that the careful control of infiltrated electrodes/systems is required [185, 186].

5.2 Reactivity of Segregated Cation Species with Volatile Impurities

Various volatile impurities exist in SOC stacks, such as gaseous CrO_3 from chromia-forming metallic interconnects and high-temperature alloys used in Balance-of-Plant (BoP) components, SO_2, CO_2 and H_2O from airstream and boron species from borosilicate glass sealants. Surface-segregated cations tend to interact actively with these volatile impurities, leading to the deposition of impurities, microstructural changes and operating instability [39, 48, 49, 57, 187–203].

5.2.1 Cr

Although there are no clear indications of Cr deposition on electrodes in the case of LSM electrode exposure to gaseous CrO_3 under open-circuit conditions [204], Cr preferentially deposits to LSM electrode/electrolyte interfaces under cathodic polarization conditions due to the chemical reaction between low valence Mn^{2+} and CrO_3 according to the proposed nucleation theory [49, 132, 205]. Here, low valence Mn^{2+} cations can readily segregate under cathodic polarization conditions and their high mobility enables their distribution at the electrode/electrolyte interface [67, 68, 71]. These Mn^{2+} cations can subsequently act as a nucleating agent to combine with CrO_3 to form the Mn–Cr–O nuclei and initiate the deposition of CrO_3 and the $(Mn,Cr)_3O_4$ spinel phase onto YSZ surfaces and LSM/YSZ interfaces. In terms of anodic polarization conditions, LSM electrodes are exposed to oxygen-rich environments and Mn cations tend to adopt higher valences (+3 and +4), which lead to LSM lattice contraction. The formation of negatively charged excess oxygen can also cause Sr segregation on LSM surfaces, leading to the formation of $SrCrO_4$ at the electrode/electrolyte interface under the anodic polarization conditions [136].

Surface-segregated Sr cations on LSCF also play a key role in determining Cr deposition because segregated SrO cations tend to form the Sr–Cr–O nuclei to initiate $SrCrO_4$ and Cr_2O_3 deposition [49, 132, 206]. For example, Zhao et al. [86] annealed LSCF pellets at 800 °C for 96 h in the presence of Cr_2O_3 powder in dry air and observed the significant growth of surface-segregated SrO particles. LSCF pellets were also annealed in the presence of Cr_2O_3 in wet air, which led to greatly accelerated Sr segregation with roughened LSCF grain surfaces and the formation of nanopores or pinholes. Here, this was attributed to the combined effects of the high volatility of $CrO_2(OH)_2$ formed in humid air [207] and the acceleration effect of moisture on Sr surface segregation [195–197]. Wang et al. [208] also reported that the amount of $SrCrO_4$ generated on LSCF pellet surfaces decreased with decreasing temperature in the range of 700–900 °C and that decreases in temperature can significantly reduce the amount of surface-segregated SrO and partial pressure of CrO_3, leading to significant reductions in Cr deposition. Wei et al. [209] further studied cation segregation and Cr deposition on double-perovskite oxide $PrBaCo_2O_{5+\delta}$ (PBCO) and observed that after high-temperature annealing in O_2 atmosphere, both Ba and Co diffused out of the lattice to form BaO and Co_3O_4 precipitates on the surface. It was found that in the presence of volatile Cr species, $BaCrO_4$, but not $CoCr_2O_4$, was observed on PBCO electrode surfaces, indicating that Cr deposition preferentially occurred on segregated BaO rather than on Co_3O_4 precipitates. The interactions between segregated species and Cr at cathodes under the SOFC operation mode can be described with a generalized nucleation deposition theory in which Cr deposition is essentially a chemical process in nature that is initiated by the nucleation reaction between high valence Cr species and a nucleation agent as follows [49]:

$$CrO_{3(g)} + N_{(s)} \rightarrow Cr{-}N{-}O_{(nuclei,s)} + O_{2(g)} \quad (6)$$

$$Cr{-}N{-}O_{(nuclei,s)} + CrO_{3(g)} \rightarrow Cr_2O_{3(s)} \quad (7)$$

$$Cr{-}N{-}O_{(nuclei,s)} + CrO_{3(g)} + N_{(s)} \rightarrow \text{solid compounds} \quad (8)$$

in which $N_{(s)}$ represents a nucleation agent. Here, nucleation agents include Mn,Sr and Ba species generated under high-temperature annealing and/or polarization conditions on perovskite-based electrode surfaces and can be on electrode and electrolyte surfaces or at electrode/electrolyte interfaces. Further reactions between the Cr–N–O nuclei, gaseous Cr

species and nucleation agents can also lead to the deposition and formation of Cr_2O_3 and solid compounds such as $(Cr,Mn)_3O_4$, $SrCrO_4$ and $BaCrO_4$.

For LSCF electrodes exposed to CrO_3 environments, Cr preferentially deposits onto outermost electrode surfaces to form dense $SrCrO_4$ layers [188, 206, 210–212] and to a lesser extent at the interface between LSCF electrodes and GDC barrier layers [213, 214]. This is evidenced by Cr distribution in LSCF electrodes after operation for 10000 h (Fig. 14) [211]. Here, the preferential formation of $SrCrO_4$ on electrode surface layers can drive the diffusion of segregated SrO from electrode/electrolyte interfaces to electrode surfaces and therefore cause Sr deficiency in LSCF electrodes in interfacial regions [188, 206, 210–212].

5.2.2 SO_2

Sulphur in air streams can significantly affect the performance and durability of SOFCs [191, 215, 216]. For example, Wang et al. [217] studied the mechanism and kinetics of sulphur deposition on LSM electrodes at 700 °C and 800 °C in 1 ppm and 10 ppm SO_2 and reported that the deposition of SO_2 was likely controlled by the nucleation reaction between surface-segregated SrO and SO_2 to form $SrSO_4$ on LSM electrode surfaces. Here, segregated SrO species act as both the nucleation agent and the reactant and the formation of $SrSO_4$ in turn can promote Sr segregation, leading to LSM Sr deficiency and driving the chemical reaction to the LSM/YSZ interface. High oxygen activities and SrO segregation can also lead to the formation of Sr/La zirconate at electrode/electrolyte interfaces.

$$SO_2 + SrO \rightarrow SrSO_4 \tag{9}$$

Xiong et al. [191] also investigated the sulphur poisoning of LSM electrodes in highly concentrated 0.01% SO_2 in air and reported that the LSM electrode was relatively stable during cathodic polarization at 800 °C for 5 h. On the other hand, Liu et al. [190] tested a double-layer oxygen electrode with an LSM–ScSZ inner layer and an LSM outer layer in 20 ppm SO_2 and reported that after cathodic polarization at 800 °C for 1000 h, $SrSO_4$ particles were observed around the LSM particles in both layers of the electrode. Wang et al. [218] further reported that the deposition of sulphur and formation of $SrSO_4$ were at the LSM/YSZ interface in the presence of 1 ppm SO_2 at 800 °C under anodic polarization conditions and attributed this to the fact that anodic polarization can promote SrO segregation at the LSM close to the YSZ electrolyte, promoting the formation of $SrSO_4$ and interfacial delamination.

Compared with LSM, cobaltite oxygen electrodes such as LSC, $Sm_{0.5}Sr_{0.5}CoO_3$ (SSC) and LSCF have much higher tendencies to react with SO_2. For example, Schuler et al. [58, 219] exposed a double-layer oxygen electrode consisting of a LSM–YSZ inner layer and an LSC outer layer to ~ 12 ppb SO_2 and reported that after operation at 800 °C for 1900 h, $SrSO_4$ preferentially deposited onto the LSC layer, in which the formation of more $SrSO_4$ on the cobaltite electrodes as compared with that on LSM electrodes was believed to be due to the higher activity of SrO in cobaltite electrodes [58, 190, 191]. Here, the reaction between SO_2 and LSC is favourable under oxygen-rich atmospheres and can be described by:

$$6La_{0.5}Sr_{0.5}CoO_3 + 3SO_2 + \frac{1}{2}O_2 \rightarrow 3SrSO_4 + Co_3O_4 + 3LaCoO_3 \tag{10}$$

In another study, Bucher et al. [220] exposed LSC pellets in air with SO_2 concentrations ranging from a few ppb

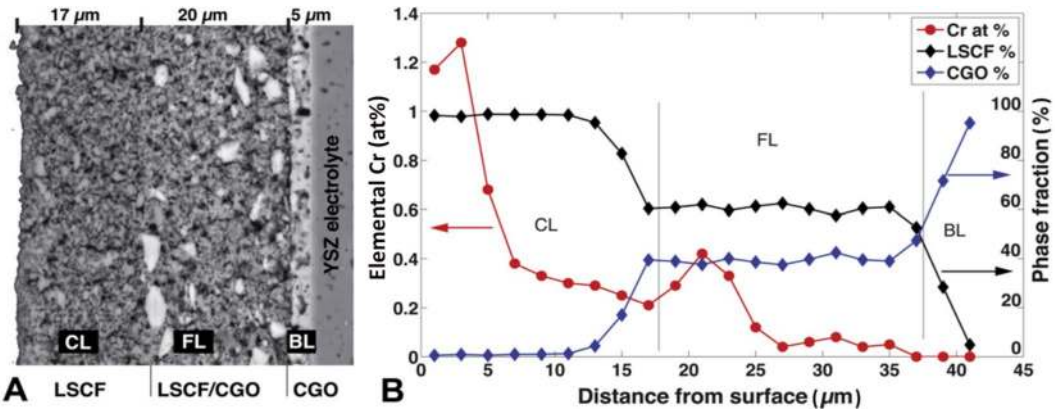

Fig. 14 **a** SEM micrograph of an SOFC cross section showing the LSCF collector layer (CL), the LSCF–CGO ($Gd_{0.1}Ce_{0.9}O_{1.95}$) functional layer (FL), a CGO buffer layer (BL) and the YSZ electrolyte, **b** LSCF and CGO phase profiles with increasing CGO content towards the cathode/electrolyte interface. Reproduced with permission from Ref. [211]. Copyright 2012, Elsevier Inc.

to 2 ppm at 700 °C for 2000 h and observed $SrSO_4$ crystals on the LSC surface in addition to a 100-300-nm-thick nanocrystalline sublayer consisting of $SrSO_4$, $La_2O_2SO_4$ and Co_3O_4. Similarly, Xiong et al. [191] reported that the testing of SSC electrodes under cathodic polarization conditions in 0.01% SO_2-concentrated air at 800 °C for 8 h led to the formation of $SrSO_4$ and $Sm_2O_2SO_4$ at the electrode surface. Wang et al. [215, 221] further exposed LSCF electrodes in 0.1, 1, 10 and 100 ppm SO_2 at 800 °C and reported that degradation became critical with increasing SO_2 concentrations due to the increasing generation of $SrSO_4$ and $CoFe_2O_4$. In addition, sulphur deposition preferentially occurred in the vicinity of the LSCF electrode/GDC electrolyte interface in 0.1 ppm SO_2. The creation of high oxygen vacancy concentrations in electrochemically active regions under polarization conditions is believed to be able to promote SO_2 adsorption and accelerate $SrSO_4$ formation at electrode/electrolyte interfaces [222]. Alternatively, Kushi [223] reported that after exposure in 0.2 ppm SO_2 at 700 °C, sulphur deposition mainly occurred at the electrolyte/electrode interface after anodic polarization, whereas deposited sulphur was widely distributed across the entire electrode after cathodic polarization.

The formation of $SrSO_4$ on LSCF is critically dependent on operating temperature. For example, Wang et al. [224] annealed LSCF pellets in 20 ppm SO_2 at temperatures ranging from 400 to 900 °C and found that $SrSO_4$ formed on LSCF surfaces at high temperatures $\geqslant$ 700 °C, whereas SrS formed at low temperatures < 700 °C. In addition, the surface segregation of Sr and/or Co on LSCF decreased significantly with temperature, whereas sulphur deposition on LSCF surfaces showed a volcano-type dependency on temperature, in which the reaction and formation of $SrSO_4$ were most kinetically active at 700 °C. Wang et al. [225] also reported that LSCF can exhibit severe performance degradation in 1 ppm SO_2 at low temperatures of 650 °C and 700 °C but that degradation was reduced at a high temperature of 800 °C. The results suggest that the severe performance loss at lower temperatures is due to the adsorption of SO_2 on the entire LSCF surface without the formation of sulphates, whereas the less severe performance loss at higher temperatures was attributed to the formation and accumulation of $SrSO_4$, which left some active surface sites available for electrochemical reduction reactions.

The sulphur poisoning behaviour of LSCF electrodes is also dependent on composition. For example, De Vero [226] compared the sulphur poisoning of LSCF films with an A-site excess composition ($La_{0.75}Sr_{0.42}Co_{0.15}Fe_{0.68}O_{3-\delta}$) and a stoichiometric composition ($La_{0.60}Sr_{0.39}Co_{0.20}Fe_{0.81}O_{3-\delta}$) by annealing at 800 °C for 100 h in trace amounts of SO_2 (in the ppb level) and reported that the A-site excess LSCF film exhibited significant $SrSO_4$ formation with severe porosity, whereas only isolated $SrSO_4$ formation was observed in the stoichiometric LSCF film. Here, the partial poisoning by sulphur minimized excessive porosity and enhanced Co-rich oxide precipitation.

5.2.3 Boron

The main source of volatile boron species originates from the use of boron-containing sealing glass in SOCs, such as BO_2 under dry conditions and $B_3H_3O_6$ under wet reducing conditions [227]. To investigate this, Chen et al. [228] annealed LSM and LSCF pellets at 800 °C for 7 and 30 days using borosilicate glass as a boron source and found that the reaction between boron and surface-segregated SrO resulted in the formation of a SrB_2O_4 layer on the outermost surface of the pellets. $LaBO_3$ was also observed underneath the SrB_2O_4 surface layer. Chen et al. [203] further annealed BSCF pellets in gaseous boron at 800 °C for 7 days and observed a Ba- and Sr-rich layer on the surface.

Polarization can significantly affect the distribution of deposited boron. Chen et al. [229, 230] conducted the in situ electrochemical study of boron poisoning in LSM electrodes under cathodic and anodic polarization at 800 °C in which borosilicate glass pellets were placed on top of an LSM electrode as a boron source without direct contact by using a Pt mesh buffer layer. Here, it was found that boron deposition occurred randomly on the LSM electrode surface under open circuit conditions but was driven to the electrode/electrolyte interface region under cathodic polarization, resulted in the formation of $LaBO_3$ and Mn_2O_3 and the disintegration of the LSM perovskite structure (Fig. 15a, b). A $LaBO_3$ layer was also observed at the electrode/electrolyte interface under anodic polarization that led to electrode delamination and failure (Fig. 15c, d). Here, preferential boron deposition at the electrode/electrolyte interface can be attributed to the increased activity of highly energetic La at the LSM lattice sites of the three-phase boundary region under polarization conditions, which can accelerate the reaction rate between boron and energetic La. The in situ boron poisoning of LSCF electrodes under cathodic polarization was also investigated [231]. After cathodic polarization at 700 °C for 20 h, ohmic and polarization resistances were found to have increased by 4 and 12 times, respectively, and significant microstructure changes were observed in the vicinity of the electrode/electrolyte interface (Fig. 15e, f). Here, the thickness of the reaction layer was found to be dependent on the overall electrode thickness, which was 6 μm thick for a 28 μm-thick electrode and 2.5 μm thick for a 6 μm-thick electrode. These microstructural changes can be attributed to the preferential deposition of boron and formation of $LaBO_3$ at the electrode/electrolyte interface of LSCF electrodes.

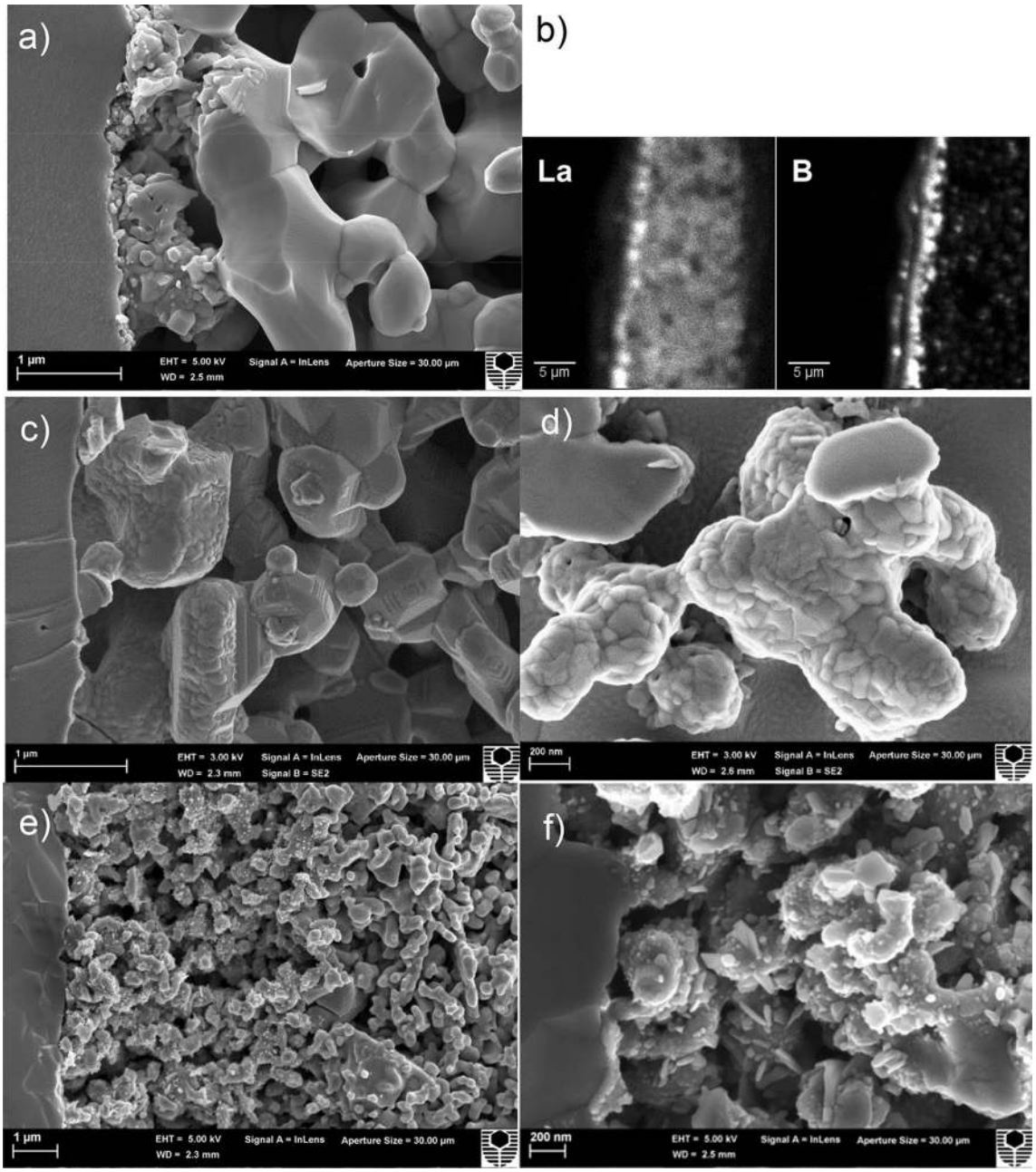

Fig. 15 SEM micrograph and Nano-SIMS imaging of the cross section (**a**–**c**) and the exposed YSZ electrolyte surface (**d**) of LSM electrodes after polarization in the presence of borosilicate glass; (**a**, **b**) after cathodic polarization at 0.2 A cm^{-2} and 800 °C for 100 h; (**c**, **d**) after anodic polarization at 0.050 A cm^{-2} and 800 °C for 8 h; and (**e**, **f**) of the LSCF electrode after cathodic polarization at 0.2 A cm^{-2} and 700 °C for 20 h. Reproduced with permission from Ref. [229–231]. Copyright 2014, Royal Society of Chemistry; Copyright 2015, The Electrochemical Society Inc.; Copyright 2016, Elsevier Inc.

5.2.4 CO_2

The effects of CO_2 on the distribution of surface cations are generally conducted under accelerated conditions. For example, Hu et al. [232] tested LSM electrodes in 0–10% CO_2 containing air in temperatures ranging from 750 to 850 °C and reported the formation of $SrCO_3$ on LSM surfaces based on AES and attenuated total reflectance Fourier transform infrared spectroscopy (ATR-FTIR). Ponce et al. [233] also observed the tendency of CO_2 reacting with SrO at LSM surfaces to form $SrCO_3$. In addition, researchers have reported the minor poisoning effect of CO_2 on the operating stability of LSM electrodes [232, 234]. On the other hand, the poisoning effect of the reaction between CO_2 and SrO on

LSCF is severer. For example, Yu et al. [192] annealed LSCF at 800 °C under a CO_2 containing atmosphere for 9 h and observed the formation of a secondary phase on the surface, which consisted of SrO covered with a capping layer of $SrCO_3$ and Co-rich phases. Chen et al. [39] exposed LSCF electrodes to 1% and 10% CO_2 in air and reported that the impedance of the LSCF electrodes increased significantly with time and that the degree of degradation increased with increasing CO_2 concentrations (Fig. 16a). To gain a deeper understanding of the causes of this degradation, these researchers further exposed LSCF films to 10% CO_2 atmosphere at 500 °C and in situ Raman spectroscopy results showed drastic increases in peaks related to strontium carbonate with increasing exposure times (Fig. 16b). After exposure to CO_2, the LSCF film surface became much rougher (Fig. 16c). DFT calculations also indicated that the growth of $SrCO_3$ resulted from carbonate formation through the strong interaction between CO_2 and Sr cations segregated from the LSCF electrode. In another study, Darvish et al. [234] carried out thermodynamic predictions regarding phase formations in LSCF and suggested the higher tendency of $SrCO_3$ formation at higher P_{CO_2}, lower P_{O_2} and lower temperatures.

Compared with LSCF, BSCF is more vulnerable to attack by CO_2 [235–238]. This is due to the higher tendency of CO_2 adsorption on BSCF surfaces and the formation of Ba-rich carbonates, particularly at higher temperatures, higher CO_2 concentrations and higher Ba doping levels in BSCF [235, 236]. For example, Arnold et al. [239] showed that BSCF bulk samples can be affected down to a depth of 50 µm if exposed to pure CO_2 at 875 °C for 72 h in which two distinctive layers within the reaction zone existed. Here, the outer layer was ~ 5 µm thick and consisted mainly of (Ba,Sr)CO_3, whereas the second layer underneath was ~ 40 µm thick and exhibited plate-like morphology with a mixture of carbonates and Co-/Fe-enriched oxides. Schmale et al. [240] exposed BSCF specimens to 99.9% CO_2 atmosphere at 900 °C and reported the formation of a (Ba,Sr)CO_3 carbonate top layer 1.4–3.0 µm in thickness after annealing for 24 h. The reaction layer increased to 5–7 µm in thickness after prolonging the annealing period to 240 h. In both cases, the Ba/Sr ratio remained at 1.25–1.50.

5.2.5 H_2O

Moisture in air has a detrimental effect on the surface exchange rate and electrocatalytic performance of LSM, LSC and LSCF oxygen electrodes due to the structural damage caused by interactions between surface-segregated cations and moisture [193–197]. For example, moisture can accelerate SrO segregation on LSM. Sharma et al. [241] reported that exposure to 20% moisture enhanced SrO segregation on LSM after annealing at 800 °C for 50 h. Hu et al. [242] also observed SrO particle segregation on LSM

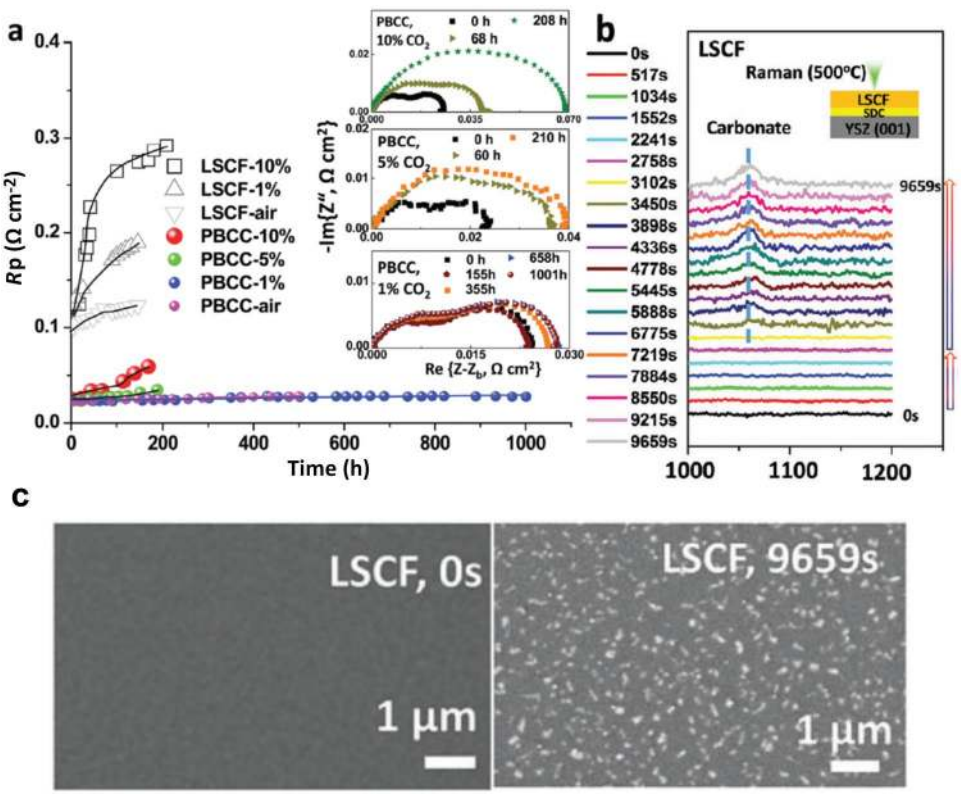

Fig. 16 **a** Durability of LSCF in air containing different amounts of CO_2 under OCV conditions, **b** in situ surface enhanced Raman spectroscopic study of LSCF films at 500 °C in atmospheres of pure O_2 or O_2 with 10% CO_2 and **c** SEM of fresh films and films after Raman testing in O_2 with 10% CO_2. Reproduced with permission from Ref. [39]. Copyright 2018, Royal Society of Chemistry

surfaces at annealing temperatures of 750–850 °C in 50% moisture. The results showed that an increased moisture, temperature and electric bias as well as decreased oxygen partial pressure can accelerate Sr surface segregation on LSM and as well as formation of $La_2Zr_2O_7$ and Mn_2O_3 phases at LSM/YSZ interfaces.

Moisture can also induce La_2O_3 segregation. For example, Kim et al. [243] observed La_2O_3 segregation on LSM surfaces annealed at 800 °C for 5 h in 20% and 40% humidified air that was different as compared with annealing in dry air. Liu et al. [197] also reported that exposure to 20% moisture at 800 °C for 200 h led to the partial decomposition of LSM into La_2O_3 and MnO_x. Here, these researchers reported that decomposition was severer at a reduced temperature of 700 °C and was possibly due to the preferential combination of La cations from LSM with steam to form La_2O_3, particularly at reduced temperatures.

Moisture can severely accelerate Sr surface segregation in LSC and LSCF. For example, Bucher et al. [195, 196] annealed LSC and LSCF pellet samples in humid atmosphere in a Si reactor and reported that after annealing at 600 °C for 5000 h with 30% and 75% relative humidity, LSC surface roughness increased by approximately one order of magnitude. Silicon poisoning and strong Sr segregation at depths of 10–90 nm were also found based on XPS depth profiles as compared with Sr segregation at a depth of 2 nm in dry conditions. Similarly, significant Sr segregation and silicon poisoning were also detected on LSCF after annealing at 600 and 700 °C in 30% humidity in which the reaction between volatile Si species and surface-segregated SrO may be the driving force for Sr surface accumulation. Liu et al. [197] also reported that after testing LSCF oxygen electrodes at 800 °C for 1000 h in 5% moisture the generation of a Sr-rich layer on the oxygen electrode surface was observed, and at a reduced temperature of 700 °C with 10% moisture, more Sr-rich oxides were detected.

5.3 Sr Segregation and Reaction at YSZ/GDC Interfaces

LSCF readily reacts with YSZ. Chen et al. [155] reported that the solid reaction of LSCF–YSZ mixtures starts at a calcining temperature of 800 °C to form a secondary phase of $SrZrO_3$. $SrZrO_3$ possesses an orthorhombic structure at room temperature [244] and is an electrical insulator with a poor ionic conductivity of 1.87×10^{-6} S cm^{-1} at 800 °C [245, 246], which is more than four orders of magnitude lower than 8.70×10^{-2} S cm^{-1} of GDC and 5.40×10^{-2} S cm^{-1} of YSZ [247]. In addition, the generated $SrZrO_3$ phase at the electrode/electrolyte interface can block ion migration [248] and the diffusion of Sr to YSZ surfaces can cause Sr depletion in LSCF, leading to the further formation of Sr-free La(Co,Fe)O_3 with significantly reduced electrocatalytic activities for ORR [249, 250]. Because of this, GDC or SDC barrier layers between LSCF and YSZ are essential for conventionally sintered LSCF electrodes at high temperatures of 1000–1200 °C to avoid chemical reactions at the LSCF/YSZ interface. Despite this, numerous reports have shown that even in the presence of doped ceria barrier layers, $SrZrO_3$ phases can still form at the YSZ interface after high-temperature electrode sintering [84, 100, 246, 249].

The diffusion of Sr across the GDC layer is mainly caused by the high reactivity of segregated Sr species. Thermodynamically, surface-segregated Sr species exist mainly in the form of $Sr(OH)_2$ in humid air that is volatile under SOFC operating conditions [251]. Because of this, volatile Sr species can easily diffuse across the pores or grain boundaries of GDC barrier layers through gas- or solid-phase diffusion to reach the YSZ surface and form $SrZrO_3$ [56, 252]. For example, Lu et al. [56] reported that after the sintering of a YSZ electrolyte close to an LSCF pellet without physical contact at 1200 °C for 50 h, $SrZrO_3$ was observed at the grain boundary of the YSZ electrolyte surface, indicating the volatility of surface-segregated Sr species. Yin et al. [251] also compared the SrO activity of SrO powder with LSCF powder through annealing at 1000 °C in air for 200 h in which a YSZ sheet was placed on top of the powders without direct contact during annealing. It was reported that after annealing with SrO powder, Sr deposition was observed on the YSZ surface, whereas after annealing with LSCF powder, no Sr deposition was observed on the YSZ surface, indicating the higher SrO activity of SrO powder as compared with LSCF powder at 1000 °C.

Lu et al. [56] further investigated the effects of sintering temperature on LSCF electrodes and observed the formation of a $SrZrO_3$ layer on the SDC/YSZ interface at sintering temperatures of 1150 °C and above. At a lower sintering temperature of 1050 °C, EDS analysis revealed the presence of significant amounts of Sr at the SDC/YSZ interface. On the other hand, Gao and Barnett [253] did not detect Sr diffusion to GDC/YSZ interfacial regions after sintering LSCF–GDC composite oxygen electrodes at 1100 °C for 2 h. This discrepancy may be due to variable surface chemistry of LSCF and the physical states of GDC barrier layers.

Because the pores of doped ceria barrier layers can facilitate the diffusion of volatile Sr, the adoption of a dense, pore-free doped ceria barrier layer is useful in blocking Sr diffusion [56, 254]. For example, Lu et al. [56] reported that in contrast to significant Sr diffusion to YSZ and porous SDC layer interfaces, the deposition of a dense SDC layer through PLD led to undetectable amounts of Srat YSZ electrolyte surfaces after sintering at 1200 °C for 2 h. The suppression of Sr diffusion led to the increase in PPD from 0.7 W cm^{-2} for the porous SDC barrier layer to 1.2 W cm^{-2}

for the densified SDC layer. Despite this, dense GDC barrier layers cannot completely eliminate Sr diffusion during extended sintering and under long-term operating conditions and segregated Sr diffusion can proceed through grain boundary or surface diffusion pathways in GDC layers [100, 254].

6 Strategies to Mitigate Surface Segregation

6.1 Composition Manipulation and Doping

One effective strategy to suppress Sr segregation and migration is to introduce A-site deficiencies in LSCF [56, 103]. For example, Lu et al. [56] reported that a 5% A-site-deficient LSCF oxygen electrode, $(La_{0.6}Sr_{0.4})_{0.95}Co_{0.2}Fe_{0.8}O_3$, can significantly reduce the formation of $SrZrO_3$ at the SDC/YSZ interface as compared with stoichiometric LSCF. Jung et al. [36] also reported that the degree of surface segregation in STF can be successfully controlled by intentionally preparing Sr deficient films. Celikbilek et al. [255] observed the formation of a well-dispersed, nanoscale B-site spinel phase ($CoFeO_x$) on the surface of an A-site-deficient $(La_{0.7}Sr_{0.3})_{0.95}(Co_{0.2}Fe_{0.8})O_{3-\delta}$ perovskite film electrode that led to enhanced electrochemical performances. Researchers have further reported that A-site nonstoichiometry can effectively reduce the reactivity between LSM electrodes and YSZ electrolytes [256, 257].

A-site or B-site doping is another effective strategy to suppress Sr segregation. Kim's group [38, 258] reported that Ca doping in the A-sites of double-perovskite structures to form $NdBa_{1-x}Ca_xCo_2O_{5+\delta}$ (NBCC) and $PrBa_{0.5}Sr_{0.5-x}Ca_xCo_2O_{5+\delta}$ (PBSCC) can significantly enhance the electrochemical performance and operating stability of electrodes under air and CO_2-containing atmospheres. Chen et al. [39] also demonstrated the excellent ORR activity and remarkable CO_2 tolerance of Ca-doped $PrBa_{0.8}Ca_{0.2}Co_2O_{5+\delta}$ (PBCC). When exposed to ~ 1 vol% CO_2 at 750 °C, the initial R_P of the PBCC electrode was 0.024 Ω cm^2 and slightly increased to 0.028 Ω cm^2 after operation for 1000 h, which is ~ 1/24 that of an LSCF oxygen electrode under the same conditions. Here, the enhanced stability was attributed to both the increased electron affinity of mobile oxygen species with Ca as determined through DFT calculations and the increased redox stability from coulometric titration [38]. Impedance spectroscopy and in situ surface-enhanced Raman spectroscopy analyses indicated that the surface of PBCC was much more active for oxygen exchange and more robust against CO_2 poisoning than that of LSCF as confirmed by DFT calculations [39].

B-site doping with high valence cations such as Nb [259–264], Sb [265, 266], Mo [267], Ta [268], Y [269–272], Sc [273] and W [274, 275] has also been shown to be effective in enhancing the structural and compositional stability of cobalt-containing perovskite oxygen electrode materials such as LSCF, BSCF, $SrCoO_{3-\delta}$ and $BaCoO_{3-\delta}$. For example, Li et al. [268] reported that Nb- and Ta-co-doped $SrCoO_{3-\delta}$ ($SrCo_{0.8}Nb_{0.1}Ta_{0.1}O_{3-\delta}$) significantly stabilized the perovskite structure, which led to enhanced ORR activities. Duan et al. [271, 276] also studied a Zr- and Y-co-doped $BaCo_{0.4}Fe_{0.4}Zr_{0.1}Y_{0.1}O_{3-\delta}$ (BCFZY) oxygen electrode for both ion- and proton-conducting SOFCs and reported that the application of BCFZY in GDC-based SOFCs enabled a peak power density of 0.97 W cm^{-2} at 500 °C and that the oxygen electrode showed excellent H_2O and CO_2 tolerances in air at 350 °C. Chen et al. [261] developed a novel Nb-doped $La_{0.24}Sr_{0.16}Ba_{0.6}Co_{0.5}Fe_{0.44}Nb_{0.06}O_{3-\delta}$ (LSBCFN) electrode through the novel direct mixing synthesis of LSCF and $Ba(Co_{0.7}Fe_{0.2}Nb_{0.1})O_{3-\delta}$ (BSCN). The new LSBCFN electrode showed high electrical conductivities (124 S cm^{-1} at 600 °C) and better electrochemical activities for ORR as compared with those of LSCF or BCFN in temperatures ranging from 600 to 900 °C. In addition, the surface of the prepared LSBCFN was clean after polarization in the presence of a Fe–Cr metallic interconnect in contrast to the significant deposition of Cr compounds observed on LSCF and BCFN electrode surfaces (Fig. 17). Here, Cr deposits on BCFN surfaces were mainly composed of Ba and Cr (Fig. 17d) and can be attributed to the formation of $BaCr_2O_4$ and/or $BaCrO_4$ [277]. The high resistance of LSBCFN electrodes to Cr deposition is due to the significantly reduced surface segregation of Sr and Ba (Fig. 17g).

One positive effect of high valence cation doping is the control of Co valences as the structural stability of Co-based perovskite oxides is mainly affected by the oxidation state of Coin perovskites [266, 273, 278]. Based on this, Wang et al. [264, 279] systematically studied the chemical stability of BSCF in a wide range of oxygen partial pressures from 1 to 10^{-22} bar from room temperature to 1000 °C and found that the cubic phase of BSCF decomposed if trivalent Co ions were oxidized to higher oxidation states in high oxygen partial pressures or if divalent Co ions were reduced to lower oxidation states in low oxygen partial pressures [279]. Usiskin et al. [278] also reported that both BSCF and $SrCo_{0.9}Nb_{0.1}O_{3-\delta}$ (SCN) can experience oxidative partial decomposition, which is thermodynamically preferred if the average valence of Co is greater than ~ 3.0. The doping of high valence cations can also effectively tune Co valences and therefore tailor the chemical stability of Co-based electrode materials. For example, Sc doping led to the absence of Co^{4+} in $SrSc_{0.2}Co_{0.8}O_{3-\delta}$ [273]. Wang et al. [264, 266] reported that the doping of high valence Nb or Sb into

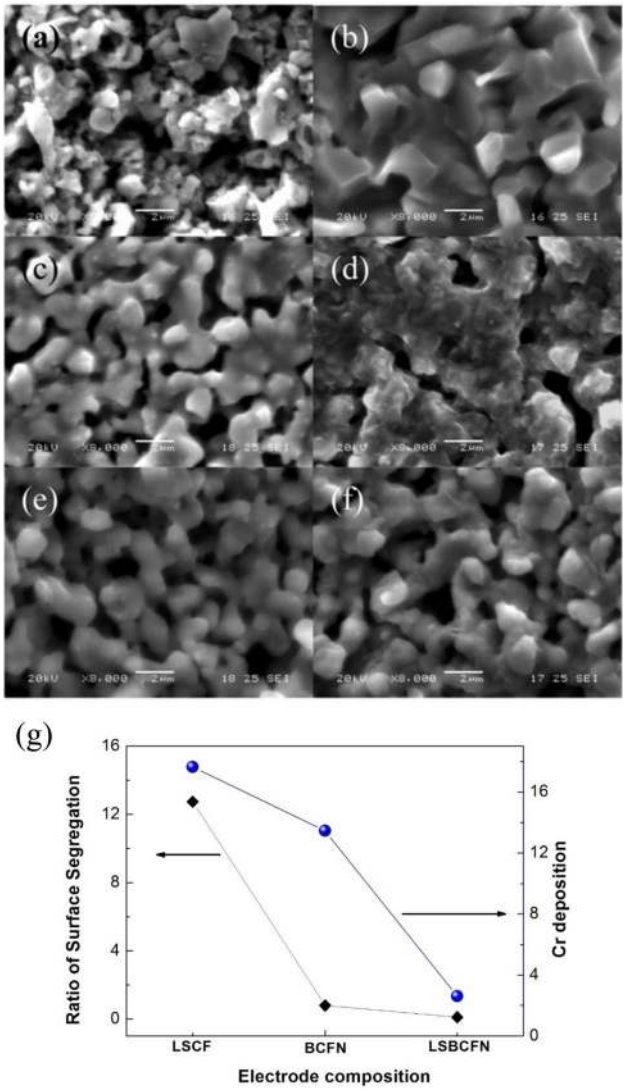

Fig. 17 SEM micrographs of LSCF, BCFN and LSBCFN electrode surfaces before and after testing at 900 °C under a current passage of 200 mA cm^{-2} in the presence of metallic interconnects: **a**, **b** LSCF, **c**, **d** BCFN and **e**, **f** LSBCFN. Plots of Cr deposition and ratios of surface segregation of Sr and Ba of LSCF, BCFN and LSBCFN electrodes are given in **g**. Reproduced with permission from Ref. [261]. Copyright 2013, Royal Society of Chemistry

B-sites lowered the average valence of Co and consequently improved the chemical stability of BSCF under high oxygen partial pressures.

However, there is a balance that exists between structural stability and electrocatalytic activity in the doping of high valence cations in perovskite oxygen electrode B-sites. For example, Fan et al. [280] reported that in the case of Nb-doped BSCF, Nb doping can enhance the structural stability of BSCF but at the expense of reduced oxygen permeation activity. The doping of 10% Nb in BSCFB-sites led to a 10% lowering in oxygen flux, whereas the doping of 20% Nb drastically increased performance losses to 65%. Similarly, Chen et al. [189] reported that Nb doping in LSCF B-sites significantly reduced SrO surface segregation and enhanced the stability of oxygen electrodes but also decreased electrode activity, whereas Pd doping promoted ORR activities due to the exsolution of catalytically active Pd/PdO nanoparticles under the influence of cathodic polarization. As a result, the synergistic effects of Nb and Pd co-doping can lead to increased electrocatalytic activities and operating stability for LSCF electrodes.

6.2 Surface Modification

The modification of cobaltite-based perovskite oxides with intentionally selected catalysts/materials has been extensively adopted to improve the electrocatalytic activity of oxygen electrodes [281–285]. In addition, these modifications can potentially suppress SrO surface segregation and enhance operating stability. For example, Choi et al. [17] developed a facile infiltration approach to modify LSCF electrodes with a dense and conformal LSM film coating in which the LSM film was epitaxially grown on LSCF grains after annealing at 800 °C due to their structural similarities. This approach took advantage of the fast ionic and electronic transport of the LSCF backbone and the facile surface kinetics of the LSM thin film, and as a result, the LSM film coating significantly enhanced the electrocatalytic activity and stability of LSCF during operations at 750 °C for 500 h (Fig. 18) [286]. It has also been reported that LSM infiltration can enhance the operational stability of BSCF in CO_2 [287].

In another study, Chen et al. [288] reported that the infiltration of multi-phase catalyst coatings composed of $BaCoO_{3-x}$ (BCO) and $PrCoO_{3-x}$ (PCO) nanoparticles and conformal PBCC thin films on LSCF led to much better performances with excellent durability as compared with bare LSCF cells within 250 h. The coating of BCO on LSCF can significantly suppress Sr surface segregation and enhance operating stability during exposure to Cr contamination [289].

Researchers have also reported that alkaline earth metal-free oxides such as LNO, $LaCoO_{3-\delta}$ (LC) and $PrNi_{0.5}Mn_{0.5}O_3$ (PNM) can act as effective surface protective layers and LNO coatings can not only enhance electrode electrocatalytic activities, but also increase the operational stability LSCF and $La_{0.8}Sr_{0.2}Co_{0.8}Ni_{0.2}O_{3-\delta}$ [290, 291]. In addition, PNM, LNO and LC coatings can enhance the tolerance of LSCF, BSCF and PBSCF to CO_2 and CrO_3 [189, 238, 292–294]. Moreover, Chen et al. [295] studied the effects of PrO_2, CeO_2 and $Pr_{0.2}Ce_{0.8}O_2$ (PDC) coatings on LSCF film surfaces and found that PrO_2 coatings can induce higher oxygen vacancy concentrations as compared with bare LSCF, greatly enhancing the rate of oxygen dissociation

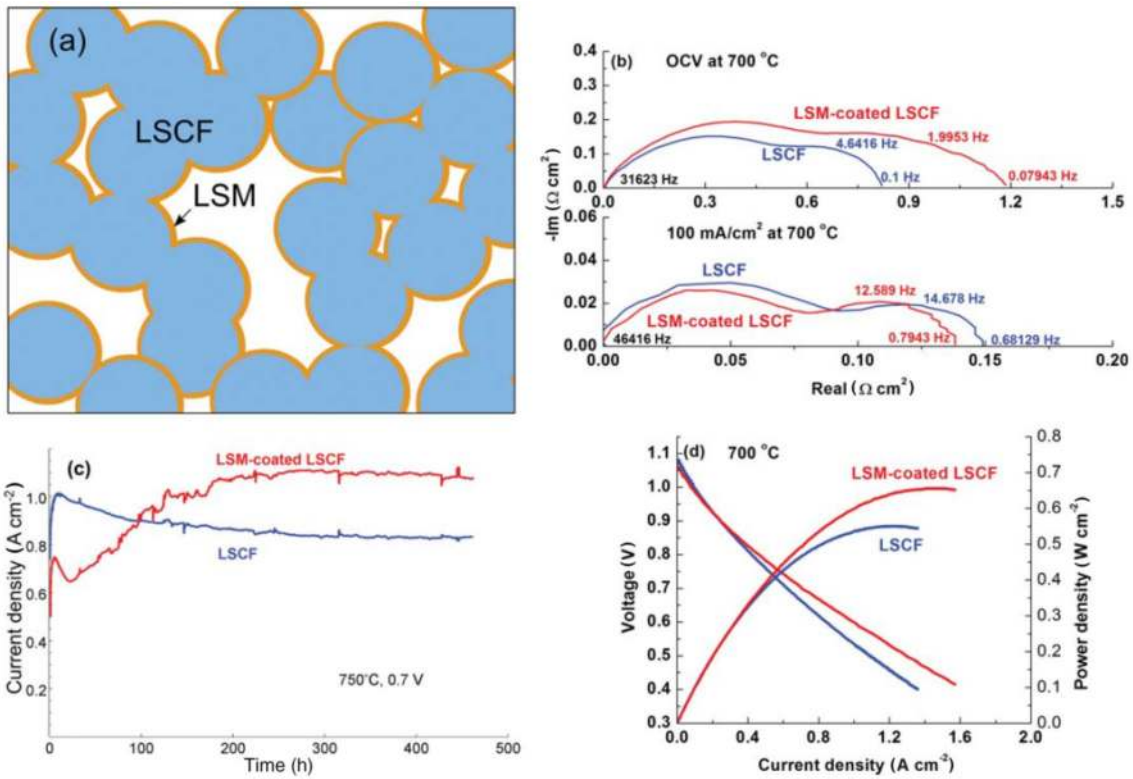

Fig. 18 **a** Schematic of an LSM-infiltrated LSCF oxygen electrode. **b** Impedance spectra of cells with and without the infiltration of LSM into LSCF electrodes. **c** Time-dependent current density plots of two cells under a constant voltage of 0.7 V. **d** *I–V* and *I–P* curves after long-term testing. Reproduced with permission from Ref. [286]. Copyright 2011, Royal Society of Chemistry

and ORR activity. In addition, PDC and CeO_2 coatings can suppress SrO surface segregation, thus enhancing durability. These results were also in good agreement with the positive effects of GDC nanoparticle decoration on the suppression of SrO surface segregation in LSCF and SSC electrodes [296–298]. Furthermore, Li et al. [290] reported that SDC infiltration can significantly enhance the CO_2 tolerance of $SrCo_{0.85}Ta_{0.15}O_3$ electrodes.

In another study, Gong et al. [299] investigated the effects of nanoscale ZrO_2 films on the cation stability of nanostructured LSC electrodes in which LSC was first infiltrated into an LSGM scaffold and coated with a conformal layer of the nanoscale ZrO_2 film through atomic layer deposition (ALD). And as a result of this ZrO_2 coating, reductions in R_P and degradation rates as compared with the pristine sample by factors of 19 and 18 during stability testing at 700 °C for 4000 h, respectively, were observed. Here, the improved ORR activity retention was attributed to the suppression of Sr enrichment through the exchange of $Zr_M\bullet$ for Co(III) and the creation of space charge layers across the oxygen electrode/ZrO_2 interface according to a defect chemistry model. Gong et al. [300] also used ZrO_2 coatings to enhance the cation stability of LSCF–GDC oxygen electrodes. Yildiz et al. [165] modified LSC film surfaces by infiltrating cations more and less reducible than Co into LSC B-sites and found that the infiltration of less reducible cations can significantly suppress Sr segregation and phase separation and reduce surface oxygen vacancy concentrations as well as increase LSC surface oxidation. Here, the reduction in surface oxygen vacancy concentrations led to decreased electrostatic interactions between oxygen vacancies and Sr cations, meaning that the infiltration of less reducible cations can significantly improve stability. These researchers further reported that the addition of Hf led to up to 30 times faster oxygen exchange kinetics after annealing at 530 °C for 54 h in air.

6.3 Phase Migration and In Situ Formation of Protective Layers

More recently, Ai et al. [301, 302] developed a decoration method to incorporate doped Bi_2O_3 materials such as $Er_{0.4}Bi_{1.6}O_3$ (ESB) into LSM and $Sm_{0.95}Co_{0.95}Pd_{0.05}O_{3-\delta}$ (SmCPd) to form composite electrodes without the high-temperature pre-sintering process and found that ESB-decorated composite electrodes provided significantly enhanced cathode performances for ORR in SOFCs. Further studies have shown that ESB decoration can substantially increase the power performance and stability

of Nb-doped $La_{0.6}Sr_{0.4}Co_{0.2}Fe_{0.7}Nb_{0.1}O_{3-\delta}$ (LSCFNb) electrodes directly assembled on barrier layer-free YSZ electrolyte cells, achieving a peak power density of 1.32 W cm^{-2} and excellent stability at 750 °C and 250 mA cm^{-2} for 100 h [303]. Here, these results indicate the redistribution and migration of the ESB phase in the ESB-LSCFNb composite towards the YSZ electrolyte under the influence of cathodic polarization and the formation of a thin ESB layer at the cathode/YSZ electrolyte interface (Fig. 19). And aside from individual and isolated Sr-rich areas/particles in the size range of 10–40 nm, La and other elements of LSCFNb were uniformly distributed, indicating the significant suppression of Sr segregation and diffusion in LSCFNb electrodes under polarization conditions by ESB decoration. The in situ formed ESB layer can not only prevent direct contact and subsequent reaction between segregated SrO and the YSZ electrolyte, but also significantly promote oxygen migration/diffusion at the interface for O_2 reduction reactions, resulting in remarkable increases in power output and decreases in activation energy. And overall, these results clearly demonstrate the benefits of the in situ formation of highly functional and active ESB protective layers on LSC-based cathode and YSZ electrolyte interfaces through ESB-decorated composite cathodes under SOFC operation conditions. Despite this, more work is required to optimize the polarization conditions for these phase migrations and distributions for the electrode/electrolyte interface of SOCs.

7 Concluding Remarks

Cation surface segregation, particularly Sr, is thermodynamically favourable under SOC operating conditions. Segregated Sr cations are uniformly dispersed on electrode surfaces and can gradually agglomerate to form Sr-rich secondary phases in the form of SrO, $SrCO_3$ or $Sr(OH)_2$. These Sr-rich secondary phases are electrochemically inert, and their occupation on active surface sites can drastically deteriorate ORR/OER electrocatalytic activity. The excess surface segregation of Sr can also lead to the deficiency of Sr cations at the A-site of perovskite oxides, resulting in the deterioration in the electronic as well as ionic conductivity properties of the oxygen electrodes. And the major driving forces of surface segregation include elastic and/or electrostatic interactions. However, under polarization conditions, oxygen nonstoichiometry, i.e. the oxygen vacancy formation and termination processes on the surface of the perovskite electrodes, induced by the cathodic and anodic polarization

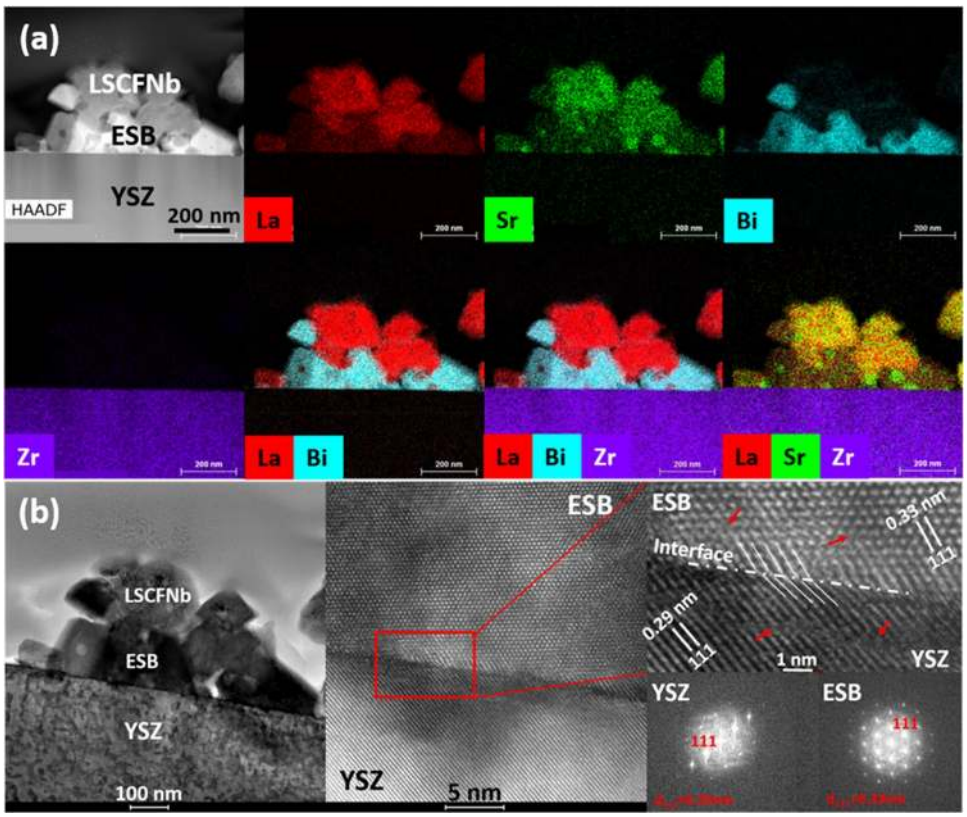

Fig. 19 **a** STEM-EDS element mapping and **b** HRTEM and FFT images of the ESB-LSCFNb/YSZ interface of an anode-supported YSZ electrolyte cell with a directly assembled ESB-LSCFNb electrode after polarization at 250 mA cm^{-2} and 750 °C for 100 h. Red arrows indicate lattice distortion. Reproduced with permission from Ref. [303]. Copyright 2018, American Chemical Society

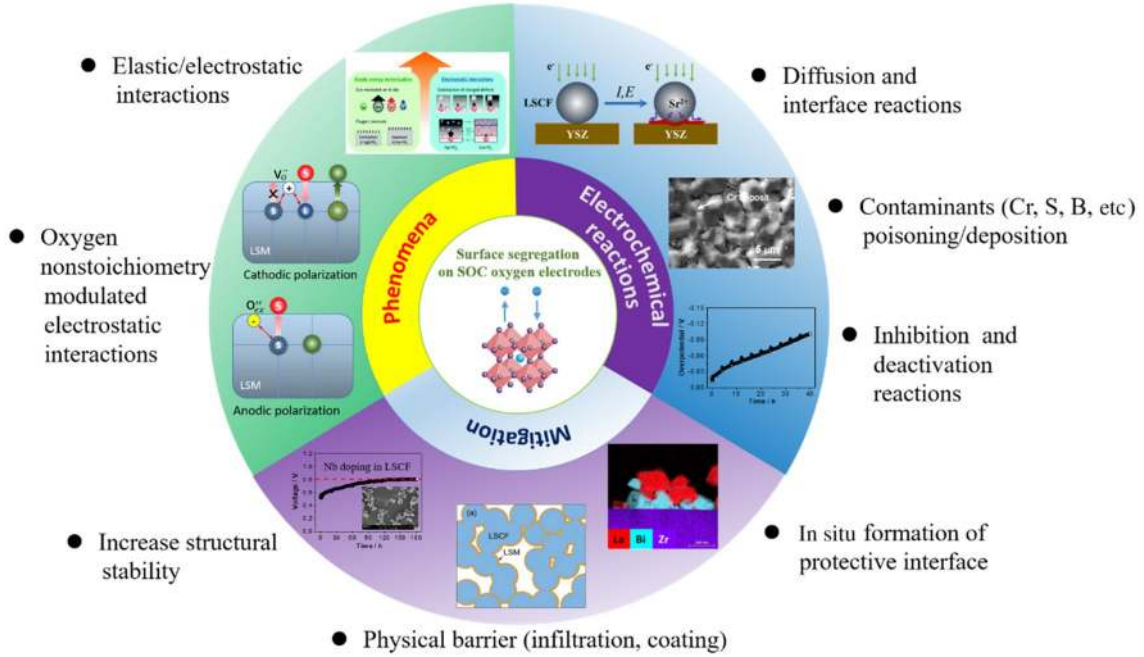

Fig. 20 Phenomena, electrochemical properties and mitigation strategies of cation surface segregation of SOC oxygen electrodes

could substantially modulate and change nature of the electrostatic interactions, accelerating or incorporating surface-segregated Sr species. The dominant role of oxygen vacancy generation/termination under polarization conditions is evidently illustrated by the opposite effects of polarization on Sr surface segregation and incorporation or inhibition on LSM and LSCF electrodes. Because of this, the role of polarization in surface segregation is particularly important for the fundamental understanding of the performance and stability of SOCs under cyclic polarization or reversible operating conditions.

Segregated cations, particularly Sr and Mn species, can further interact chemically with volatile impurities such as Cr, S and B in SOC stacks, leading to contaminant deposition and poisoning as well as significant performance degradation. Because of this, inhibition and significant reduction of surface cation segregation are critical in the enhancement of SOC electrochemical performance and durability. Here, the manipulation of operating regimes as well as the modification of stoichiometric compositions and oxygen electrode surfaces is effective approaches to mitigate the detrimental effects of surface segregation on operational stability. In addition, recent developments in the phase migration and in situ deposition and formation of highly active and protective layers on electrode/electrolyte interfaces have shown particular potential in the mitigation and inhibition of the detrimental effects of surface segregation in cobaltite-based electrodes of SOCs. Figure 20 summarizes the phenomena, electrochemical properties and mitigation strategies of cation surface segregation of SOC cathodes.

Overall, more insightful and fundamental knowledge concerning cation segregation, particularly in Sr-containing perovskite oxygen electrodes, is needed to foster the development of commercially viable SOC technologies. Here, key questions that need to be addressed include surface chemistry (e.g. segregation, diffusion, surface termination), and changes in surface chemistry with environment such as volatile species, microstructural features under static annealing conditions; oxygen nonstoichiometry and its associated surface chemistry under dynamic polarization conditions; cation segregation, distribution and phase changes at electrode surfaces and electrode/electrolyte interfaces; and the fundamental effects of segregation on electrochemical activity and long-term durability. And to address these interrelated and complex scientific questions, a combination of in situ and ex situ surface and microstructural characterization techniques such as synchrotron XAS, XPS, EELS, SIMS, high-temperature scanning probe microscopy and FIB-STEM as well as computational and thermodynamic modelling need to be applied to obtain model electrodes under well-controlled and defined test conditions to provide critical insights into the mechanisms of cation segregation that can further be used to predict the long-term activity and durability of SOC oxygen electrodes.

Acknowledgements This project was supported by the National Natural Science Foundation of China (21875038), the Natural Science

Foundation of Fujian Province, China (2018J01678), and the Australian Research Council under the Discovery Project Scheme (DP180100568 and DP180100731).

Open Access This article is licensed under a Creative Commons Attribution 4.0 International License, which permits use, sharing, adaptation, distribution and reproduction in any medium or format, as long as you give appropriate credit to the original author(s) and the source, provide a link to the Creative Commons licence, and indicate if changes were made. The images or other third party material in this article are included in the article's Creative Commons licence, unless indicated otherwise in a credit line to the material. If material is not included in the article's Creative Commons licence and your intended use is not permitted by statutory regulation or exceeds the permitted use, you will need to obtain permission directly from the copyright holder. To view a copy of this licence, visit http://creativecommons.org/licenses/by/4.0/.

References

1. Wachsman, E.D., Lee, K.T.: Lowering the temperature of solid oxide fuel cells. Science **334**, 935–939 (2011)
2. Gao, Z., Mogni, L.V., Miller, E.C., et al.: A perspective on low-temperature solid oxide fuel cells. Energy Environ. Sci. **9**, 1602–1644 (2016)
3. Zhang, Y., Knibbe, R., Sunarso, J., et al.: Recent progress on advanced materials for solid-oxide fuel cells operating below 500° C. Adv. Mater. **29**, 1700132 (2017)
4. Fan, L., Zhu, B., Su, P.C., et al.: Nanomaterials and technologies for low temperature solid oxide fuel cells: recent advances, challenges and opportunities. Nano Energy **45**, 148–176 (2018)
5. Mori, T., Wepf, R., Jiang, S.P.: Future prospects for the design of 'state-of-the-art' solid oxide fuel cells. J. Phys. Energy (2020). https://doi.org/10.1088/2515-7655/ab8f05
6. Jensen, S.H., Graves, C., Mogensen, M., et al.: Large-scale electricity storage utilizing reversible solid oxide cells combined with underground storage of CO_2 and CH_4. Energy Environ. Sci. **8**, 2471–2479 (2015)
7. Ebbesen, S.D., Jensen, S.H., Hauch, A., et al.: High temperature electrolysis in alkaline cells, solid proton conducting cells, and solid oxide cells. Chem. Rev. **114**, 10697–10734 (2014)
8. Zheng, Y., Wang, J., Yu, B., et al.: A review of high temperature co-electrolysis of H_2O and CO_2 to produce sustainable fuels using solid oxide electrolysis cells (SOECs): advanced materials and technology. Chem. Soc. Rev. **46**, 1427–1463 (2017)
9. Mogensen, M., Chen, M., Frandsen, H., et al.: Reversible solid-oxide cells for clean and sustainable energy. Clean Energy **3**, 175–201 (2019)
10. Song, Y., Zhang, X., Xie, K., et al.: High-temperature CO_2 electrolysis in solid oxide electrolysis cells: developments, challenges, and prospects. Adv. Mater. **31**, 1902033 (2019)
11. Yokokawa, H., Sakai, N., Horita, T., et al.: Electrolytes for solid-oxide fuel cells. MRS Bull. **30**, 591–595 (2005)
12. Fergus, J.W.: Electrolytes for solid oxide fuel cells. J. Power Sources **162**, 30–40 (2006)
13. Zhong, H., Matsumoto, H., Ishihara, T., et al.: Self-supported $LaGaO_3$-based honeycomb-type solid oxide fuel cell with high volumetric power density. Solid State Ion. **179**, 1474–1477 (2008)
14. Yang, L., Wang, S.Z., Blinn, K., et al.: Enhanced sulfur and coking tolerance of a mixed ion conductor for SOFCs: $BaZr_{0.1}Ce_{0.7}Y_{0.2-x}Yb_xO_{3-\delta}$. Science **326**, 126–129 (2009)
15. Fabbri, E., Bi, L., Pergolesi, D., et al.: Towards the next generation of solid oxide fuel cells operating below 600 °C with chemically stable proton-conducting electrolytes. Adv. Mater. **24**, 195–208 (2012)
16. Suzuki, T., Hasan, Z., Funahashi, Y., et al.: Impact of anode microstructure on solid oxide fuel cells. Science **325**, 852–855 (2009)
17. Choi, J.J., Qin, W.T., Liu, M.F., et al.: Preparation and characterization of $(La_{0.8}Sr_{0.2})_{0.95}MnO_{3-\delta}$ (LSM) thin films and LSM/LSCF interface for solid oxide fuel cells. J. Am. Ceram. Soc. **94**, 3340–3345 (2011)
18. Chen, Y., deGlee, B., Tang, Y., et al.: A robust fuel cell operated on nearly dry methane at 500 °C enabled by synergistic thermal catalysis and electrocatalysis. Nat. Energy **3**, 1042–1050 (2018)
19. Tao, S.W., Irvine, J.T.S.: A redox-stable efficient anode for solid-oxide fuel cells. Nat. Mater. **2**, 320–323 (2003)
20. Lu, J., Zhu, C., Pan, C., et al.: Highly efficient electrochemical reforming of CH_4/CO_2 in a solid oxide electrolyser. Sci. Adv. **4**, eaar5100 (2018)
21. Huang, Y.H., Dass, R.I., Xing, Z.L., et al.: Double perovskites as anode materials for solid-oxide fuel cells. Science **312**, 254–257 (2006)
22. Zhu, C., Hou, S., Hu, X., et al.: Electrochemical conversion of methane to ethylene in a solid oxide electrolyzer. Nat. Commun. **10**, 1173 (2019)
23. Liu, Q., Dong, X., Xiao, G., et al.: A novel electrode material for symmetrical SOFCs. Adv. Mater. **22**, 5478–5482 (2010)
24. Kim, S.H., Ohshima, T., Shiratori, Y., et al.: Effect of water vapor and SO*x* in air on the cathodes of solid oxide fuel cells. In: Fthenakis, V., Dillon, A., Savage, N. (eds.) Life-Cycle Analysis for New Energy Conversion and Storage Systems, pp. 131–137. Cambridge University Press, Cambridge (2008)
25. Ye, L., Zhang, M., Huang, P., et al.: Enhancing CO_2 electrolysis through synergistic control of non-stoichiometry and doping to tune cathode surface structures. Nat. Commun. **8**, 14785 (2017)
26. Sengodan, S., Choi, S., Jun, A., et al.: Layered oxygen-deficient double perovskite as an efficient and stable anode for direct hydrocarbon solid oxide fuel cells. Nat. Mater. **14**, 205–209 (2015)
27. Chen, K., Ai, N., Jiang, S.P.: Reasons for the high stability of nano-structured (La,Sr)MnO_3 infiltrated Y_2O_3–ZrO_2 composite oxygen electrodes of solid oxide electrolysis cells. Electrochem. Commun. **19**, 119–122 (2012)
28. Hughes, G.A., Yakal-Kremski, K., Barnett, S.A.: Life testing of LSM–YSZ composite electrodes under reversing-current operation. Phys. Chem. Chem. Phys. **15**, 17257–17262 (2013)
29. Chen, K., Liu, S.S., Ai, N., et al.: Why solid oxide cells can be reversibly operated in solid oxide electrolysis cell and fuel cell modes? Phys. Chem. Chem. Phys. **17**, 31308–31315 (2015)
30. Graves, C., Ebbesen, S.D., Jensen, S.H., et al.: Eliminating degradation in solid oxide electrochemical cells by reversible operation. Nat. Mater. **14**, 239–244 (2015)
31. Jiang, S.P.: Development of lanthanum strontium manganite perovskite cathode materials of solid oxide fuel cells: a review. J. Mater. Sci. **43**, 6799–6833 (2008)
32. Chen, Y., Bu, Y., Zhang, Y., et al.: A highly efficient and robust nanofiber cathode for solid oxide fuel cells. Adv. Energy Mater. **7**, 1601890 (2017)
33. Jiang, S.P.: Development of lanthanum strontium cobalt ferrite perovskite electrodes of solid oxide fuel cells—a review. Int. J. Hydrogen Energy **44**, 7448–7493 (2019)
34. Li, Y., Zhang, W., Wu, T., et al.: Segregation induced self-assembly of highly active perovskite for rapid oxygen reduction reaction. Adv. Energy Mater. **8**, 1801893 (2018)
35. Shao, Z.P., Haile, S.M.: A high-performance cathode for the next generation of solid-oxide fuel cells. Nature **431**, 170–173 (2004)

36. Jung, W., Tuller, H.L.: Investigation of surface Sr segregation in model thin film solid oxide fuel cell perovskite electrodes. Energy Environ. Sci. **5**, 5370–5378 (2012)
37. Zhang, S.L., Wang, H.Q., Lu, M.Y., et al.: Cobalt-substituted $SrTi_{0.3}Fe_{0.7}O_{3-\delta}$: a stable high-performance oxygen electrode material for intermediate-temperature solid oxideelectrochemical cells. Energy Environ. Sci. **11**, 1870–1879 (2018)
38. Yoo, S., Jun, A., Ju, Y.W., et al.: Development of double-perovskite compounds as cathode materials for low-temperature solid oxide fuel cells. Angew. Chem. Int. Ed. **53**, 13064–13067 (2014)
39. Chen, Y., Yoo, S., Choi, Y., et al.: A highly active, CO_2-tolerant electrode for the oxygen reduction reaction. Energy Environ. Sci. **11**, 2458–2466 (2018)
40. Vøllestad, E., Strandbakke, R., Tarach, M., et al.: Mixed proton and electron conducting double perovskite anodes for stable and efficient tubular proton ceramic electrolysers. Nat. Mater. **18**, 752–759 (2019)
41. Chen, Y., Téllez, H., Burriel, M., et al.: Segregated chemistry and structure on (001) and (100) surfaces of $(La_{1-x}Sr_x)_2CoO_4$ override the crystal anisotropy in oxygen exchange kinetics. Chem. Mater. **27**, 5436–5450 (2015)
42. Han, J.W., Yildiz, B.: Mechanism for enhanced oxygen reduction kinetics at the $(La,Sr)CoO_{3-\delta}/(La,Sr)_2CoO_{4+\delta}$ hetero-interface. Energy Environ. Sci. **5**, 8598–8607 (2012)
43. Wu, J., Pramana, S.S., Skinner, S.J., et al.: Why Ni is absent from the surface of $La_2NiO_{4+\delta}$? J. Mater. Chem. A **3**, 23760–23767 (2015)
44. Gu, X.K., Carneiro, J.S.A., Samira, S., et al.: Efficient oxygen electrocatalysis by nanostructured mixed-metal oxides. J. Am. Chem. Soc. **140**, 8128–8137 (2018)
45. Sohal, M., O'Brien, J., Stoots, C., et al.: Degradation issues in solid oxide cells during high temperature electrolysis. J. Fuel Cell Sci. Technol. **9**, 011017 (2012)
46. Moçoteguy, P., Brisse, A.: A review and comprehensive analysis of degradation mechanisms of solid oxide electrolysis cells. Int. J. Hydrogen Energy **38**, 15887–15902 (2013)
47. Chen, K., Jiang, S.P.: Review-materials degradation of solid oxide electrolysis cells. J. Electrochem. Soc. **163**, F3070–F3083 (2016)
48. Yokokawa, H., Yamaji, K., Brito, M.E., et al.: General considerations on degradation of solid oxide fuel cell anodes and cathodes due to impurities in gases. J. Power Sources **196**, 7070–7075 (2011)
49. Jiang, S.P., Chen, X.B.: Chromium deposition and poisoning of cathodes of solid oxide fuel cells—a review. Int. J. Hydrogen Energy **39**, 505–531 (2014)
50. Druce, J., Téllez, H., Hyodo, J.: Surface segregation and poisoning in materials for low-temperature SOFCs. MRS Bull. **39**, 810–815 (2014)
51. Li, Y., Zhang, W., Zheng, Y., et al.: Controlling cation segregation in perovskite-based electrodes for high electro-catalytic activity and durability. Chem. Soc. Rev. **46**, 6345–6378 (2017)
52. Koo, B., Kim, K., Kim, J.K., et al.: Sr segregation in perovskite oxides: why it happens and how it exists. Joule **2**, 1476–1499 (2018)
53. Jiang, S.P., Love, J.G.: Origin of the initial polarization behavior of Sr-doped $LaMnO_3$ for O-2 reduction in solid oxide fuel cells. Solid State Ion. **138**, 183–190 (2001)
54. Kim, D., Park, J.W., Yun, B.H., et al.: Correlation of time-dependent oxygen surface exchange kinetics with surface chemistry of $La_{0.6}Sr_{0.4}Co_{0.2}Fe_{0.8}O_{3-\delta}$ catalysts. ACS Appl. Mater. Interfaces **11**, 31786–31792 (2019)
55. Simner, S.P., Anderson, M.D., Engelhard, M.H., et al.: Degradation mechanisms of La–Sr–Co–Fe–O_3 SOFC cathodes. Electrochem. Solid State Lett. **9**, A478–A481 (2006)
56. Lu, Z., Darvish, S., Hardy, J., et al.: $SrZrO_3$ formation at the interlayer/electrolyte interface during $(La_{1-x}Sr_x)_{1-\delta}Co_{1-y}Fe_yO_3$ cathode sintering. J. Electrochem. Soc. **164**, F3097–F3103 (2017)
57. Sasaki, K., Haga, K., Yoshizumi, T., et al.: Chemical durability of solid oxide fuel cells: influence of impurities on long-term performance. J. Power Sources **196**, 9130–9140 (2011)
58. Schuler, J.A., Gehrig, C., Wuillemin, Z., et al.: Air side contamination in solid oxide fuel cell stack testing. J. Power Sources **196**, 7225–7231 (2011)
59. Irvine, J.T.S., Neagu, D., Verbraeken, M.C., et al.: Evolution of the electrochemical interface in high-temperature fuel cells and electrolysers. Nat. Energy **1**, 1–13 (2016)
60. Perry, N.H., Ishihara, T.: Roles of bulk and surface chemistry in the oxygen exchange kinetics and related properties of mixed conducting perovskite oxide electrodes. Materials **9**, 858 (2016)
61. Dulli, H., Dowben, P.A., Liou, S.H., et al.: Surface segregation and restructuring of colossal-magnetoresistant manganese perovskites $La_{0.65}Sr_{0.35}MnO_3$. Phys. Rev. B **62**, R14629–R14632 (2000)
62. de Jong, M.P., Dediu, V.A., Taliani, C., et al.: Electronic structure of $La_{0.7}Sr_{0.3}MnO_3$ thin films for hybrid organic/inorganic spintronics applications. J. Appl. Phys. **94**, 7292–7296 (2003)
63. Kumigashira, H., Horiba, K., Ohguchi, H., et al.: In situ photoemission characterization of terminating-layer-controlled $La_{0.6}Sr_{0.4}MnO_3$ thin films. Appl. Phys. Lett. **82**, 3430–3432 (2003)
64. Wu, Q.H., Liu, M., Jaegermann, W.: X-ray photoelectron spectroscopy of $La_{0.5}Sr_{0.5}MnO_3$. Mater. Lett. **59**, 1980–1983 (2005)
65. Caillol, N., Pijolat, M., Siebert, E.: Investigation of chemisorbed oxygen, surface segregation and effect of post-treatments on $La_{0.8}Sr_{0.2}MnO_3$ powder and screen-printed layers for solid oxide fuel cell cathodes. Appl. Surf. Sci. **253**, 4641–4648 (2007)
66. Huber, A.K., Falk, M., Rohnke, M., et al.: In situ study of activation and de-activation of LSM fuel cell cathodes—electrochemistry and surface analysis of thin-film electrodes. J. Catal. **294**, 79–88 (2012)
67. Backhaus-Ricoult, M., Adib, K., Clair, T.S., et al.: In-situ study of operating SOFC LSM/YSZ cathodes under polarization by photoelectron microscopy. Solid State Ion. **179**, 891–895 (2008)
68. Rohnke, M., Schaepe, K., Bachmann, A.K., et al.: In situ ToF-SIMS monitoring of SOFC cathodes—a case study of $La_{0.74}Sr_{0.17}Mn_{1.01}O_{2.9}$ model electrodes. Appl. Surf. Sci. **422**, 817–827 (2017)
69. Jiang, S.P., Zhang, S., Zhen, Y.D.: Early interaction between Fe–Cr alloy metallic interconnect and Sr-doped $LaMnO_3$ cathodes of solid oxide fuel cells. J. Mater. Res. **20**, 747–758 (2005)
70. Chen, M., Cheng, Y., He, S., et al.: Active, durable bismuth oxide-manganite composite oxygen electrodes: interface formation induced by cathodic polarization. J. Power Sources **397**, 16–24 (2018)
71. de Jong, M.P., Bergenti, I., Dediu, V.A., et al.: Evidence for Mn^{2+} ions at surfaces of $La_{0.7}Sr_{0.3}MnO_3$ thin films. Phys. Rev. B **71**, 014434 (2005)
72. Davis, J., Ludwig, K., Smith, K., et al.: Surface segregation in lanthanum strontium manganite thin films and its potential effect on the oxygen reduction reaction. J. Electrochem. Soc. **164**, F3091–F3096 (2017)
73. Wang, H.Q., Barnett, S.A.: Degradation mechanisms of porous $La_{0.6}Sr_{0.4}Co_{0.2}Fe_{0.8}O_{3-\delta}$ solid oxide fuel cell cathodes. J. Electrochem. Soc. **165**, F564–F570 (2018)
74. Orikasa, Y., Crumlin, E.J., Sako, S., et al.: Surface strontium segregation of solid oxide fuel cell cathodes proved by in situ

depth-resolved X-ray absorption spectroscopy. ECS Electrochem. Lett. **3**, F23–F26 (2014)
75. Ni, N., Cooper, S.J., Williams, R., et al.: Degradation of $(La_{0.6}Sr_{0.4})_{0.95}(Co_{0.2}Fe_{0.8})O_{3-\delta}$ solid oxide fuel cell cathodes at the nanometer scale and below. ACS Appl. Mater. Interfaces **8**, 17360–17370 (2016)
76. Niania, M.A., Podor, R., Britton, T.B., et al.: High temperature and in situ study of SrO surface precipitation on perovskite ceramics. Microsc. Microanal. **22**, 10–11 (2016)
77. Druce, J., Ishihara, T., Kilner, J.: Surface composition of perovskite-type materials studied by low energy ion scattering (LEIS). Solid State Ion. **262**, 893–896 (2014)
78. Druce, J., Tellez, H., Burriel, M., et al.: Surface termination and subsurface restructuring of perovskite-based solid oxide electrode materials. Energy Environ. Sci. **7**, 3593–3599 (2014)
79. Kubicek, M., Limbeck, A., Frömling, T., et al.: Relationship between cation segregation and the electrochemical oxygen reduction kinetics of $La_{0.6}Sr_{0.4}CoO_{3-\delta}$ thin film electrodes. J. Electrochem. Soc. **158**, B727–B734 (2011)
80. Cai, Z., Kubicek, M., Fleig, J., et al.: Chemical heterogeneities on $La_{06}Sr_{04}CoO_{3-\delta}$ thin films—correlations to cathode surface activity and stability. Chem. Mater. **24**, 1116–1127 (2012)
81. Rupp, G.M., Tellez, H., Druce, J., et al.: Surface chemistry of $La_{0.6}Sr_{0.4}CoO_{3-\delta}$ thin films and its impact on the oxygen surface exchange resistance. J. Mater. Chem. A **3**, 22759–22769 (2015)
82. Lu, M.Y., Railsback, J.G., Wang, H., et al.: Stable high current density operation of $La_{0.6}Sr_{0.4}Co_{0.2}Fe_{0.8}O_{3-\delta}$ oxygen electrodes. J. Mater. Chem. A **7**, 13531–13539 (2019)
83. Wang, H., Yakal-Kremski, K.J., Yeh, T., et al.: Mechanisms of performance degradation of $(La,Sr)(Co,Fe)O_{3-\delta}$ solid oxide fuel cell cathodes. J. Electrochem. Soc. **163**, F581–F585 (2016)
84. Hardy, J.S., Templeton, J.W., Edwards, D.J., et al.: Lattice expansion of LSCF-6428 cathodes measured by in situ XRD during SOFC operation. J. Power Sources **198**, 76–82 (2012)
85. Chang, K.C., Ingram, B., Ilavsky, J., et al.: Synchrotron X-ray studies of model SOFC cathodes, part I: thin film cathodes. Solid State Ion. **311**, 118–126 (2017)
86. Zhao, L., Drennan, J., Kong, C., et al.: Insight into surface segregation and chromium deposition on $La_{0.6}Sr_{0.4}Co_{0.2}Fe_{0.8}O_{3-\delta}$ cathodes of solid oxide fuel cells. J. Mater. Chem. A **2**, 11114–11123 (2014)
87. Zhao, L., Zhang, J., Becker, T., et al.: Raman spectroscopy study of chromium deposition on $La_{0.6}Sr_{0.4}Co_{0.2}Fe_{0.8}O_{3-\delta}$ cathode of solid oxide fuel cells. J. Electrochem. Soc. **161**, F687–F693 (2014)
88. Mutoro, E., Crumlin, E.J., Pöpke, H., et al.: Reversible compositional control of oxide surfaces by electrochemical potentials. J. Phys. Chem. Lett. **3**, 40–44 (2012)
89. Chang, K.C., Ingram, B., Hopper, M., et al.: Ultra small angle X-ray scattering studies of solid oxide fuel cell cathode powders. ECS Trans. **50**, 111–115 (2013)
90. Baumann, F.S., Fleig, J., Konuma, M., et al.: Strong performance improvement of $La_{0.6}Sr_{0.4}Co_{0.8}Fe_{0.2}O_{3-\delta}$ SOFC cathodes by electrochemical activation. J. Electrochem. Soc. **152**, A2074–A2079 (2005)
91. He, Z., Zhang, L., He, S., et al.: Cyclic polarization enhances the operating stability of $La_{0.57}Sr_{0.38}Co_{0.18}Fe_{0.72}Nb_{0.1}O_{3-\delta}$ oxygen electrode of reversible solid oxide cells. J. Power Sources **404**, 73–80 (2018)
92. Norman, C., Leach, C.: In situ high temperature X-ray photoelectron spectroscopy study of barium strontium iron cobalt oxide. J. Membr. Sci. **382**, 158–165 (2011)
93. Burriel, M., Wilkins, S., Hill, J.P., et al.: Absence of Ni on the outer surface of Sr doped La_2NiO_4 single crystals. Energy Environ. Sci. **7**, 311–316 (2014)
94. Ai, N., Li, N., Rickard, W.D., et al.: Highly stable Sr-free cobaltite-based perovskite cathodes directly assembled on a barrier-layer-free Y_2O_3–ZrO_2 electrolyte of solid oxide fuel cells. ChemSusChem **10**, 993–1003 (2017)
95. Téllez, H., Druce, J., Ju, Y.W., et al.: Surface chemistry evolution in $LnBaCo_2O_{5+\delta}$ double perovskites for oxygen electrodes. Int. J. Hydrogen Energy **39**, 20856–20863 (2014)
96. Tellez, H., Druce, J., Kilner, J.A., et al.: Relating surface chemistry and oxygen surface exchange in $LnBaCo_2O_{5+\delta}$ air electrodes. Faraday Discuss. **182**, 145–157 (2015)
97. Zhu, L., Wei, B., Wang, Z., et al.: Electrochemically driven deactivation and recovery in $PrBaCo_2O_{5+\delta}$ oxygen electrodes for reversible solid oxide fuel cells. ChemSusChem **9**, 2443–2450 (2016)
98. Decorse, P., Caboche, G., Dufour, L.C.: A comparative study of the surface and bulk properties of lanthanum–strontium–manganese oxides $La_{1-x}Sr_xMnO_{3\pm\delta}$ as a function of Sr-content, oxygen potential and temperature. Solid State Ion. **117**, 161–169 (1999)
99. Yu, Y., Ludwig, K.F., Woicik, J.C., et al.: Effect of Sr content and strain on Sr surface segregation of $La_{1-x}Sr_xCo_{0.2}Fe_{0.8}O_{3-\delta}$ as cathode material for solid oxide fuel cells. ACS Appl. Mater. Interfaces **8**, 26704–26711 (2016)
100. Wang, F., Nishi, M., Brito, M.E., et al.: Sr and Zr diffusion in LSCF/10GDC/8YSZ triplets for solid oxide fuel cells (SOFCs). J. Power Sources **258**, 281–289 (2014)
101. Yokokawa, H., Sakai, N., Horita, T., et al.: Thermodynamic and kinetic considerations on degradations in solid oxide fuel cell cathodes. J. Alloys Compd. **452**, 41–47 (2008)
102. Chen, Y., Jung, W., Cai, Z., et al.: Impact of Sr segregation on the electronic structure and oxygen reduction activity of $SrTi_{1-x}Fe_xO_3$ surfaces. Energy Environ. Sci. **5**, 7979–7988 (2012)
103. Ding, H., Virkar, A.V., Liu, M., et al.: Suppression of Sr surface segregation in $La_{1-x}Sr_xCo_{1-y}Fe_yO_{3-\delta}$: a first principles study. Phys. Chem. Chem. Phys. **15**, 489–496 (2013)
104. Kwon, H., Lee, W., Han, J.W.: Suppressing cation segregation on lanthanum-based perovskite oxides to enhance the stability of solid oxide fuel cell cathodes. RSC Adv. **6**, 69782–69789 (2016)
105. Lussier, A., Dvorak, J., Stadler, S., et al.: Stress relaxation of $La_{1/2}Sr_{1/2}MnO_3$ and $La_{2/3}Ca_{1/3}MnO_3$ at solid oxide fuel cell interfaces. Thin Solid Films **516**, 880–884 (2008)
106. Estrade, S., Arbiol, J., Peiro, F., et al.: Cationic and charge segregation in $La_{2/3}Ca_{1/3}MnO_3$ thin films grown on (001) and (110) $SrTiO_3$. Appl. Phys. Lett. **93**, 112505 (2008)
107. Estrade, S., Rebled, J.M., Arbiol, J., et al.: Effects of thickness on the cation segregation in epitaxial (001) and (110) $La_{2/3}Ca_{1/3}MnO_3$ thin films. Appl. Phys. Lett. **95**, 072507 (2009)
108. Jalili, H., Han, J.W., Kuru, Y., et al.: New insights into the strain coupling to surface chemistry, electronic structure, and reactivity of $La_{0.7}Sr_{0.3}MnO_3$. J. Phys. Chem. Lett. **2**, 801–807 (2011)
109. Kim, S.J., Akbay, T., Matsuda, J., et al.: Strain effects on oxygen reduction activity of Pr_2NiO_4 caused by gold bulk dispersion for low temperature solid oxide fuel cells. ACS Appl. Energy Mater. **2**, 1210–1220 (2019)
110. Kousi, K., Neagu, D., Bekris, L., et al.: Endogenous nanoparticles strain perovskite host lattice providing oxygen capacity and driving oxygen exchange and CH_4 conversion to syngas. Angew. Chem. Int. Ed. **59**, 2510–2519 (2020)
111. Cai, Z., Kuru, Y., Han, J.W., et al.: Surface electronic structure transitions at high temperature on perovskite oxides: the case of strained $La_{0.8}Sr_{0.2}CoO_3$ thin films. J. Am. Chem. Soc. **133**, 17696–17704 (2011)
112. Liu, X., Zhang, L., Zheng, Y., et al.: Uncovering the effect of lattice strain and oxygen deficiency on electrocatalytic activity of perovskite cobaltite thin films. Adv. Sci. **6**, 1801898 (2019)

113. Oh, D., Gostovic, D., Wachsman, E.D.: Mechanism of $La_{0.6}Sr_{0.4}Co_{0.2}Fe_{0.8}O_3$ cathode degradation. J. Mater. Res. **27**, 1992–1999 (2012)
114. Katsiev, K., Yildiz, B., Balasubramaniam, K., et al.: Electron tunneling characteristics on $La_{0.7}Sr_{0.3}MnO_3$ thin-film surfaces at high temperature. Appl.Phys. Lett. **95**, 092106 (2009)
115. Niania, M., Podor, R., Britton, B., et al.: High temperature and in situ study of SrO surface precipitation on perovskite ceramics. In: European Microscopy Congress 2016: Proceedings, pp. 834–835. Wiley Online Library (2016)
116. Lee, W., Han, J.W., Chen, Y., et al.: Cation size mismatch and charge interactions drive dopant segregation at the surfaces of manganite perovskites. J. Am. Chem. Soc. **135**, 7909–7925 (2013)
117. Chang, K.C., Ingram, B., Kavaipatti, B., et al.: In situ synchrotron X-ray studies of dense thin-film strontium-doped lanthanum manganite solid oxide fuel cell cathodes. Paper presented at the Symposium on Solid-State Ionics held at the 2008 MRS Fall Meeting, Boston, 1–5 Dec (2008)
118. Fister, M.: In situ characterization of strontium surface segregation in epitaxial $La_{0.7}Sr_{0.3}MnO_3$ thin films as a function of oxygen partial pressure. Appl. Phys. Lett. **93**, 151904 (2008)
119. Rohnke, M., Falk, M., Huber, A.K., et al.: Combining high temperature electrochemistry and time of flight secondary ion mass spectrometry: quasi in situ study of lanthanum strontium chromate manganate electrodes. J. Power Sources **221**, 97–107 (2013)
120. Plonczak, P., Bieberle-Hutter, A., Sogaard, M., et al.: Tailoring of $La_xSr_{1-x}Co_yFe_{1-y}O_{3-\delta}$ nanostructure by pulsed laser deposition. Adv. Funct. Mater. **21**, 2764–2775 (2011)
121. la O', G.J., Ahn, S.J., Crumlin, E., et al.: Catalytic activity enhancement for oxygen reduction on epitaxial perovskite thin films for solid-oxide fuel cells. Angew. Chem. Int. Ed. **49**, 5344–5347 (2010)
122. Deacon-Smith, D.E.E., Scanlon, D.O., Catlow, C.R.A., et al.: Interlayer cation exchange stabilizes polar perovskite surfaces. Adv. Mater. **26**, 7252–7256 (2014)
123. Lee, J.H., Luo, G., Tung, I.C., et al.: Dynamic layer rearrangement during growth of layered oxide films by molecular beam epitaxy. Nat. Mater. **13**, 879–883 (2014)
124. Develos-Bagarinao, K., De Vero, J., Kishimoto, H., et al.: Oxygen surface exchange properties and surface segregation behavior of nanostructured $La_{0.6}Sr_{0.4}Co_{0.2}Fe_{0.8}O_{3-\delta}$ thin film cathodes. Phys. Chem. Chem. Phys. **21**, 7183–7195 (2019)
125. Crumlin, E.J., Mutoro, E., Liu, Z., et al.: Surface strontium enrichment on highly active perovskites for oxygen electrocatalysis in solid oxide fuel cells. Energy Environ. Sci. **5**, 6081–6088 (2012)
126. Wang, W., Jiang, S.P.: Effect of polarization on the electrode behavior and microstructure of $(La,Sr)MnO_3$ electrodes of solid oxide fuel cells. J. Solid State Electrochem. **8**, 914–922 (2004)
127. Haider, M.A., McIntosh, S.: Evidence for two activation mechanisms in LSM SOFC cathodes. J. Electrochem. Soc. **156**, B1369–B1375 (2009)
128. Wang, W., Jiang, S.P.: A mechanistic study on the activation process of $(La,Sr)MnO_3$ electrodes of solid oxide fuel cells. Solid State Ion. **177**, 1361–1369 (2006)
129. Lee, H.Y., Cho, W.S., Oh, S.M., et al.: Active reaction sites for oxygen reduction in $La_{0.9}Sr_{0.1}MnO_3$/YSZ electrodes. J. Electrochem. Soc. **142**, 2659–2664 (1995)
130. Poulsen, F.W.: Defect chemistry modelling of oxygen-stoichiometry, vacancy concentrations, and conductivity of $(La_{1-x}Sr_x)_yMnO_{3\pm\delta}$. Solid State Ion. **129**, 145–162 (2000)
131. Shannon, R.D.: Revided effective ionic-radii and systematic studies of interatomic distances in halides and chalcogenides. Acta Crystallogr. Sect. A **32**, 751–767 (1976)
132. Jiang, S.P., Zhang, J.P., Apateanu, L., et al.: Deposition of chromium species at Sr-doped $LaMnO_3$ electrodes in solid oxide fuel cells I. Mechanism and kinetics. J. Electrochem. Soc. **147**, 4013–4022 (2000)
133. Paulson, S.C., Birss, V.I.: Chromium poisoning of LSM-YSZ SOFC cathodes—I. Detailed study of the distribution of chromium species at a porous, single-phase cathode. J. Electrochem. Soc. **151**, A1961–A1968 (2004)
134. Mizusaki, J., Mori, N., Takai, H., et al.: Oxygen nonstoichiometry and defect equilibrium in the perovskite-type oxides $La_{1-x}Sr_xMnO_{3+d}$. Solid State Ion. **129**, 163–177 (2000)
135. Huber, A.K., Falk, M., Rohnke, M., et al.: In situ study of electrochemical activation and surface segregation of the SOFC electrode material $La_{0.75}Sr_{0.25}Cr_{0.5}Mn_{0.5}O_{3\pm\delta}$. Phys. Chem. Chem. Phys. **14**, 751–758 (2012)
136. Chen, K., Hyodo, J., Dodd, A., et al.: Chromium deposition and poisoning of $La_{0.8}Sr_{0.2}MnO_3$ oxygen electrodes of solid oxide electrolysis cells. Faraday Discuss. **182**, 457–476 (2015)
137. Vovk, G., Chen, X., Mims, C.A.: In situ XPS studies of perovskite oxide surfaces under electrochemical polarization. J. Phys. Chem. B **109**, 2445–2454 (2004)
138. Choi, S.M., Ahn, J., Son, J.W., et al.: Comprehensive understanding of cathodic and anodic polarization effects on stability of nanoscale oxygen electrode for reversible solid oxide cells. ACS Appl. Mater. Interfaces **10**, 39608–39614 (2018)
139. Kivi, I., Aruväli, J., Kirsimäe, K., et al.: Oxygen stoichiometry in $La_{0.6}Sr_{0.4}CoO_{3-\delta}$ and $La_{0.6}Sr_{0.4}Co_{0.2}Fe_{0.8}O_{3-\delta}$ cathodes under applied potential as a function of temperature and oxygen partial pressure, measured by electrochemical in situ high-temperature XRD method. J. Electrochem. Soc. **160**, F1022–F1026 (2013)
140. Kivi, I., Aruväli, J., Kirsimäe, K., et al.: Kinetic response of $La_{0.6}Sr_{0.4}CoO_{3-\delta}$ lattice parameters to electric potential change in porous cathode at in situ solid oxide fuel cell conditions. J. Electrochem. Soc. **162**, F354–F358 (2015)
141. Matsui, T., Komoto, M., Muroyama, H., et al.: Degradation factors in $(La,Sr)(Co,Fe)O_{3-\delta}$ cathode/Sm_2O_3–CeO_2 interlayer/Y_2O_3–ZrO_2 electrolyte system during operation of solid oxide fuel cells. J. Power Sources **312**, 80–85 (2016)
142. Khan, M.Z., Mehran, M.T., Song, R.H., et al.: Effects of applied current density and thermal cycling on the degradation of a solid oxide fuel cell cathode. Int. J. Hydrogen Energy **43**, 12346–12357 (2018)
143. Khan, M.Z., Song, R.H., Hussain, A., et al.: Effect of applied current density on the degradation behavior of anode-supported flat-tubular solid oxide fuel cells. J. Eur. Ceram. Soc. **40**, 1407–1417 (2020)
144. Chen, K.F., Li, N., Ai, N., et al.: Direct application of cobaltite-based perovskite cathodes on the yttria-stabilized zirconia electrolyte for intermediate temperature solid oxide fuel cells. J. Mater. Chem. A **4**, 17678–17685 (2016)
145. Li, M., Chen, K.F., Hua, B., et al.: Smart utilization of cobaltite-based double perovskite cathodes on barrier-layer-free zirconia electrolyte of solid oxide fuel cells. J. Mater. Chem. A **4**, 19019–19025 (2016)
146. He, S., Saunders, M., Chen, K., et al.: A FIB-STEM study of strontium segregation and interface formation of directly assembled $La_{0.6}Sr_{0.4}Co_{0.2}Fe_{0.8}O_{3-\delta}$ cathode on Y_2O_3–ZrO_2 electrolyte of solid oxide fuel cells. J. Electrochem. Soc. **165**, F417–F429 (2018)
147. Jiang, S.P.: Thermally and electrochemically induced electrode/electrolyte interfaces in solid oxide fuel cells: an AFM and EIS study. J. Electrochem. Soc. **162**, F1119–F1128 (2015)
148. He, S., Chen, K.F., Saunders, M., et al.: Interface formation and Mn segregation of directly assembled $La_{0.8}Sr_{0.2}MnO_3$ cathode on Y_2O_3–ZrO_2 and Gd_2O_3–CeO_2 electrolytes of solid oxide fuel cells. Solid State Ion. **325**, 176–188 (2018)

149. The, D., Grieshammer, S., Schroeder, M., et al.: Microstructural comparison of solid oxide electrolyser cells operated for 6100 h and 9000 h. J. Power Sources **275**, 901–911 (2015)
150. Schefold, J., Brisse, A., Tietz, F.: Nine thousand hours of operation of a solid oxide cell in steam electrolysis mode. J. Electrochem. Soc. **159**, A137–A144 (2012)
151. Tietz, F., Sebold, D., Brisse, A., et al.: Degradation phenomena in a solid oxide electrolysis cell after 9000 h of operation. J. Power Sources **223**, 129–135 (2013)
152. Shimura, K., Nishino, H., Kakinuma, K., et al.: High durability of $La_{0.6}Sr_{0.4}Co_{0.2}Fe_{0.8}O_{3-\delta}$/samaria-doped ceria (SDC) composite oxygen electrode with SDC interlayer for reversible solid oxide fuel cell/solid oxide electrolysis cell. J. Ceram. Soc. Jpn. **125**, 218–222 (2017)
153. Finsterbusch, M., Lussier, A., Schaefer, J.A., et al.: Electrochemically driven cation segregation in the mixed conductor $La_{0.6}Sr_{0.4}Co_{0.2}Fe_{0.8}O_{3-\delta}$. Solid State Ion. **212**, 77–80 (2012)
154. Laurencin, J., Hubert, M., Sanchez, D.F., et al.: Degradation mechanism of $La_{0.6}Sr_{0.4}Co_{0.2}Fe_{0.8}O_{3-\delta}$/$Gd_{0.1}Ce_{0.9}O_{2-\delta}$ composite electrode operated under solid oxide electrolysis and fuel cell conditions. Electrochim. Acta **241**, 459–476 (2017)
155. Chen, K., Li, N., Ai, N., et al.: Polarization-induced interface and Sr segregation of in situ assembled $La_{0.6}Sr_{0.4}Co_{0.2}Fe_{0.8}O_{3-\delta}$ electrodes on Y_2O_3–ZrO_2 electrolyte of solid oxide fuel cells. ACS Appl. Mater. Interfaces **8**, 31729–31737 (2016)
156. Ai, N., He, S., Li, N., et al.: Suppressed Sr segregation and performance of directly assembled $La_{0.6}Sr_{0.4}Co_{0.2}Fe_{0.8}O_{3-\delta}$ oxygen electrode on Y_2O_3–ZrO_2 electrolyte of solid oxide electrolysis cells. J. Power Sources **384**, 125–135 (2018)
157. Pan, Z., Liu, Q., Zhang, L., et al.: Effect of Sr surface segregation of $La_{0.6}Sr_{0.4}Co_{0.2}Fe_{0.8}O_{3-\delta}$ electrode on its electrochemical performance in SOC. J. Electrochem. Soc. **162**, F1316–F1323 (2015)
158. Pan, Z., Liu, Q., Zhang, L., et al.: Study of activation effect of anodic current on $La_{0.6}Sr_{0.4}Co_{0.2}Fe_{0.8}O_{3-\delta}$ air electrode in solid oxide electrolyzer cell. Electrochim. Acta **209**, 56–64 (2016)
159. Railsback, J.G., Wang, H., Liu, Q., et al.: Degradation of $La_{0.6}Sr_{0.4}Fe_{0.8}Co_{0.2}O_{3-\delta}$ oxygen electrodes on $Ce_{0.9}Gd_{0.1}O_{2-\delta}$ electrolytes during reversing current operation. J. Electrochem. Soc. **164**, F3083–F3090 (2017)
160. Harrison, W.A.: Origin of Sr segregation at $La_{1-x}Sr_xMnO_3$ surfaces. Phys. Rev. B **83**, 155437 (2011)
161. Sharma, V., Mahapatra, M.K., Singh, P., et al.: Cationic surface segregation in doped $LaMnO_3$. J. Mater. Sci. **50**, 3051–3056 (2015)
162. Hashimoto, S.I., Fukuda, Y., Kuhn, M., et al.: Oxygen nonstoichiometry and thermo-chemical stability of $La_{0.6}Sr_{0.4}Co_{1-y}Fe_yO_{3-\delta}$ ($y=0.2$, 0.4, 0.6, 0.8). Solid State Ion. **181**, 1713–1719 (2010)
163. Hashimoto, S., Fukuda, Y., Kuhn, M., et al.: Thermal and chemical lattice expansibility of $La_{0.6}Sr_{0.4}Co_{1-y}Fe_yO_{3-\delta}$ ($y=0$, 0.2, 0.4, 0.6 and 0.8). Solid State Ion. **186**, 37–43 (2011)
164. Kuyyalil, J., Newby, D., Laverock, J., et al.: Vacancy assisted SrO formation on $La_{0.8}Sr_{0.2}Co_{0.2}Fe_{0.8}O_{3-\delta}$ surfaces—a synchrotron photoemission study. Surf. Sci. **642**, 33–38 (2015)
165. Tsvetkov, N., Lu, Q., Sun, L., et al.: Improved chemical and electrochemical stability of perovskite oxides with less reducible cations at the surface. Nat. Mater. **15**, 1010–1016 (2016)
166. Chang, K.C., Ingram, B., Kavaipatti, B., et al.: In situ synchrotron X-ray studies of dense thin-film strontium-doped lanthanum manganite solid oxide fuel cell cathodes. MRS Online Proc. Library, **1126** (2008)
167. De Souza, R.A., Kilner, J.A., Walker, J.F.: A SIMS study of oxygen tracer diffusion and surface exchange in $La_{0.8}Sr_{0.2}MnO_{3+\delta}$. Mater. Lett. **43**, 43–52 (2000)
168. Pavone, M., Munoz-Garcia, A.B., Ritzmann, A.M., et al.: First-principles study of lanthanum strontium manganite: insights into electronic structure and oxygen vacancy formation. J. Phys. Chem. C **118**, 13346–13356 (2014)
169. Mizusaki, J., Yonemura, Y., Kamata, H., et al.: Electronic conductivity, Seebeck coefficient, defect and electronic structure of nonstoichiometric $La_{1-x}Sr_xMnO_3$. Solid State Ion. **132**, 167–180 (2000)
170. Adler, S.B.: Factors governing oxygen reduction in solid oxide fuel cell cathodes. Chem. Rev. **104**, 4791–4843 (2004)
171. De Souza, R.A., Kilner, J.A.: Oxygen transport in $La_{1-x}Sr_xMn_{1-y}Co_yO_{3\pm\delta}$ perovskites. Part I. Oxygen tracer diffusion. Solid State Ion. **106**, 175–187 (1998)
172. De Souza, R.A., Kilner, J.A.: Oxygen transport in $La_{1-x}Sr_xMn_{1-y}Co_yO_{3\pm\delta}$ perovskites part II. Oxygen surface exchange. Solid State Ion. **126**, 153–161 (1999)
173. Jiang, S.P.: Activation, microstructure, and polarization of solid oxide fuel cell cathodes. J. Solid State Electrochem. **11**, 93–102 (2007)
174. la O', G.J., Savinell, R.F., Shao-Horn, Y.: Activity enhancement of dense strontium-doped lanthanum manganite thin films under cathodic polarization: a combined AES and XPS study. J. Electrochem. Soc. **156**, B771–B781 (2009)
175. Budiman, R.A., Bagarinao, K.D., Ishiyama, T., et al.: Influence of Sr and Co deficiency on the transport properties and oxygen reduction reaction of $La_{0.6}Sr_{0.4}Co_{0.2}Fe_{0.8}O_{3-\delta}$. Solid State Ion. **348**, 115285 (2020)
176. Rupp, G.M., Opitz, A.K., Nenning, A., et al.: Real-time impedance monitoring of oxygen reduction during surface modification of thin film cathodes. Nat. Mater. **16**, 640 (2017)
177. Choi, Y., Lin, M.C., Liu, M.: Computational study on the catalytic mechanism of oxygen reduction on $La_{0.5}Sr_{0.5}MnO_3$ in solid oxide fuel cells. Angew. Chem. Int. Ed. **46**, 7214–7219 (2007)
178. Mutoro, E., Crumlin, E.J., Biegalski, M.D., et al.: Enhanced oxygen reduction activity on surface-decorated perovskite thin films for solid oxide fuel cells. Energy Environ. Sci. **4**, 3689–3696 (2011)
179. Hong, T., Zhao, M., Brinkman, K., et al.: Enhanced oxygen reduction activity on Ruddlesden–Popper phase decorated $La_{0.8}Sr_{0.2}FeO_{3-\delta}$ 3D heterostructured cathode for solid oxide fuel cells. ACS Appl. Mater. Interfaces **9**, 8659–8668 (2017)
180. Hong, T., Chen, F., Xia, C.: Barium carbonate nanoparticle to enhance oxygen reduction activity of strontium doped lanthanum ferrite for solid oxide fuel cell. J. Power Sources **278**, 741–750 (2015)
181. Hong, T., Chen, F., Xia, C.: Barium carbonate nanoparticle as high temperature oxygen reduction catalyst for solid oxide fuel cell. Electrochem. Commun. **51**, 93–97 (2015)
182. Xia, C., Hong, T., Brinkman, K.: Barium carbonate nanoparticles as synergistic catalysts for the oxygen reduction reaction on $La_{0.6}Sr_{0.4}Co_{0.2}Fe_{0.8}O_{3-\delta}$ solid oxide fuel cell cathodes. ChemElectroChem **3**, 805–813 (2016)
183. Traulsen, M.L., McIntyre, M.D., Norrman, K., et al.: Reversible decomposition of secondary phases in BaO infiltrated LSM electrodes—polarization effects. Adv. Mater. Interfaces **3**, 1600750 (2016)
184. Chen, Y., Yoo, S., Zhang, W., et al.: Effective promotion of oxygen reduction reaction by in situ formation of nanostructured catalyst. ACS Catal. **9**, 7137–7142 (2019)
185. Ai, N., Chen, K.F., Jiang, S.P.: A fundamental study of infiltrated CeO_2 and $(Gd,Ce)O_2$ nanoparticles on the electrocatalytic activity of Pt cathodes of solid oxide fuel cells. Solid State Ion. **233**, 87–94 (2013)
186. Ai, N., Chen, K.F., Jiang, S.P.: Role of electrocatalytic properties of infiltrated nanoparticles in the activity of cathodes of solid oxide fuel cells A case study of infiltrated $La_{0.8}Sr_{0.2}Co_xMn_{1-x}O_3$

($x = 0$, 0.5, and 1) on Pt electrode. Int. J. Hydrogen Energy **42**, 28807–28815 (2017)
187. Wachsman, E.D., Oh, D., Armstrong, E., et al.: Mechanistic understanding of Cr poisoning on $La_{0.6}Sr_{0.4}Co_{0.2}Fe_{0.8}O_3$ (LSCF). ECS Trans. **25**, 2871–2879 (2009)
188. Huang, Y.L., Hussain, A.M., Pellegrinelli, C., et al.: Chromium poisoning effects on surface exchange kinetics of $La_{0.6}Sr_{0.4}Co_{0.2}Fe_{0.8}O_{3-\delta}$. ACS Appl. Mater. Interfaces **9**, 16660–16668 (2017)
189. Chen, Y., Yoo, S., Li, X., et al.: An effective strategy to enhancing tolerance to contaminants poisoning of solid oxide fuel cell cathodes. Nano Energy **47**, 474–480 (2018)
190. Liu, R.R., Taniguchi, S., Shiratori, Y., et al.: Influence of SO_2 on the long-term durability of SOFC cathodes. ECS Trans. **35**, 2255–2260 (2011)
191. Xiong, Y.P., Yamaji, K., Horita, T., et al.: Sulfur poisoning of SOFC cathodes. J. Electrochem. Soc. **156**, B588–B592 (2009)
192. Yu, Y., Nikiforov, A.Y., Kaspar, T.C., et al.: Chemical characterization of surface precipitates in $La_{0.7}Sr_{0.3}Co_{0.2}Fe_{0.8}O_{3-\delta}$ as cathode material for solid oxide fuel cells. J. Power Sources **333**, 247–253 (2016)
193. Hagen, A., Neufeld, K., Liu, Y.L.: Effect of humidity in air on performance and long-term durability of SOFCs. J. Electrochem. Soc. **157**, B1343–B1348 (2010)
194. Nielsen, J., Hagen, A., Liu, Y.L.: Effect of cathode gas humidification on performance and durability of solid oxide fuel cells. Solid State Ion. **181**, 517–524 (2010)
195. Bucher, E., Sitte, W.: Long-term stability of the oxygen exchange properties of $(La,Sr)_{1-z}(Co,Fe)O_{3-\delta}$ in dry and wet atmospheres. Solid State Ion. **192**, 480–482 (2011)
196. Bucher, E., Sitte, W., Klauser, F., et al.: Impact of humid atmospheres on oxygen exchange properties, surface-near elemental composition, and surface morphology of $La_{0.6}Sr_{0.4}CoO_{3-\delta}$. Solid State Ion. **208**, 43–51 (2012)
197. Liu, R.R., Kim, S.H., Taniguchi, S., et al.: Influence of water vapor on long-term performance and accelerated degradation of solid oxide fuel cell cathodes. J. Power Sources **196**, 7090–7096 (2011)
198. Zhou, X.D., Templeton, J.W., Zhu, Z., et al.: Electrochemical performance and stability of the cathode for solid oxide fuel cells. III. Role of volatile boron species on LSM/YSZ and LSCF. J. Electrochem. Soc. **157**, B1019–B1023 (2010)
199. Chen, K., Ai, N., Lievens, C., et al.: Impact of volatile boron species on the microstructure and performance of nano-structured $(Gd,Ce)O_2$ infiltrated $(La,Sr)MnO_3$ cathodes of solid oxide fuel cells. Electrochem. Commun. **23**, 129–132 (2012)
200. Chen, K., Ai, N., Zhao, L., et al.: Effect of volatile boron species on the electrocatalytic activity of cathodes of solid oxide fuel cells: I. $(La,Sr)MnO_3$ based electrodes. J. Electrochem. Soc. **160**, F183–F190 (2013)
201. Chen, K., Ai, N., Zhao, L., et al.: Effect of volatile boron species on the electrocatalytic activity of cathodes of solid oxide fuel cells: II. $(La,Sr)(Co,Fe)O_3$ based electrodes. J. Electrochem. Soc. **160**, F301–F308 (2013)
202. Zhao, L., Hyodo, J., Chen, K., et al.: Effect of boron deposition and poisoning on the surface exchange properties of LSCF electrode materials of solid oxide fuel cells. J. Electrochem. Soc. **160**, F682–F686 (2013)
203. Chen, K., Hyodo, J., O'Donnell, K.M., et al.: Effect of volatile boron species on the electrocatalytic activity of cathodes of solid oxide fuel cells. J. Electrochem. Soc. **161**, F1163–F1170 (2014)
204. Horita, T., Cho, D.H., Wang, F., et al.: Correlation between degradation of cathode performance and chromium concentration in $(La,Sr)MnO_3$ cathode. Solid State Ion. **225**, 151–156 (2012)
205. Jiang, S.P., Zhen, Y.D.: Mechanism of Cr deposition and its application in the development of Cr-tolerant cathodes of solid oxide fuel cells. Solid State Ion. **179**, 1459–1464 (2008)
206. Jiang, S.P., Zhang, S., Zhen, Y.D.: Deposition of Cr species at $(La,Sr)(Co,Fe)O_{3-\delta}$ cathodes of solid oxide fuel cells. J. Electrochem. Soc. **153**, A127–A134 (2006)
207. Chen, X.B., Zhen, Y.D., Li, J., et al.: Chromium deposition and poisoning in dry and humidified air at $(La_{0.8}Sr_{0.2})_{0.9}MnO_{3+\delta}$ cathodes of solid oxide fuel cells. Int. J. Hydrogen Energy **35**, 2477–2485 (2010)
208. Wang, C.C., Becker, T., Chen, K., et al.: Effect of temperature on the chromium deposition and poisoning of $La_{0.6}Sr_{0.4}Co_{0.2}Fe_{0.8}O_{3-\delta}$ cathodes of solid oxide fuel cells. Electrochim. Acta **139**, 173–179 (2014)
209. Wei, B., Schroeder, M., Martin, M.: Surface cation segregation and chromium deposition on the double-perovskite oxide $PrBaCo_2O_{5+\delta}$. ACS Appl. Mater. Interfaces **10**, 8621–8629 (2018)
210. Jiang, S.P., Zhang, J.P., Zheng, X.G.: A comparative investigation of chromium deposition at air electrodes of solid oxide fuel cells. J. Eur. Ceram. Soc. **22**, 361–373 (2002)
211. Schuler, J.A., Wuillemin, Z., Hessler-Wyser, A., et al.: Cr-poisoning in $(La,Sr)(Co,Fe)O_3$ cathodes after 10,000 h SOFC stack testing. J. Power Sources **211**, 177–183 (2012)
212. Wei, B., Chen, K., Wang, C.C., et al.: Cr deposition on porous $La_{0.6}Sr_{0.4}Co_{0.2}Fe_{0.8}O_{3-\delta}$ electrodes of solid oxide cells under open circuit condition. Solid State Ion. **281**, 29–37 (2015)
213. Beez, A., Yin, X., Menzler, N.H., et al.: Insight into the reaction mechanism of $(La_{0.58}Sr_{0.40})(Co_{0.20}Fe_{0.80})O_{3-\delta}$ cathode with volatile chromium species at high current density in a solid oxide fuel cell stack. J. Electrochem. Soc. **164**, F3028–F3034 (2017)
214. Menzler, N.H., Sebold, D., Wessel, E.: Interaction of $La_{0.58}Sr_{0.40}Co_{0.20}Fe_{0.80}O_{3-\delta}$ cathode with volatile Cr in a stack test—scanning electron microscopy and transmission electron microscopy investigations. J. Power Sources **254**, 148–152 (2014)
215. Wang, F.F., Yamaji, K., Cho, D.H., et al.: Sulfur poisoning on $La_{0.6}Sr_{0.4}Co_{0.2}Fe_{0.8}O_3$ cathode for SOFCs. J. Electrochem. Soc. **158**, B1391–B1397 (2011)
216. Yang, Z.B., Guo, M.Y., Wang, N., et al.: A short review of cathode poisoning and corrosion in solid oxide fuel cell. Int. J. Hydrogen Energy **42**, 24948–24959 (2017)
217. Wang, C.C., Chen, K., Jiang, S.P.: Mechanism and kinetics of SO_2 poisoning on the electrochemical activity of $La_{0.8}Sr_{0.2}MnO_3$ cathodes of solid oxide fuel cells. J. Electrochem. Soc. **163**, F771–F780 (2016)
218. Wang, C.C., Chen, K., Jiang, T., et al.: Sulphur poisoning of solid oxide electrolysis cell anodes. Electrochim. Acta **269**, 188–195 (2018)
219. Schuler, A.J., Wuillemin, Z., Hessler-Wyser, A., et al.: Sulfur as pollutant species on the cathode side of a SOFC system. ECS Trans. **25**, 2845–2852 (2009)
220. Bucher, E., Gspan, C., Sitte, W.: Degradation and regeneration of the SOFC cathode material $La_{0.6}Sr_{0.4}CoO_{3-\delta}$ in SO_2-containing atmospheres. Solid State Ion. **272**, 112–120 (2015)
221. Wang, F., Yamaji, K., Cho, D.H., et al.: Evaluation of sulfur dioxide poisoning for LSCF cathodes. Fuel Cells **13**, 520–525 (2013)
222. Wang, F., Yamaji, K., Cho, D.H., et al.: Effect of strontium concentration on sulfur poisoning of LSCF cathodes. Solid State Ion. **225**, 157–160 (2012)
223. Kushi, T.: Effects of sulfur poisoning on degradation phenomena in oxygen electrodes of solid oxide electrolysis cells and solid oxide fuel cells. Int. J. Hydrogen Energy **42**, 9396–9405 (2017)

224. Wang, C.C., Chen, K., Jiang, S.P.: Sulfur deposition and poisoning of $La_{0.6}Sr_{0.4}Co_{0.2}Fe_{0.8}O_{3-\delta}$ cathode materials of solid oxide fuel cells. J. Electrochem. Soc. **161**, F1133–F1139 (2014)
225. Wang, F., Kishimoto, H., Develos-Bagarinao, K., et al.: Interrelation between sulfur poisoning and performance degradation of LSCF cathode for SOFCs. J. Electrochem. Soc. **163**, F899–F904 (2016)
226. De Vero, J.C., Develos-Bagarinao, K., Liu, S.S., et al.: Sulfur poisoning behavior of $La_{1-x}Sr_xCo_{1-y}Fe_yO_{3-\delta}$ thin films with different compositions. J. Alloys Compd. **748**, 608–619 (2018)
227. Zhang, T., Fahrenholtz, W.G., Reis, S.T., et al.: Borate volatility from SOFC sealing glasses. J. Am. Ceram. Soc. **91**, 2564–2569 (2008)
228. Chen, K., Hyodo, J., Zhao, L., et al.: Effect of volatile boron species on the microstructure and composition of $(La,Sr)MnO_3$ and $(La,Sr)(Co,Fe)O_3$ cathode materials of solid oxide fuel cells. J. Electrochem. Soc. **160**, F1033–F1039 (2013)
229. Chen, K., Liu, S.S., Guagliardo, P., et al.: A fundamental study of boron deposition and poisoning of $La_{0.8}Sr_{0.2}MnO_3$ cathode of solid oxide fuel cells under accelerated conditions. J. Electrochem. Soc. **162**, F1282–F1291 (2015)
230. Chen, K., Hyodo, J., Ai, N., et al.: Boron deposition and poisoning of $La_{0.8}Sr_{0.2}MnO_3$ oxygen electrodes of solid oxide electrolysis cells under accelerated operation conditions. Int. J. Hydrogen Energy **41**, 1419–1431 (2016)
231. Chen, K., Fang, L., Zhang, T., et al.: New zinc and bismuth doped glass sealants with substantially suppressed boron deposition and poisoning for solid oxide fuel cells. J. Mater. Chem. A **2**, 18655–18665 (2014)
232. Hu, B., Mahapatra, M.K., Keane, M., et al.: Effect of CO_2 on the stability of strontium doped lanthanum manganite cathode. J. Power Sources **268**, 404–413 (2014)
233. Ponce, S., Peña, M.A., Fierro, J.L.G.: Surface properties and catalytic performance in methane combustion of Sr-substituted lanthanum manganites. Appl. Catal. B **24**, 193–205 (2000)
234. Darvish, S., Gopalan, S., Zhong, Y.: Thermodynamic stability maps for the $La_{0.6}Sr_{0.4}Co_{0.2}Fe_{0.8}O_{3\pm\delta}$–$CO_2$–$O_2$ system for application in solid oxide fuel cells. J. Power Sources **336**, 351–359 (2016)
235. Yan, A., Cheng, M., Dong, Y., et al.: Investigation of a $Ba_{0.5}Sr_{0.5}Co_{0.8}Fe_{0.2}O_{3-\delta}$ based cathode IT-SOFC: I. The effect of CO_2 on the cell performance. Appl. Catal. B Environ. **66**, 64–71 (2006)
236. Yan, A., Liu, B., Dong, Y., et al.: A temperature programmed desorption investigation on the interaction of $Ba_{0.5}Sr_{0.5}Co_{0.8}Fe_{0.2}O_{3-\delta}$ perovskite oxides with CO_2 in the absence and presence of H_2O and O_2. Appl. Catal. B Environ. **80**, 24–31 (2008)
237. Bucher, E., Egger, A., Caraman, G.B., et al.: Stability of the SOFC cathode material $(Ba,Sr)(Co,Fe)O_{3-\delta}$ in CO_2-containing atmospheres. J. Electrochem. Soc. **155**, B1218–B1224 (2008)
238. Zhou, W., Liang, F.L., Shao, Z.P., et al.: Hierarchical CO_2-protective shell for highly efficient oxygen reduction reaction. Sci. Rep. **2**, 327 (2012)
239. Arnold, M., Wang, H., Feldhoff, A.: Influence of CO_2 on the oxygen permeation performance and the microstructure of perovskite-type $(Ba_{0.5}Sr_{0.5})(Co_{0.8}Fe_{0.2})O_{3-\delta}$ membranes. J. Membr. Sci. **293**, 44–52 (2007)
240. Schmale, K., Barthel, J., Bernemann, M., et al.: AFM investigations on the influence of CO_2 exposure on $Ba_{0.5}Sr_{0.5}Co_{0.8}Fe_{0.2}O_{3-\delta}$. J. Solid State Electrochem. **17**, 2897–2907 (2013)
241. Sharma, V., Mahapatra, M.K., Krishnan, S., et al.: Effects of moisture on (La,A) MnO_3 (A = Ca, Sr, and Ba) solid oxide fuel cell cathodes: a first-principles and experimental study. J. Mater. Chem. A **4**, 5605–5615 (2016)
242. Hu, B., Keane, M., Mahapatra, M.K., et al.: Stability of strontium-doped lanthanum manganite cathode in humidified air. J. Power Sources **248**, 196–204 (2014)
243. Kim, S.H., Shim, K.B., Kim, C.S., et al.: Degradation of solid oxide fuel cell cathodes accelerated at a high water vapor concentration. J. Fuel Cell Sci. Technol. **7**, 0210111–0210116 (2010)
244. Matsuda, T., Yamanaka, S., Kurosaki, K., et al.: High temperature phase transitions of $SrZrO_3$. J. Alloys Compd. **351**, 43–46 (2003)
245. Willy Poulsen, F., van der Puil, N.: Phase relations and conductivity of Sr- and La-zirconate. Solid State Ion. **53–56**, 777–783 (1992)
246. Wankmüller, F., Szász, J., Joos, J., et al.: Correlative tomography at the cathode/electrolyte interfaces of solid oxide fuel cells. J. Power Sources **360**, 399–408 (2017)
247. Tsoga, A., Gupta, A., Naoumidis, A., et al.: Gadolinia-doped ceria and yttria stabilized zirconia interfaces: regarding their application for SOFC technology. Acta Mater. **48**, 4709–4714 (2000)
248. Develos-Bagarinao, K., Yokokawa, H., Kishimoto, H., et al.: Elucidating the origin of oxide ion blocking effects at GDC/$SrZr(Y)O_3$/YSZ interfaces. J. Mater. Chem. A **5**, 8733–8743 (2017)
249. Kiebach, R., Zhang, W.W., Zhang, W., et al.: Stability of $La_{0.6}Sr_{0.4}Co_{0.2}Fe_{0.8}O_3$/$Ce_{0.9}Gd_{0.1}O_2$ cathodes during sintering and solid oxide fuel cell operation. Journal of Power Sources **283**, 151–161 (2015)
250. Li, N., Ai, N., He, S., et al.: Effect of Pd doping on the activity and stability of directly assembled $La_{0.95}Co_{0.19}Fe_{0.76}Pd_{0.05}O_{3-\delta}$ cathodes of solid oxide fuel cells. Solid State Ion. **316**, 38–46 (2018)
251. Yin, X., Bencze, L., Motalov, V., et al.: Thermodynamic perspective of Sr-related degradation issues in SOFCs. Int. J. Appl. Ceram. Technol. **15**, 380–390 (2018)
252. Tietz, F., Mai, A., Stöver, D.: From powder properties to fuel cell performance—a holistic approach for SOFC cathode development. Solid State Ion. **179**, 1509–1515 (2008)
253. Gao, Z., Barnett, S.A.: Effects of reduced firing temperature on anode-supported solid oxide fuel cells. J. Electrochem. Soc. **161**, F600–F604 (2014)
254. Knibbe, R., Hjelm, J., Menon, M., et al.: Cathode-electrolyte interfaces with CGO barrier layers in SOFC. J. Am. Ceram. Soc. **93**, 2877–2883 (2010)
255. Celikbilek, O., Thieu, C.A., Agnese, F., et al.: Enhanced catalytic activity of nanostructured, A-site deficient $(La_{0.7}Sr_{0.3})_{0.95}(Co_{0.2}Fe_{0.8})O_{3-\delta}$ for SOFC cathodes. J. Mater. Chem. A **7**, 25102–25111 (2019)
256. Jiang, S.P., Love, J.G., Zhang, J.P., et al.: The electrochemical performance of LSM/zirconia-yttria interface as a function of a-site non-stoichiometry and cathodic current treatment. Solid State Ion. **121**, 1–10 (1999)
257. Jiang, S.P., Zhang, J.P., Ramprakash, Y., et al.: An investigation of shelf-life of strontium doped $LaMnO_3$ materials. J. Mater. Sci. **35**, 2735–2741 (2000)
258. Choi, S., Park, S., Shin, J., et al.: The effect of calcium doping on the improvement of performance and durability in a layered perovskite cathode for intermediate-temperature solid oxide fuel cells. J. Mater. Chem. A **3**, 6088–6095 (2015)
259. Ito, W., Nagai, T., Sakon, T.: Oxygen separation from compressed air using a mixed conducting perovskite-type oxide membrane. Solid State Ion. **178**, 809–816 (2007)
260. Nagai, T., Ito, W., Sakon, T.: Relationship between cation substitution and stability of perovskite structure in $SrCoO_{3-\delta}$-based mixed conductors. Solid State Ion. **177**, 3433–3444 (2007)

261. Chen, X.B., Jiang, S.P.: Highly active and stable $(La_{0.24}Sr_{0.16}Ba_{0.6})(Co_{0.5}Fe_{0.44}Nb_{0.06})O_{3-\delta}$ (LSBCFN) cathodes for solid oxide fuel cells prepared by a novel mixing synthesis method. J. Mater. Chem. A **1**, 4871–4878 (2013)
262. Zhang, P., Guan, G., Khaerudini, D.S., et al.: Properties of A-site nonstoichiometry $(Pr_{0.4})_xSr_{0.6}Co_{0.2}Fe_{0.7}Nb_{0.1}O_{3-\sigma}$ $(0.9 \leqslant x \leqslant 1.1)$ as symmetrical electrode material for solid oxide fuel cells. J. Power Sources **248**, 163–171 (2014)
263. Li, J., Yang, C., Liu, M.: High performance intermediate temperature solid oxide fuel cells with $Ba_{0.5}Sr_{0.5}Co_{0.8}Fe_{0.1}Nb_{0.1}O_{3-\delta}$ as cathode. Ceram. Int. **42**, 19397–19401 (2016)
264. Wang, F., Nakamura, T., Yashiro, K., et al.: Effect of Nb doping on the chemical stability of BSCF-based solid solutions. Solid State Ion. **262**, 719–723 (2014)
265. Aguadero, A., Perez-Coll, D., de la Calle, C., et al.: $SrCo_{1-x}Sb_xO_{3-\delta}$ perovskite oxides as cathode materials in solid oxide fuel cells. J. Power Sources **192**, 132–137 (2009)
266. Wang, F., Igarashi, K., Nakamura, T., et al.: Tailoring the chemical stability of cobalt-rich perovskite mixed conductor. Solid State Ion. **288**, 2–5 (2016)
267. Aguadero, A., Pérez-Coll, D., Alonso, J.A., et al.: A new family of Mo-doped $SrCoO_{3-\delta}$ perovskites for application in reversible solid state electrochemical cells. Chem. Mater. **24**, 2655–2663 (2012)
268. Li, M., Zhao, M., Li, F., et al.: A niobium and tantalum co-doped perovskite cathode for solid oxide fuel cells operating below 500 °C. Nat. Commun. **8**, 13990 (2017)
269. Meffert, M., Unger, L.S., Grünewald, L., et al.: The impact of grain size, A/B-cation ratio, and Y-doping on secondary phase formation in $(Ba_{0.5}Sr_{0.5})(Co_{0.8}Fe_{0.2})O_{3-\delta}$. J. Mater. Sci. **52**, 2705–2719 (2017)
270. Foit, S.R., Vinke, I.C., de Haart, L.G.J., et al.: Power-to-syngas: an enabling technology for the transition of the energy system? Angew. Chem. Int. Ed. **56**, 5402–5411 (2017)
271. Duan, C., Hook, D., Chen, Y., et al.: Zr and Y co-doped perovskite as a stable, high performance cathode for solid oxide fuel cells operating below 500 °C. Energy Environ. Sci. **10**, 176–182 (2017)
272. He, W., Wu, X., Yang, G., et al.: $BaCo_{0.7}Fe_{0.22}Y_{0.08}O_{3-\delta}$ as an active oxygen reduction electrocatalyst for low-temperature solid oxide fuel cells below 600 °C. ACS Energy Lett. **2**, 301–305 (2017)
273. Zhou, W., Shao, Z., Ran, R., et al.: Novel $SrSc_{0.2}Co_{0.8}O_{3-\delta}$ as a cathode material for low temperature solid-oxide fuel cell. Electrochem. Commun. **10**, 1647–1651 (2008)
274. Popov, M., Bychkov, S., Nemudry, A.: Modification of mixed conducting $Ba_{0.5}Sr_{0.5}Co_{0.8}Fe_{0.2}O_{3-\delta}$ by partial substitution of cobalt with tungsten. Russ. J. Electrochem. **52**, 648–654 (2016)
275. Shin, J.F., Xu, W., Zanella, M., et al.: Self-assembled dynamic perovskite composite cathodes for intermediate temperature solid oxide fuel cells. Nat. Energy **2**, 16214 (2017)
276. Duan, C., Tong, J., Shang, M., et al.: Readily processed protonic ceramic fuel cells with high performance at low temperatures. Science **349**, 1321–1326 (2015)
277. Kim, Y.M., Chen, X.B., Jiang, S.P., et al.: Chromium deposition and poisoning at $Ba_{0.5}Sr_{0.5}Co_{0.8}Fe_{0.2}O_{3-\delta}$ cathode of solid oxide fuel cells. Electrochem. Solid State Lett. **14**, B41–B45 (2011)
278. Usiskin, R.E., Davenport, T.C., Wang, R.Y., et al.: Bulk properties of the oxygen reduction catalyst $SrCo_{0.9}Nb_{0.1}O_{3-\delta}$. Chem. Mater. **28**, 2599–2608 (2016)
279. Wang, F., Nakamura, T., Yashiro, K., et al.: The crystal structure, oxygen nonstoichiometry and chemical stability of $Ba_{0.5}Sr_{0.5}Co_{0.8}Fe_{0.2}O_{3-\delta}$ (BSCF). Phys. Chem. Chem. Phys. **16**, 7307–7314 (2014)
280. Fang, S.M., Yoo, C.Y., Bouwmeester, H.J.M.: Performance and stability of niobium-substituted $Ba_{0.5}Sr_{0.5}Co_{0.8}Fe_{0.2}O_{3-\delta}$ membranes. Solid State Ion. **195**, 1–6 (2011)
281. Vohs, J.M., Gorte, R.J.: High-performance SOFC cathodes prepared by infiltration. Adv. Mater. **21**, 943–956 (2009)
282. Jiang, Z.Y., Xia, C.R., Chen, F.L.: Nano-structured composite cathodes for intermediate-temperature solid oxide fuel cells via an infiltration/impregnation technique. Electrochim. Acta **55**, 3595–3605 (2010)
283. Jiang, S.P.: Nanoscale and nano-structured electrodes of solid oxide fuel cells by infiltration: advances and challenges. Int. J. Hydrogen Energy **37**, 449–470 (2012)
284. Liu, Z., Liu, B., Ding, D., et al.: Fabrication and modification of solid oxide fuel cell anodes via wet impregnation/infiltration technique. J. Power Sources **237**, 243–259 (2013)
285. Ding, D., Li, X., Lai, S.Y., et al.: Enhancing SOFC cathode performance by surface modification through infiltration. Energy Environ. Sci. **7**, 552–575 (2014)
286. Lynch, M.E., Yang, L., Qin, W.T., et al.: Enhancement of $La_{0.6}Sr_{0.4}Co_{0.2}Fe_{0.8}O_{3-\delta}$ durability and surface electrocatalytic activity by $La_{0.85}Sr_{0.15}MnO_{3\pm\delta}$ investigated using a new test electrode platform. Energy Environ. Sci. **4**, 2249–2258 (2011)
287. Qiu, P., Li, J., Liu, B., et al.: Study on the ORR mechanism and CO_2-poisoning resistance of $La_{0.8}Sr_{0.2}MnO_{3-\delta}$-coated $Ba_{0.5}Sr_{0.5}Co_{0.8}Fe_{0.2}O_{3-\delta}$ cathode for intermediate temperature solid oxide fuel cells. J. Electrochem. Soc. **164**, F981–F987 (2017)
288. Chen, Y., Choi, Y., Yoo, S., et al.: A highly efficient multiphase catalyst dramatically enhances the rate of oxygen reduction. Joule **2**, 938–949 (2018)
289. Pei, K., Zhou, Y., Xu, K., et al.: Enhanced Cr-tolerance of an SOFC cathode by an efficient electro-catalyst coating. Nano Energy **72**, 104704 (2020)
290. Li, M., Zhou, W., Zhu, Z.: Highly CO_2-tolerant cathode for intermediate-temperature solid oxide fuel cells: samarium-doped ceria-protected $SrCo_{0.85}Ta_{0.15}O_{3-\delta}$ hybrid. ACS Appl. Mater. Interfaces **9**, 2326–2333 (2017)
291. Zhang, X., Li, W., Guan, B., et al.: A-site deficient $La_{2-x}NiO_{4+\delta}$ infiltrated LSCF cathode with improved performance and stability. ECS Trans. **78**, 593–601 (2017)
292. Li, J., Li, J., Yan, D., et al.: Promoted Cr-poisoning tolerance of $La_2NiO_{4+\delta}$-coated $PrBa_{0.5}Sr_{0.5}Co_{1.5}Fe_{0.5}O_{5+\delta}$ cathode for intermediate temperature solid oxide fuel cells. Electrochim. Acta **270**, 294–301 (2018)
293. Liu, Y., Shuang, J., Tong, X., et al.: Enhanced performance and stability of $La_2NiO_{4+\delta}$ impregnated $La_{0.8}Sr_{0.2}Co_{0.8}Ni_{0.2}O_{3-\delta}$ oxygen electrodes for solid oxide electrolysis cells. Electrochim. Acta **298**, 852–857 (2019)
294. Qiu, P., Li, J., Jia, L., et al.: $LaCoO_{3-\delta}$ coated $Ba_{0.5}Sr_{0.5}Co_{0.8}Fe_{0.2}O_{3-\delta}$ cathode for intermediate temperature solid oxide fuel cells. Electrochim. Acta **319**, 981–989 (2019)
295. Chen, H., Guo, Z., Zhang, L.A., et al.: Improving the electrocatalytic activity and durability of the $La_{0.6}Sr_{0.4}Co_{0.2}Fe_{0.8}O_{3-\delta}$ cathode by surface modification. ACS Appl. Mater. Interfaces **10**, 39785–39793 (2018)
296. dos Santos-Gómez, L., Porras-Vázquez, J., Losilla, E., et al.: Stability and performance of $La_{0.6}Sr_{0.4}Co_{0.2}Fe_{0.8}O_{3-\delta}$ nanostructured cathodes with $Ce_{0.8}Gd_{0.2}O_{1.9}$ surface coating. J. Power Sources **347**, 178–185 (2017)
297. Tomov, R.I., Mitchell-Williams, T., Gao, C., et al.: Performance optimization of LSCF/Gd:CeO_2 composite cathodes via single-step inkjet printing infiltration. J. Appl. Electrochem. **47**, 641–651 (2017)
298. Choi, M., Ibrahim, I.A.M., Kim, K., et al.: Engineering of charged defects at perovskite oxide surfaces for exceptionally

stable solid oxide fuel cell electrodes. ACS Appl. Mater. Interfaces (2020). https://doi.org/10.1021/acsami.9b21919
299. Gong, Y., Palacio, D., Song, X., et al.: Stabilizing nanostructured solid oxide fuel cell cathode with atomic layer deposition. Nano Lett. **13**, 4340–4345 (2013)
300. Gong, Y., Patel, R.L., Liang, X., et al.: Atomic layer deposition functionalized composite SOFC cathode $La_{0.6}Sr_{0.4}Fe_{0.8}Co_{0.2}O_{3-\delta}$–$Gd_{0.2}Ce_{0.8}O_{1.9}$: enhanced long-term stability. Chem. Mater. **25**, 4224–4231 (2013)
301. Ai, N., Li, N., He, S., et al.: Highly active and stable $Er_{0.4}Bi_{1.6}O_3$ decorated $La_{0.76}Sr_{0.19}MnO_{3+\delta}$ nanostructured oxygen electrodes for reversible solid oxide cells. J. Mater. Chem. A **5**, 12149–12157 (2017)
302. Ai, N., Chen, M., He, S., et al.: High performance nanostructured bismuth oxide–cobaltite as a durable oxygen electrode for reversible solid oxide cells. J. Mater. Chem. A **6**, 6510–6520 (2018)
303. He, S., Zhang, Q., Maurizio, G., et al.: In situ formation of $Er_{0.4}Bi_{1.6}O_3$ protective layer at cobaltite cathode/Y_2O_3–ZrO_2 electrolyte interface under solid oxide fuel cell operation conditions. ACS Appl. Mater. Interfaces **10**, 40549–40559 (2018)

Kongfa Chen is a Professor at the College of Materials Science and Engineering, Fuzhou University. He received his B.S., M.S. and Ph.D. from the Harbin Institute of Technology. Prior to his current position, he worked as a postdoctoral research fellow at Nanyang Technological University and Curtin University. His research interests are solid oxide fuel cells and solid oxide electrolysis cells. He is currently focusing on the surface distribution of cations and manipulation of electrode/electrolyte interfaces under the influence of electrochemical polarization.

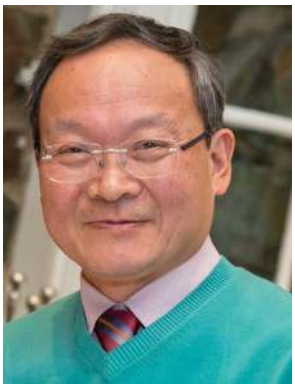

San Ping Jiang is a John Curtin Distinguished Professor at the WA School of Mines: Minerals, Energy and Chemical Engineering and the Deputy Director of Fuels and Energy Technology Institute, Curtin University, Australia. Dr. Jiang obtained his B.E. from South China University of Technology and Ph.D. from The City University, London. Before joining Curtin University in 2010, Dr. Jiang worked at CSIRO Materials Science and Manufacturing Division, Ceramic Fuel Cells Ltd. in Australia and Nanyang Technological University in Singapore. His research interests encompass fuel cells, water electrolysis, photoelectrochemical catalysis, supercapacitors, carbon dioxide reduction, single-atom catalysts and nanostructured functional materials. Dr Jiang has published ~ 420 journal papers, which have accrued over 20500 citations with an *h*-index of 75. Dr. Jiang is a highly cited researcher (HCR) in Cross-Field by Clarivate Analytics/Web of Science in 2018.